Particle-Reinforced Metal Matrix Nanocomposites Fabricated by Selective Laser Melting: A State of the Art Review

W.H. Yu[1, 2], S.L. Sing[2], C.K. Chua[2], C.N. Kuo[3, 4*], X.L. Tian[1*]

[1] *Key Laboratory for Liquid–Solid Structural Evolution and Processing of Materials, Ministry of Education, Shandong University, Jinan 250061, People's Republic of China*

[2] *Singapore Centre for 3D Printing, School of Mechanical & Aerospace Engineering, Nanyang Technological University, 50 Nanyang Avenue, 639798, Singapore*

[3] *Department of Bioinformatics and Medical Engineering, Asia University, Taichung 41354, Taiwan*

[4] *3D Printing Medical Research Institute, Asia University, Taichung 41354, Taiwan*

Abstract: Significant progress has been made in understanding selective laser melting (SLM) process as well as fabrication of various materials using this technology. This paper covers the emerging research on particle reinforced metal matrix nanocomposites (MMNCs) with SLM and provides a comprehensive overview of the underlying scientific topics behind them. In order to provide a thorough basis for understanding and controlling of the SLM processing of MMNCs fabrication, the state of the art research from the perspective of materials and SLM processing parameters is reviewed. Feedstock preparation methods for MMNCs are emphasized and compared in detail. Mechanical properties of nanocomposites and the enhancing mechanisms due to reinforcement are discussed in depth, highlighting strength, microhardness and fatigue properties. Thereafter,

* Corresponding authors.
Email: tianxuelei@sdu.edu.cn (X.L. Tian), cnkuo@asia.edu.tw (C.N. Kuo).

defects, especially those associated with SLM processing, are also elucidated by discussing their classification, mechanisms of formation and tendency in MMNCs. Applications in aerospace, automobile, electronics and electronic packaging, and biomedical industry are illustrated. Summary of findings from this review and trends for future research in the development of MMNCs by SLM are addressed in the final part.

Keywords: Additive manufacturing; Particle-reinforced metal matrix nanocomposites; Selective laser melting; Powder materials; Processing parameters; Enhancing mechanisms

Contents

1. Introduction

Composites are a class of materials that have two or more distinct constituents with significantly different chemical, physical and mechanical properties. They are a breakthrough and significant human achievement since they can be dated back to ancient time when grass stems reinforced adobes were used as construction materials [1, 2]. Research and mass production of modern composites originated from the very last century and the notion of custom-made materials has been applied to various fields shortly after. Particle reinforced metal matrix composites (MMCs) are increasingly employed in automotive, aerospace and military industry as structural applications due to their excellent combination of high strength, thermal stability, ductility and their isotropy compared with fiber or flake reinforced composites [3-6]. Examples include brake disks of particles reinforced MMCs in traffic engineering of high wear-resistance which is usually a featured property of MMCs [7]. Other applications, e.g. electronic packaging and thermal-management, make MMCs promising in industries [8].

The increasing desire for custom-made materials, especially those with light weight and high performance, has driven the development of MMCs. Metal matrix nanocomposites (MMNCs) are those MMCs in which the reinforcement of nanoparticles is employed. Due to the nanoscale structure, MMNCs have an edge over MMCs with microscale reinforcements in terms of wear resistance, damping properties and mechanical strength, making them more appealing for many applications [9, 10]. For instance, the mechanical properties of aluminum matrix composites (AMCs) reinforced with 10 vol.% Al_2O_3 and 10 vol.% SiC microscale were inferior to those of AMC reinforced with only 3 vol.% Al_2O_3 nanoparticles [11, 12]. Despite the superior properties and growing interest, the complex

processing and inadequate economic efficiency have limited the applications of MMNCs. The conventional production methods can be categorized into three types: solid state methods, semi-solid state methods and liquid state methods [13]. Solid state methods involve powder metallurgy [14], mechanical alloying [15], diffusion bonding and physical vapor deposition. Compocasting [16] and thixoforging [17, 18] are the typical semi-solid state processes used to produce MMNCs. Liquid state methods include stirring casting [19, 20], ultrasonic method [21, 22], pressure infiltration, spray deposition, *in situ* processing [23-25], arc-discharge plasma method, spark plasma sintering [26, 27], etc. One common feature of these technologies is high energy consumption, which can be attributed to the main issues arising from processing of the nanoscale sized particles. The poor wettability inherent to the powder materials due to high specific surface area and high degree of contamination is inevitable [28]. Nanometer scale sized powders worsen the surface quality further. Nanoparticles are prone to agglomerate into coarse clusters due to their poor wettability with the molten metal matrices and large Van der Waals' force, leaving homogeneous dispersion of reinforcement phases throughout the matrix extremely challenging. Extensive efforts have been devoted to improve wettability between matrix and reinforcement phase in conventional processing. For instance, metallic coating on the reinforcement, heat treatment of the particles before dispersion into melts, addition of reactive elements into the melt have been explored [13, 29, 30]. New technologies of high energy to well disperse the particles are still essential to disperse the reinforcement to achieve microstructural homogeneity and advanced mechanical properties.

Selective laser melting (SLM), as an additive manufacturing (AM) technology [31-33] applied to metals [34] and ceramics [35, 36] for decades, has shown promising potential for

MMNCs fabrication by employing a high power laser system. It facilitates near net shape manufacturing as the technology starts from preparation of CAD data files which are subsequently aligned with processing parameters and meshed to stacking 2-D layers by software, e.g. Magics. The following production process includes a loop of depositing a layer of metallic powder on a substrate plate or previous processed layers, selectively melting the powder with a high energy laser beam according to the profile of each layer, lowering the platform by one-layer thickness and then recoating a new layer of powder. The process ends with the deposition and melting of the last sliced layer of the components [37]. Fig. 1 illustrates the schematic of SLM principles and machine components. The white fonts indicate the machine related components and the black ones are the most frequently adjusted parameters, classified as processing related parameters in Fig. 2. The other comprehensive SLM process controlling parameters that are materials related are also shown in Fig. 2. The materials related parameters include the inherent properties and powder features while the processing related parameters can be controlled by the machine components.

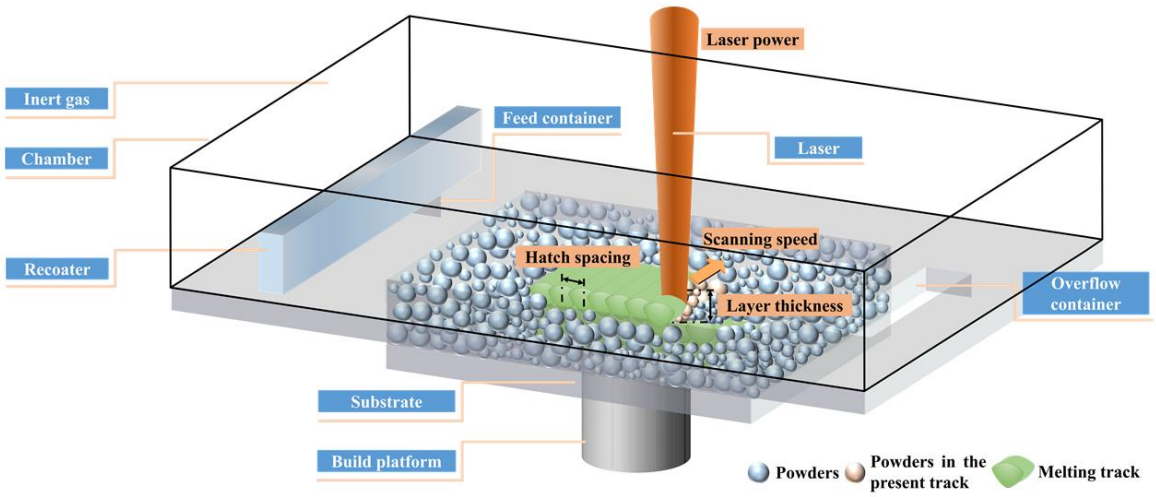

Fig. 1. Schematic of SLM machine and process. The white fonts illustrate the machine components while the black fonts illustrate the parameters.

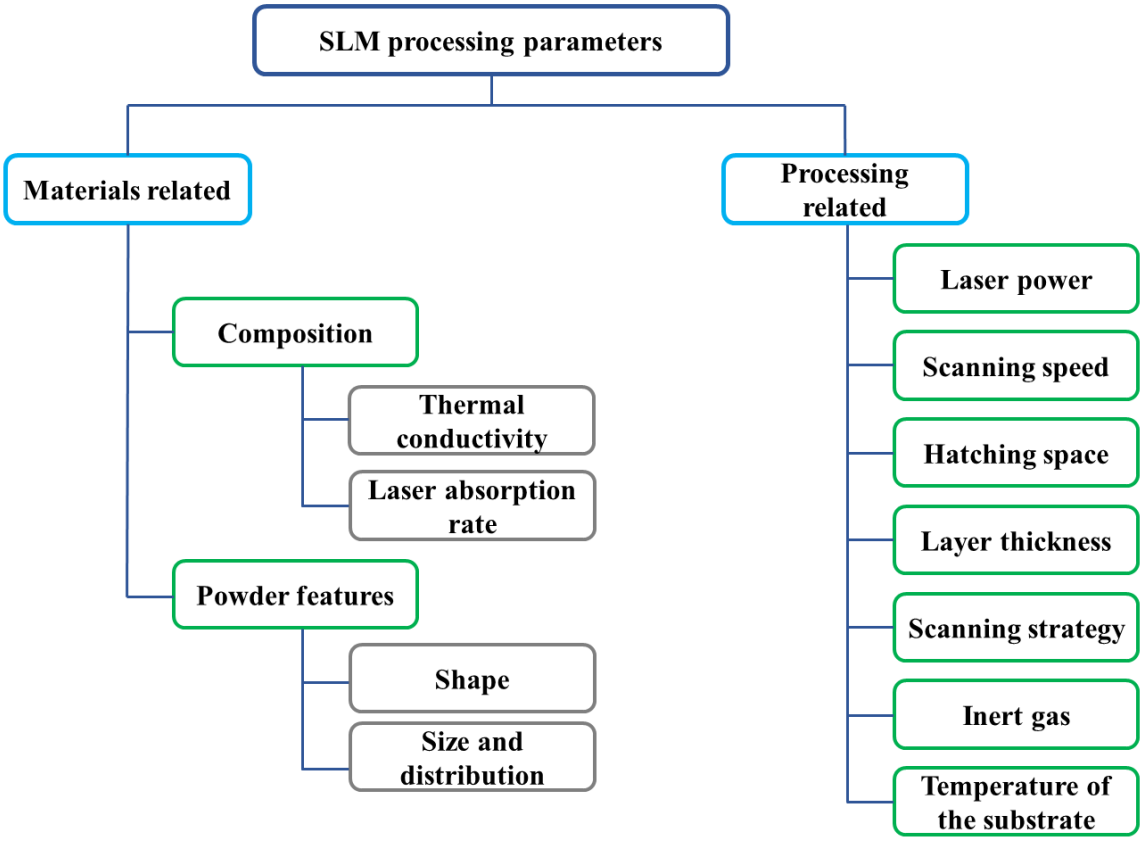

Fig. 2. SLM processing parameters.

As a powder bed fusion AM technology, SLM allows quick production of three-dimensional (3D) parts with complicated shapes directly from powder materials without the time-consuming mold design process [38]. Since high performance of MMNCs implies difficulty in post-subtractive-processing [39], near net shape manufacturing makes it suitable for end applications or at least minimizes the post-processing as nowadays polishing and heat treatment are usually essential for SLM parts [40]. SLM offers an option to reduce the production cost and lead time, especially for those parts with high performance but needed in limited quantity. Ultrafine and gradient microstructure attributing to the rapid melting and solidification process (with a cooling rate of 10^3-10^6

^{o}C/s) results in superior property to counterparts produced by conventional methods [41-44]. Another advantage is that recycle of powders allows ecological and environmental consideration as nanometer scale powders remain expensive. Thus, SLM exhibits promising potential in production of MMNCs with unique structure and properties even with metallic glass matrix composite at a fair cost [45-48]. Application of SLM to MMNCs fabrication is gaining more interest with growing investigation focusing on the exploration and optimization of the process [49, 50]. While there are promises, defects unique to SLM remain significant concerns. These include rough surface, porosity, and residual stress, etc. Therefore, to achieve the SLM processing of MMNCs, a thorough understanding of both the materials and SLM processing parameters is necessary.

Ample literatures and several reviews that focused on the knowledge of SLM process of metals or alloys are available [51-54]. The introduction of nanoparticles would incur changes in physical properties of the materials, thus affecting heat and rheology behavior of the melt pool and resulting in SLM parameters' window shift. Comprehensive understanding of the fabrication and performance of nanocomposites with SLM is necessary and this work seeks to gain a thorough understanding of the scientific and technological knowledge.

This review focuses on the status of the nanocomposites from the use of SLM while other fabrication methods of nanocomposites are not within the scope. Physical phenomena in the SLM process are introduced to offer a basic understanding of the scientific problems. An in-depth review of the fabrication consideration related to nanocomposites, including the materials and SLM processing parameters, is then presented. Emphasis on physical properties and preparation of powders is included in this review. Thereafter, mechanical

properties of MMNCs and the corresponding enhancing mechanisms are addressed to provide a deeper understanding of MMNCs. The review also addresses the defects unique to SLM technology associated with nanoparticles. The application of MMNCs especially those fabricated with SLM processing is listed and compared. The final part of this paper outlines the trends for future research.

2. Selective laser melting of metal matrix nanocomposites

SLM involves powder-liquid-solid transitions with many physical phenomena, i.e. absorption and scattering of laser radiation, heat transfer, fluid flow, evaporation and emission of materials, phase transformation and chemical reactions [55-57]. Identifying and controlling the above physical phenomena and their interactions are crucial to produce defect-free parts with full density.

Heat absorption involves the interaction between laser beam and powder materials. Photons of a laser beam undergo multiple reflection and absorption in the powder bed system [58, 59], characteristics of both affect the laser absorption and resultant melt pool features [60]. Powder shape, size distribution, packing density and thermo-physical properties are essential characteristics which would be greatly influenced by the nanoparticles. These influences will be addressed in Section 2.1. The power density distribution of laser source (P_d) often follows axisymmetric Gaussian profiles:

$$P_d = \frac{fP}{\pi r_b^2} \exp\left(-f\frac{r^2}{r_b^2}\right) \quad (1)$$

where f is the distribution factor, P is the total power of the laser beam, r_b is the radius of the laser beam and r is the radial distance of any point from the center of the laser beam. Laser types and spot size are highlighted in Eq. (1), associating with the distribution factor f

and radius of heat source r_b [53]. However, the nature of laser source is not as variable as the characteristics of the powder because it is often machine-specific and has been reviewed in metal systems elsewhere [50]. Emphasis is placed on controllable processing parameters, e.g. laser power and scanning speed, which will be discussed in Section 2.2.

Subsequent heat transfer, includes heat conduction, convection and radiation, is in concurrence with fluid flow. Fluid flow depends on various phenomena, e.g. gravity, buoyancy, Marangoni flow and evaporation. In SLM, gravity and buoyancy play minor role and thus were less discussed [61]. Marangoni convection is a surface-tension-driven flow [62-64], with the liquid of low surface tension pulled towards that with higher surface tension. Magnitude of surface tension gradient may depend on both chemical concentration and temperature gradients in the melt pool [65]. The temperature field distribution of the melt pool under laser beam with a Gaussian profile exhibits a high temperature in the center and low temperature in the border, and thus the fluid flow tends to present a radially outward flow pattern [52]. Marangoni number (*Ma*) is employed to measure the strength of the convective flow and is given by:

$$Ma = -\frac{\mathrm{d}\gamma}{\mathrm{d}T}\frac{L\Delta T}{\mu\alpha} \tag{2}$$

where L is the width of the melt pool, ΔT is the difference between the maximum temperature inside the pool and the solidus temperature of the material, μ is the dynamic viscosity, α is the thermal conductivity of the material, , and $\frac{\mathrm{d}\gamma}{\mathrm{d}T}$ is the sensitivity of the surface tension with respect to temperature.

The material vaporizes extensively when the temperature exceeds its boiling point, and the generated recoil pressures drive the fluid motion in return. When a high recoil pressure

exerts on the melt pool, penetrating deeply into certain layer thicknesses of the powder system and creating a keyhole, instability of melt surface and removal of molten material is expected [66-68]. Extreme high temperature and unstable fluid flow in keyhole mode melt pool would raise the bar to achieve parts with full density. Moreover, deviation of material composition of the components due to selective evaporation of volatile elements would cause inhomogeneity and property degradation [56, 69].

The study of multiple modes of heat and mass transfer during SLM process has been attempted in simulations due to the impossibilities of *in situ* observations of the melt pools at extreme high temperatures [69-71]. Various assumptions and simplifications have been made in these simulations due to the complex nature of the process to reduce computation expense. However, neglect of physics leads to deviation from the reality. For example, Fig. 3 illustrates the change of melt pool characteristics such as size and fluid behavior when more temperature dependent physics is taken into consideration. In Fig. 3a, if surface tension is assumed to be temperature independent, few physical effects can be obtained. In such a case, the shallowest melt pool with a constant surface tension results in the simulation deviating significantly from reality. In Fig. 3b, the temperature dependent surface tension is further considered, creating the Marangoni effect. This drives the molten materials towards the cold rear of the melt pool and increases the unstable effects onto the melt surface. Models in Fig. 3c involve recoil pressure as the temperature of the molten materials may exceed the boiling point. The laser penetrates into deep region of the materials and introduces a depression under the laser spot. The instability of the melt pool increases significantly and incurs more defects [72]. In the production of MMNCs, the introduction of nanoparticles adds complexity to the heat and mass transfer. Migration of

nanoparticles depends on the aforementioned physics in return, highlighting the importance of overall consideration of them.

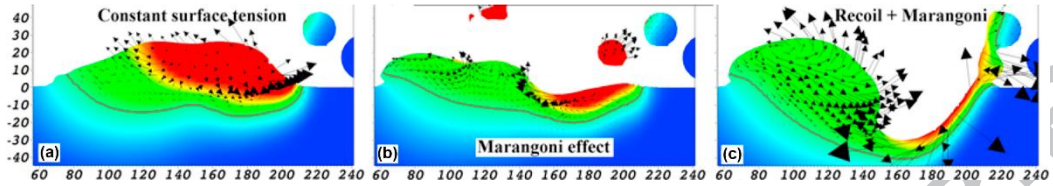

Fig. 3. 2D slices of 3D simulation demonstrating the melt pool morphology and fluid behavior with incremental physics considered. (a) Surface tension independent on the temperature, (b) surface tension dependent on the temperature, (c) further consideration of recoil pressure. The red color represents temperature above 4000 K while blue represents 293 K. The solid line outlines the melt pool (Reproduced from [72], Copyright (2016), with permission from Elsevier).

The foregoing phenomena are strongly materials and process dependent. As illustrated in Fig. 1, the powder, laser, inert gas and substrate are the four aspects of controlling parameters, among which the latter three are machine related. Laser power, scanning speed, hatch spacing and layer thickness are summarized as most controllable parameters. Scanning strategy is as important as they are although it is not illustrated in the schematic. In this section, powder stock and the above mentioned five aspects would be addressed, whereas atmosphere, laser type and spot size are not in the scope due to the paucity of publications in MMNCs production.

2.1 Materials

Feedstock of nanocomposites consists of matrix and reinforcement powders. Chemical composition (species and volume fraction) and the powder characteristics of each constituent as well as dispersion methods of reinforcement particles determine the final

feedstock properties (Fig. 4). The influencing factors of the composite powders resemble those in metal powders [73, 74], including particle shape and size distribution, which result in different flowability and powder bed density. Optical and thermal properties of the powder layer are thus influenced and essential to the aforementioned physical phenomena in SLM. In this section, selection of matrices for MMNCs and changes induced by nanoparticles are detailed as well as the resultant temperature and fluid redistribution.

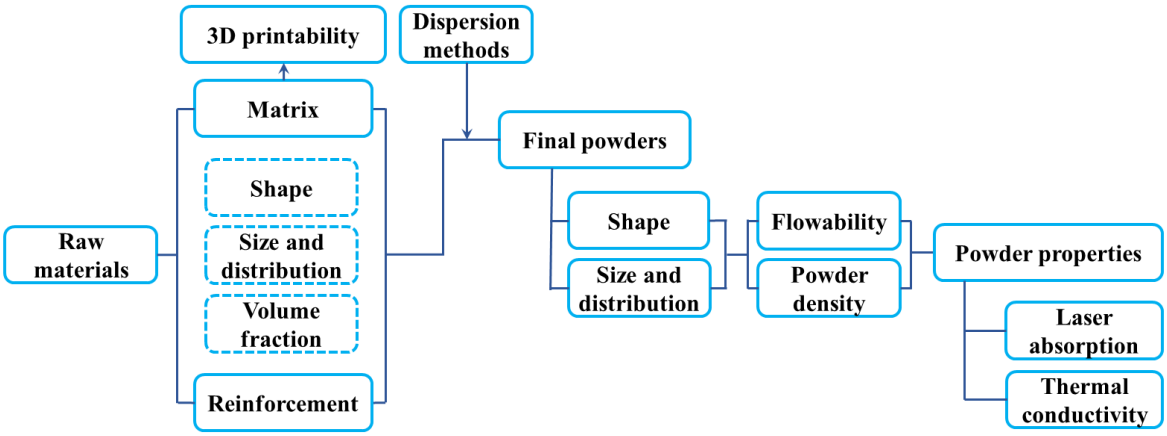

Fig. 4. Influencing parameters for composite powders for use in SLM.

2.1.1 Matrix

As custom-made materials, MMNCs products are application-oriented and have been mainly targeted for lightweight alloys with excellent ductility, e.g. Al [75], Mg [76], Cu [77] alloys. However, when it comes to the SLM process, the feasibility of processing by SLM becomes a priority, which severely limits the selection of matrices. Nowadays, only a small variety of metal powders can be reliably processed by SLM to achieve fully dense components. Among these, 316L stainless steel, commercially pure titanium (CP-Ti), Ti-6Al-4V, AlSi10Mg, A356, Inconel 718, NiTi shape memory alloy, etc. are the most

popular [78-83]. These metal materials possess proper melting and solidification dynamics, e.g. narrow solidification temperature range. This feature is an important criterion as SLM is a process of fast melting and solidification, requiring good liquid flowability. Good flowability of the molten alloys not only helps to wet the substrates but also ensure sufficient liquid feeding during solidification [84]. That is why pure metals attract more attention in 3D printing trials [85-87]. Alloying is proposed to change the solidification range. However, in most cases, the effect could be negative. Therefore, more attention should be paid to the selection of the alloying elements. For example, the vertical pseudo-binary phase diagrams of Ti-Al-V(-Mo) alloys were calculated to investigate the effect of Mo, Al and V elements on the solidification range [88]. Addition of 10 wt.% Mo expands the solidification range of Ti-6Al-4V alloy from 5 ^{o}C to 17 ^{o}C. Al and V exert little change on solidification range of Ti-Al-V alloys in the absence of Mo while negative effect shows up when Mo is involved in the systems. Eutectic composition of Al-Si alloys facilitates narrow solidification range and good flowability of alloys. In contrast, Al7075 [89], Al6061 [90] and Al-1Si [84] alloys with large solidification range show inferior access to AM with hot cracks at various processing parameters. It is important to highlight that solidification range is not the exclusive criterion while considering other physical properties, e.g. laser absorption, thermal conductivity and affinity to oxygen that explain the reasons why aluminum alloys are difficult to 3D print.

It would be a breakthrough if more alloys can be processed by SLM, as it not only facilitates the 3D printing of metals, but also providing more options of matrices for MMNCs.

When the alloys are applied to the MMNCs, the available options become even more limited. The aforementioned criteria count for the selection of matrices. However, although the current titanium based powder feedstock for SLM includes CP-Ti, Ti-6Al-4V, Ti-6Al-7Nb, Ti-21Nb-17Zr and Ti-24Nb-4Zr-8Sn, etc. it is unfortunate that only CP-Ti has been reported for MMNCs with SLM [91]. CP-Ti has an edge over other titanium alloys due to the narrow solidification range. Higher ductility of CP-Ti [92] also favors the good accommodation with the reinforcements [93]. This is not the case for aluminum alloys because AlSi10Mg has a narrow solidification range but inferior elongation compared with A356 alloys [94, 95]. AlSi10Mg alloys are more popular and effective as matrix in MMNCs, indicating the critical role of solidification range. In contrast to the wider applications of conventional processing methods of nanocomposites, most of the current research of SLM fabricated MMNCs has been limited to steel [96-98], aluminum [99-101], titanium [102-104] and nickel [105, 106] based matrices.

2.1.2 Reinforcement

2.1.2.1 The role of nanoparticles

Nanoparticles of different species imparts different effects on the MMNCs. For the end applications, strength is an important selection criterion because it determines the structural efficiency and is usually a targeted property for composites. Other than the strength of the ceramics, the distribution of nanoparticles is responsible for the structural efficiency. When nanoparticles are blended, their interaction with matrices determines the distribution of themselves. They may act as nucleation sites or non-nucleation sites, locating inside the matrix grains or in between the grain boundaries.

Martin *et al.* demonstrated that nucleation sites offer an opportunity for alloys with wide solidification range in temperature, which are not suitable for 3D printing, to achieve crack-free, equiaxed and fine-grained microstructures [107]. Nanoparticle compositions targeted to each alloy in this technology were selected according to matching crystallographic lattice spacing and density based on classical nucleation theory. The new technology enables fully dense components of Al7075 and Al6061 alloys to be attainable by AM with ZrH_2, TiB_2 or WC nanoparticles inducing nucleation sites. Additionally, Ti-6Al-4V alloy powder with ZrH_2 nanoparticles, AlSi10Mg alloy powder with WC nanoparticles and iron powder with TiC nanoparticles were also proposed to be additively manufactured for high-strength and crack-free alloys with a fine equiaxed microstructure.

In fact, exogenous nucleation sites in SLM process are not required because of the same crystal structure of the previous layers and the high cooling rate of the melts. That is why this effect is rarely mentioned in literatures. Refinement of matrix grains mainly comes from the growth restriction effect of the particles. In such a case, most nanoparticles locate themselves in between the grain boundaries [108]. Li *et al.* [78] observed no TiB_2 particles inside the α-Al grains although TiB_2 serves as nucleation sites of α-Al grains.

2.1.2.2 Feedstock preparation methods

Since no commercial feedstock of nanocomposite powder is available for SLM currently, various preparation methods have been adopted to mix the matrix and reinforcement powders. The methodologies influence the final powder morphology and would affect the heat absorption and transfer, thus deserving intensive research. Table 1 lists and compares the processing methods of powder preparation.

Table 1 Methods for preparation of nanocomposite feedstock.

Method	Application	Advantages	Demerits
Direct mixing	TiB_2/316L [96] TiC/Ti [109] SiC/Fe [110] nano-hydroxyapatite / stainless-steel [111]	Low cost; wide applicability; applicability for various volume fraction; simultaneous exposition to laser	Poor dispersion
Ball milling	TiC/AlSi10Mg [112] TiC/Ti [102] AlN/AlSi10Mg [113] TiB_2/316L stainless steel [96] TiC/316L stainless steel [114] TiC/ H13 steel [98] Al_2O_3/Al [115]	Medium cost; wide applicability; good dispersion	Poor flowability; time consuming
Direct mixing or ball milling + i*n situ* reaction	$TiC/TiAl_3$ [103] TiN/Ti_5Si_3 [116] Fe_2O_3/Al; Fe_2O_3/AlMg1SiCu; Fe_2O_3/AlSi10Mg [117] TiB_2/ Ti-45Al-2Cr-5Nb [118] TiB/Ti [119] Cr_3C_2/Fe [120]	Low/medium cost; wider suitability in particle size; good dispersion	Careful design of reaction process

In situ pre-alloying + gas-atomization	TiB_2/AlSi10Mg [78] TiB_2/Al-3.8Cu-1.3Mg [121]	Good flowability; controllable size and distribution; good dispersion	Complex
Agent deposition	Al_2O_3– acid-treated carbon nanotubes (ATCNT)/MoTiAl; Al_2O_3–ATCNT/NiAlCrMo [122] TiB_2–aerosol /AlSi10Mg [123]	Good flowability; good dispersion; applicability for various volume fraction; simultaneous exposition to laser	High cost; complex processing
Electrodeposition	Al_2O_3/Ni; SiC/Ni [124] ZrH_2/Al7075 [107]	Good flowability; good dispersion	High cost; limited powder quantity

Despite the knowledge about the tendency of nanoparticle agglomeration, direct mixing method has been adopted as a benchmark by many investigators [96, 109-111]. Nanoparticles are distributed around the matrix powder surfaces without changing their morphology. As raw materials of matrix usually exhibit spherical morphology, this method allows good flowability of the final powder mixture. However, nanoparticle agglomeration and poor wettability is inevitable. Comparison between direct mixing and other methods e.g. ball milling, indicates inferior densification behavior and mechanical properties of parts with this simple method, especially when the volume fraction is high [96].

Other processing methods must be used to avoid agglomeration of nanoparticles, among which ball milling is the most popular due to its low cost and being applicable to many powders. As a non-equilibrium process, the process includes the repeated deformation, fracture and cold welding of powder particles [125]. At the initial stage, fracture of the reinforcement particles occurs due to their brittle nature before they stick onto the matrix powder, while cold welding predominates in the matrix powder due to plastic deformation. During the deformation and cold-welding of the matrix powders, reinforcement powders dispersed inside the matrix. Fracture then takes over because of the hardening of the matrix. In the end, a dynamic between cold welding and fracture ensures a stable powder size and absence of agglomeration. In the ball milled composite powders, the nanoparticles are dispersed uniformly both on the surface and in the interior of the matrix. TiC/Ti powders of ball milling and direct mixing are illustrated in Fig. 5, from which one can observe that ball milling method facilitates uniform dispersion of nanoparticles while in direct mixing method, nanoparticles only stick to the surface of the matrix powders and no fracture happens [109]. Uniform and dispersed distribution in ball milling method promotes high

relative density and mechanical performance. The difference in the distribution of nanoparticles alters the sequence of the laser interaction between the laser and powder, thus influencing the melt pool and further physical processing. As seen in Fig. 5a, the interaction of TiC nanoparticles with laser lags behind in ball milled powder, whereas in direct mixing powder, TiC nanoparticles expose directly to the laser. The microstructure of TiC/Ti nanocomposite powder with direct mixing method is reported to be more sensitive to the SLM parameters as the powders tend to deprive the nanostructures of the composite.

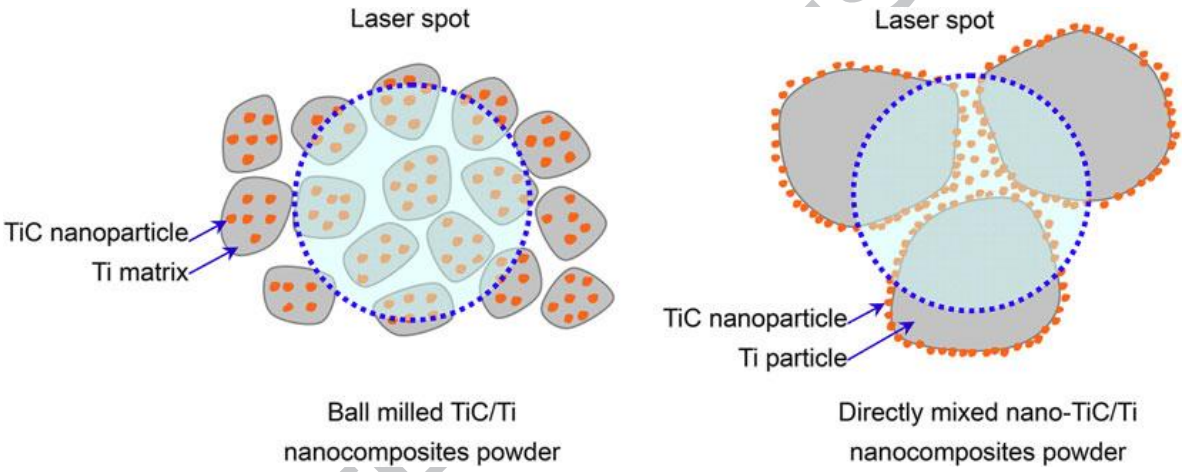

Fig. 5. Schematic of nanoparticle distribution in TiC/Ti nanocomposite powders produced by ball milling and direct mixing (Reproduced from [109], Copyright (2014), with permission from Springer Nature).

A significant change of the ball milled materials arises from the grain refinement, mainly due to severe plastic deformation and high energy input into the system. The process accompanies with the generation of various crystal defects, such as point defects and dislocations. These defects increase the internal energy of the lattice and subsequent evolution of these defects to final grain boundaries relieves the high energy. Refinement meets a limit as defects density saturates. The phenomenon has been reported in various

literatures [96, 104, 112, 126]. Grain refinement substantially promotes the final microstructure and properties of the MMNCs because of structural heredity effects [127-129]. The crystallite size (*D)* of the milled powder can be determined by XRD characterization and Scherrer formula:

$$D = \frac{0.9\lambda}{\beta \cos\theta} \quad (3)$$

where λ is the wave length of the X-ray, β is the full width at half maximum of the XRD peak, and θ is the diffraction angle.

Another advantage of ball milling is that the starting size of the reinforcement powder can range from nanometers to several micrometers. The particles could be crushed into nanometer scale during the processing. Therefore, it eases the requirement and cost of nanoparticles. TiC of 5 to 7 μm has been used to produce ultrafine reinforcement in Inconel 625 based composite with laser metal deposition [130]. AlMangour *et al.* produced TiC/316L steel nanocomposites using TiC powder with a starting mean size of 1 μm [131]. It is noted that the nanoscale ceramic particles show superior performance as the fracture of microscale particles is hard to control. It is more accessible with micrometer scale powders if there exists dissolution among the elements [103, 104, 116], although it is more time consuming.

The demerits of ball milling lie in the flowability degradation and enlarging size range. Irregular shape or rough surface which is detrimental to flowability is common after ball milling. For example, pure aluminum exhibits plate-like morphology at the initial stage of the process [132]. Equiaxed morphology could be achieved in dynamic state whilst rough surface remains [58, 133]. Attar *et al.* demonstrated that flattening of the TiB_2/Ti powder

became more pronounced when further increasing the milling time from 2 h up to 4 h [134]. Size range follows a trend of increasing first and subsequent decreasing according to principle of ball milling. Controlling of the final shape and size distribution relies on the milling time because cold welding and crack vary at different timings, depending on the ductility of the matrix and the hardening effect of the reinforcement. Table 2 illustrates the time and particle size of raw materials for ball milling. Comparison among different materials demonstrates that materials with more ductility require more time to achieve the equilibrium. Aluminum alloys require longer time than titanium alloys and steels due to their higher ductility. Han *et al.* produced 4 vol.% Al_2O_3/Al powder with up to 20 h milling, with the morphology change shown in Fig. 6 [115]. When being ball milled for 4 h (Fig. 6a), the welded particles exhibited irregular shapes with particle size over 100 μm, which could be attributed to the ductile nature of aluminum. The fracture mechanism was then activated with further milling to 8 h, following by morphological changes and particle size reduction (Fig. 6b). After ball milling for 16 h, the fracture behavior took over, generating a considerable number of small particles (~ 20 μm) (Fig. 6c). When the milling time was extended to 20 h (Fig. 6d), a narrower particle size range was achieved whilst large particles remained. To guarantee the flowability and size range of the ball milled particles, sieving is sometimes necessary [135]. Besides, the powder morphology differs at different milling procedures (such as different combinations of milling and pause duration), implying that the optimization of the parameters requires careful investigation [115]. Fig. 7 shows the characteristics of 4 vol.% Al_2O_3/Al composite powders ball milled for 20 h but with two different procedures. When the milling time was set at 15 min following a 5 min pause, some large and plate-like particles formed (Fig. 7a). While 10 and 15 min combination

causes few plate-like particles (Fig. 7b). After sieving through 170 mesh sieve (≤ 90 μm), a much smaller particle size (Fig. 7d) was achieved with the (10+15 min) procedure than that with (15+5 min) procedure (Fig. 7c) [115].

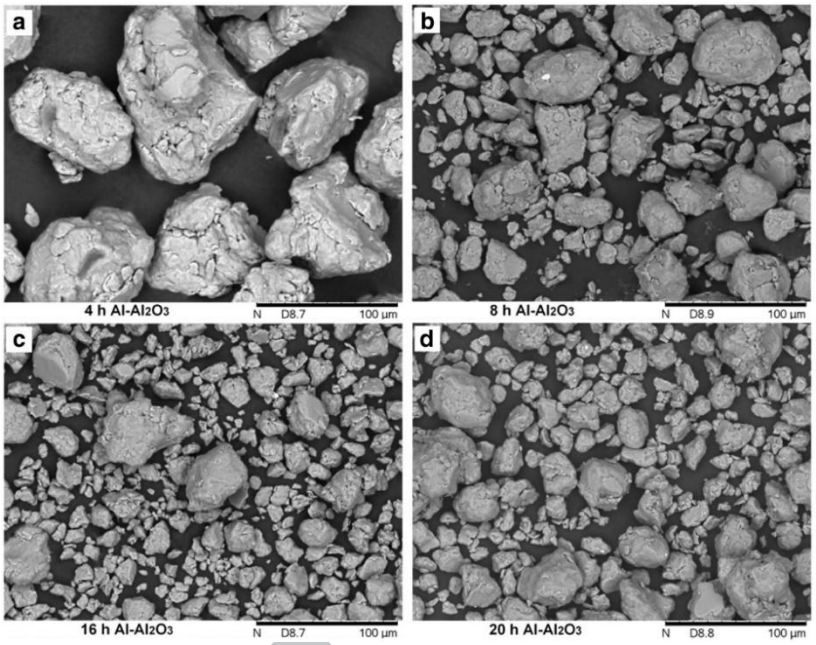

Fig. 6. The morphological evolution of the 4 vol.% Al_2O_3/Al composite powders ball-milled for (a) 4 h, (b) 8 h, (c) 16 h, (d) 20 h (Reproduced from [115], Copyright (2016), with permission from Elsevier).

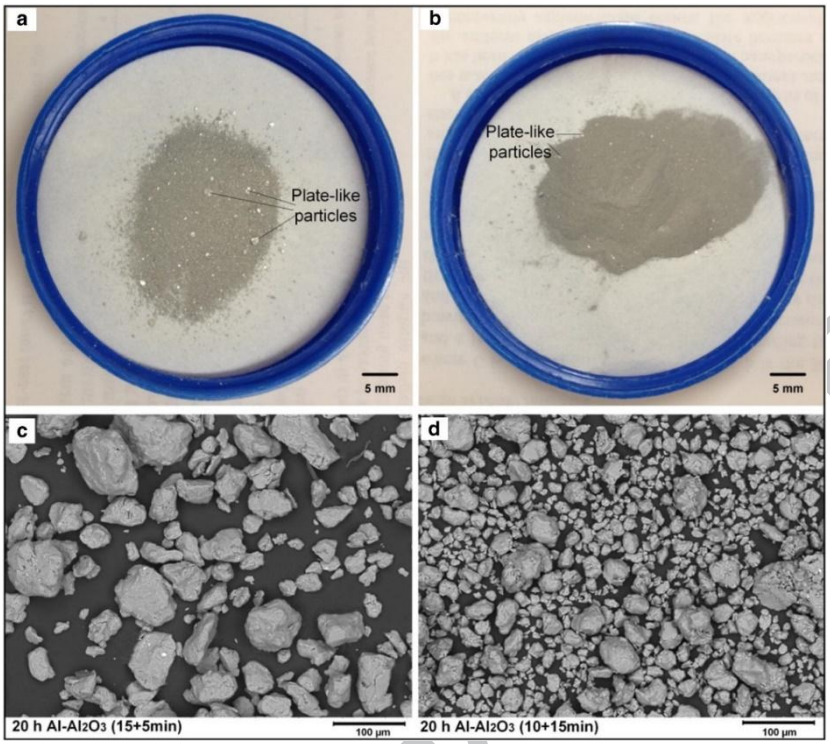

Fig. 7. 4 vol.% Al_2O_3/Al composite powders ball-milled for 20 h with different procedures: (a, c) milling time 15 min following a 5 min pause, (b, d) milling time 10 min following a 15 min pause. (Reproduced from [115], Copyright (2016), with permission from Elsevier).

Table 2 Ball milling parameters for different materials.

Materials	Rotation speed (rpm)	Ball-to-powder weight ratio	Optimum milling time (h)	Raw particle size	Introducing pattern of nanoparticles	Ref.
TiC/Ti	200	5:1	4	Ti 22.5 μm TiC 50 nm	*ex situ*	[102, 136]
TiC/Ti	300	8:1	4	Ti 25 μm TiC 45 nm	*ex situ*	[137]
TiC/AlSi10Mg	200	2:1	4	AlSi10Mg 30 μm TiC 50 nm	*ex situ*	[138]
TiB_2/AlSi10Mg	N.A.	N.A.	48	AlSi10Mg 25 μm TiB_2 60 nm	*ex situ*	[135]
Al_2O_3/Al	350	5:1	20	Al 325 mesh Al_2O_3 <50 nm	*ex situ*	[115]
TiC/316L	200	5:1	8	316 L 45 μm TiC 50 nm	*ex situ*	[131]
TiB_2/ 316L	200	5:1	8	316 L 45 μm TiB_2 2-12μm	*ex situ*	[96]

$TiC/TiAl_3$	250	10:1	25	Ti 30 μm Al 16 μm C 30 μm	*in situ* with dissolution-precipitation	[104]
TiC/316L	82	9:1	4	316L 44 μm Ti 10 μm C 2-12 μm	*in situ* with dissolution-precipitation	[97, 126]
Cr_3C_2/Fe	150	5:1	2	Fe 29.7 μm Cr_3C_2 131 nm	*in situ* with chemical reaction	[120]
$TiB_2/TiAl$	250	4:1	4	Ti-45Al-2Cr-5Nb (at.%) 27.6 μm TiB_2 3-5 μm	*in situ* with chemical reaction	[118]
TiB/Ti	200	5:1	2	Ti 48.69 μm TiB_2 3.5-6 μm	*in situ* with chemical reaction	[134]
TiC/Ti_5Si_3	300	10:1	15	Ti 45 μm SiC 13 μm	*in situ* with chemical reaction	[139]
TiN/Ti_5Si_3	250	10:1	8	Ti 30 μm Si_3N_4 4 μm	*in situ* with chemical reaction	[116]

In situ method with chemical reaction after direct mixing or ball milling is accessible. In such a case, the original size of reinforcement is allowed in micrometer scale. Dadbakhsh *et al.* produced Fe-Al intermetallics reinforced Al/AlSi10Mg/AlMg1SiCu nanocomposites with direct mixing of matrix powders (mean particle size ~ 40μm) and Fe_2O_3 particles (below 53 μm). Very fine (typically around 50 to 100 nm) secondary phases including Al-Fe intermetallics (such as $Al_{13}Fe_4$, Al_5Fe_2, Al_2Fe and Fe_3Al) and Al oxides (such as α-Al_2O_3) form through *in situ* reactions. This method eases the powder preparation but needs careful design of reaction procedure [117]. Various *in situ* systems such as TiB/Ti [119], Cr_3C_2/Fe [120] and TiB_2/Ti-45Al-2Cr-5Nb nanocomposites [118] show the potentials of *in situ* method with ball milling which ensures uniform distribution of powders.

Other *in situ* methods are attainable by pre-alloying without ball milling or direct mixing. Li *et al.* produced uniform powder with TiB_2 nanoparticles using *in situ* pre-alloying method following atomization [78]. A TiB_2 reinforced pure aluminum nanocomposite master alloy was produced with reactive salts of K_2TiF_6, followed by re-melting and addition of both Mg and Al-Si master alloys. Gas atomization was then employed to produce the final composite powder. This method ensures both the spherical morphology and smooth surface of the powders (Fig. 8a). Better flowability of the powders than that obtained with other methods is expected. The distribution of nanoparticles resembles that in ball milling method. The TiB_2 nanoparticles distribute both on the surface of the powder (Fig. 8b) and inside the matrix along the grain boundaries indicated by arrows (Fig. 8c). No nanoparticles were detected in the interior of the grains (Fig. 8d). The size range depends on the gas atomization processing which is easy to control. The only drawback is the

complexity of the fabrication of *in situ* master alloys and gas atomization. The same fabrication method was applied to TiB_2/Al-3.8Cu-1.3Mg alloys [121].

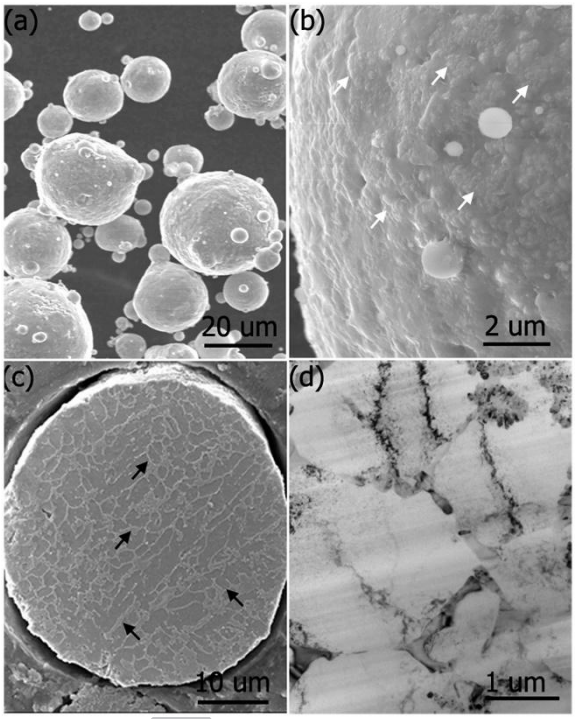

Fig. 8. SEM images of (a) morphology, (b) surface and (c) cross-section of the TiB_2/AlSi10Mg composite powder prepared by *in situ* pre-alloying and gas atomization, (d) TEM bright field image of the powder interior. The white arrows and black arrows indicate the TiB_2 nanoparticles on the surface and in the interior of the TiB_2/AlSi10Mg composite powder (Reproduced from [78], Copyright (2017), with permission from Elsevier).

Another novel strategy is to employ an agent to deposit the nanoparticles on the surface of the matrix powder. Nomura *et al.* prepared Al_2O_3/MoTiAl and Al_2O_3/NiAlCrMo nanocomposite powders by using acid-treated carbon nanotubes (ATCNTs) as a bridging agent [122]. This ATCNT bridging ensures that individual Al_2O_3 particles distribute uniformly on the surface of MoTiAl and NiAlCrMo powders without aggregation.

ATCNTs, Al_2O_3, and MoTiAl/NiAlCrMo suspension in ethanol was separately produced under ultrasonication. A 3 wt.% ATCNT/Al_2O_3 hybrid and following Al_2O_3–ATCNT/MoTiAl or Al_2O_3–ATCNT/NiAlCrMo composite suspension were synthesized by addition of ATCNT/Al_2O_3 hybrid drop by drop into MoTiAl or NiAlCrMo colloid with electrostatic self-assembly effect. The final powders were obtained after completely drying in a vacuum. Fig. 9 and Fig. 10 show the MoTiAl and NiAlCrMo powders coated with 5 wt.% and 10 wt.% Al_2O_3, respectively. It can be observed that the agent bridges the well distributed reinforcement phase and matrix powders and that the Al_2O_3-coated MoTiAl (Fig. 9) and NiAlCrMo powders (Fig. 10) remained almost the same in shape and particle size with the uncoated counterparts. Hence, this method also maintains similar flowability to the raw powders. Although nanoparticles distribute on the surface of the matrix powders, the attractive potential between the constituents enables a strong and irreversible bonding between them than that with direct mixing method. Moreover, no agglomeration can be observed. The limitation only comes from the complexity of the processing and limited surface area for nanoparticles.

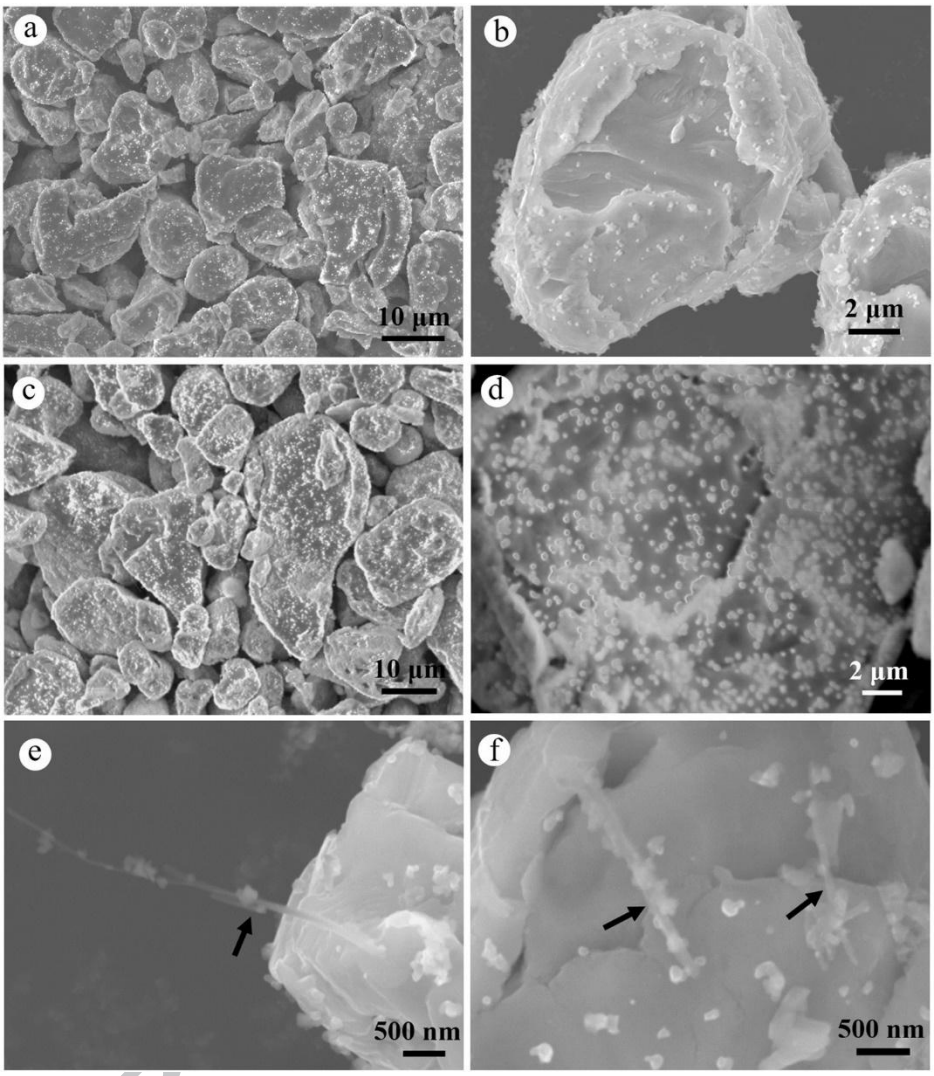

Fig. 9. SEM images of the composite powder. (a, b) 5 wt.% Al_2O_3–0.15 wt.% ATCNT/MoTiAl and (c, d) 10 wt.% Al_2O_3–0.31 wt.% ATCNT/MoTiAl; (e, f) magnification of powder surface with individual ATCNTs (black arrows) bridging the Al_2O_3 and MoTiAl powders (Reproduced from [122], Copyright (2018), with permission from Elsevier).

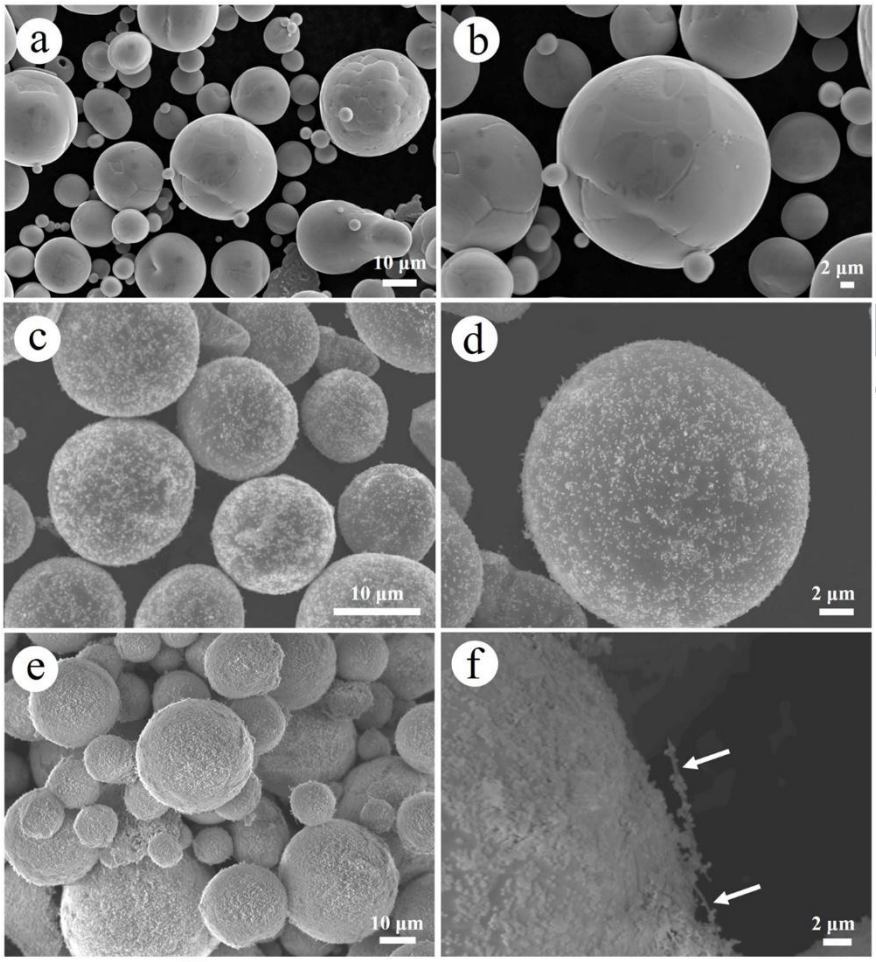

Fig. 10. SEM images of (a, b) raw NiAlCrMo powder, (c, d) 5 wt.% Al_2O_3–0.15 wt.% ATCNT/NiAlCrMo and (e, f) 10 wt.% Al_2O_3–0.31 wt.% ATCNT/NiAlCrMo powders. The white arrows in (f) indicate two individual bridging ATCNTs partially covered with Al_2O_3 nanoparticles (Reproduced from [122], Copyright (2018), with permission from Elsevier).

A similar principle has been used by Tan *et al.* in preparation of TiB_2/AlSi10Mg powders for direct metal deposition (DMD) with aerosol (2.7 vol.% polyvinyl alcohol (PVA) solution) as an agent which can also be applied to SLM [123]. This method resembles both direct mixing and agent deposition. The processing includes direct mixing of AlSi10Mg powder and micro-nano TiB_2 particle followed by spraying with 2 wt.% aerosol and

subsequent mixing. The final step is to dry and sieve the powder mixture. TiB_2 particles distribute on the surface of AlSi10Mg powders as satellite, as shown in Fig. 11. The adherence of the constituents is sufficient to survive powder feeding. Simple operation makes it attractive though the bonding strength is between direct mixing and aforementioned agent deposition.

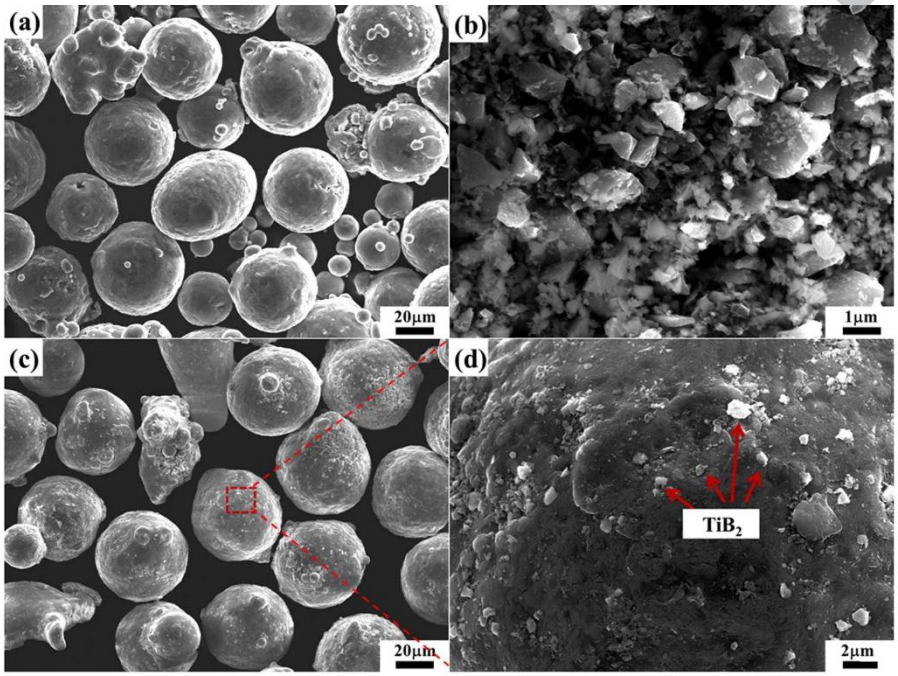

Fig. 11. SEM images of (a) AlSi10Mg powder, (b) TiB_2 particle, (c) satellited TiB_2/AlSi10Mg composite powder with PVA, (d) magnification of powder surface with satellite TiB_2 particles (Reproduced from [123], Copyright (2018), with permission from Elsevier).

The last method is electrodeposition which can maintain good flowability and strong bonding. It can be applied to all kinds of powders, however, at an expensive cost. Ma *et al.* prepared nanocomposites of Al_2O_3/Ni and SiC/Ni powders by electrodeposition [124]. Similarly, nanoparticles were electrostatically assembled to several alloy powders, e.g.

TiB_2/Al7075, ZrH_2/ Ti-6Al-4V, WC/Al7075, WC/AlSi10Mg, TiC/Fe powder (Fig. 12), with uniform distribution in the work of Martin *et al* [107].

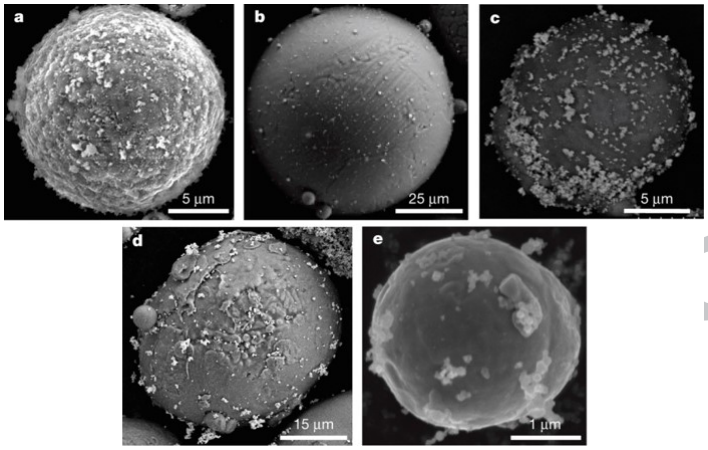

Fig. 12. Nanoparticles electrostatically assembled on metal feedstock. (a) TiB_2/Al7075, (b) ZrH_2/Ti-6Al-4V, (c) WC/Al7075, (d) WC/AlSi10Mg (e) TiC/Fe (Reproduced from [107], Copyright (2017), with permission from Springer Nature).

2.1.2.3 Physical properties change by nanoparticles

Other than powder preparation, modification of properties especially those associated with powder materials is thereafter emphasized to highlight their influence on the SLM fabrication process. There are numerous considerations for the selection of reinforcement. In fact, the influencing factors cannot be considered independently and should be considered comprehensively because any physical and thermal property changes would redistribute the temperature field and incur change in fluid dynamics as well as end applications.

The first property to be considered is laser absorption as it is related to the initiation of the SLM process. Table 3 lists laser absorption of some alloys, ceramics and composite powders. The composite powder feedstock witnesses a significant increase in laser

absorption compared with matrix alloys. Both numerical approximation and experimental measurement have been employed to investigate the laser absorption/reflectivity of the mixture of matrix and ceramic reinforcement. Gu *et al.* calculated the laser absorption of the mixture of AlSi10Mg and TiC by volume fraction using the following equation [140]:

$$A = \sum \alpha_i A_i \quad (4)$$

where α is the volume fraction of one phase, and A_i is the laser absorption of the i phase. This method requires detailed information of the matrices and ceramic particles and is efficient in numerical simulation. In fact, Eq. (4) is more suitable for bulk nanocomposites. Ma *et al.* measured the reflectivity of Al_2O_3/Ni (1.8 vol.%) to be 65.8 % compared with 67.4 % of pure Ni at 1.07 μm wavelength using a power sensor [141]. The slight difference in the laser absorption improvement is probably due to the low fraction and the transparent property of Al_2O_3 to the wavelength. However, Eq. (4) is popular in numerical simulation and qualitative approximation because of ease of estimation.

Table 3 Laser absorptivity of some alloys, ceramics and composites powders.

Material	Absorptivity	Ref.
AlSi10Mg	0.09	[100]
Ti	0.37	[142]
TiC	0.82	[143]
TiC/ Inconel 718	0.72	[144]
TiB_2/AlSi10Mg	0.71	[78]
TiB_2/Al-3.8Cu-1.3Mg	0.57	[121]

Unfortunately, the authors did not take granulomorphometry (particle size and surface area) into consideration and assumed that the apparent density remained the same. With this approximation, there is limited accuracy compared with experimental data. Nonetheless, it

is still acceptable because most ceramics show higher laser absorption and the same trends can be estimated. For example, Li *et al.* measured the reflectivity of the nanoscale TiB_2 decorated AlSi10Mg alloys (~7 vol.%) at 1.06 μm laser wavelength with diffuse reflectance spectroscopy [78]. The result (~29 %) is lower than that of normal AlSi10Mg powder which is ~37 %. Similar phenomenon is reported in TiB_2/Al-3.8Cu-1.3Mg composite powder. According to Eq. (4), mixture of ceramics with lower laser absorption would degrade the property compared with matrix alloys [121]. However, it is demonstrated that even for ceramics with lower laser absorption (e.g. the absorption of Al_2O_3 is lower than that of MoTiAl alloy), the laser absorption of the mixture witnesses an increase due to the increment of surface roughness. Fig. 13a shows the laser absorption of ATCNTs, Al_2O_3, MoTiAl raw powder and the mixtures of different volume fraction, respectively. Obviously, the mixtures show higher absorption and it even increases with particle volume fraction. The principle lies in the fact that the increase in surface roughness leads to multiple reflections and multiple absorptions of the laser which enhances the absorption to a large extent consequently, illustrated in Fig. 13b. It is consistent with the established fact that laser absorption on a rough surface could be increased by an order of magnitude over that of a perfectly flat surface [145, 146]. In the results, ATCNTs show little effect on the absorptivity, mainly because they are in between the Al_2O_3 and MoTiAl powders, acting as an agent and exposing little of themselves to the laser.

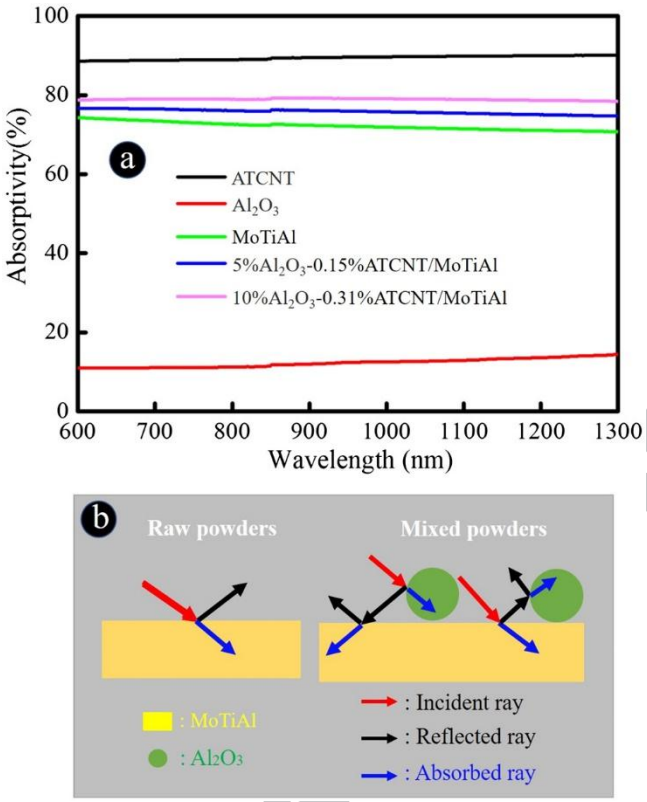

Fig. 13. (a) Laser absorptivity of ATCNTs, Al_2O_3, MoTiAl, 5 wt.%Al_2O_3–0.15 wt.%ATCNT/MoTiAl, and 10 wt.%Al_2O_3–0.31 wt.%ATCNT/MoTiAl powders as a function of laser wavelength, (b) schematic illustration revealing the difference in laser absorptivity between raw MoTiAl and Al_2O_3-ATCNT/MoTiAl mixed powders (Reproduced from [122], Copyright (2018), with permission from Elsevier).

Further consideration of the thermo-physical properties of the powder mixture is the thermal conductivity [140]. The effective thermal conductivity (k_{eff}) of the powder system is estimated by the following equation [71],

$$\frac{k_{eff}}{k_f} = \left(1-\sqrt{1-\varphi}\right)\left(1+\frac{\varphi k_r}{k_f}\right) + \sqrt{1-\varphi} \times \left[(1-\phi)\left(\frac{2}{1-\frac{Bk_f}{k_s}}\left(\frac{B}{\left(1-\frac{Bk_f}{k_s}\right)^2}\left(1-\frac{k_f}{k_s}\right)\ln\left(\frac{k_s}{Bk_f}\right) - \frac{B+1}{2} - \frac{B-1}{1-\frac{Bk_f}{k_s}}\right) + \frac{k_r}{k_f}\right) + \phi\frac{k_s}{k_f}\right] \quad (5)$$

where φ is the porosity of the powder bed, k_f is the thermal conductivity of the gas inside the pores of the powder bed, k_s is the thermal conductivity of the solid, ϕ is the fraction of flattened surface a particle in contact with another particle, B is the deformation parameter of the particle. When B=1, the particle is spherical; B<1, it exhibits as prolonged needle; B>1, it is a barrel-like. k_r is the thermal conductivity of the powder bed owing to radiation among particles and is equal to [147],

$$k_r = 4F\sigma T^3 x_r \quad (6)$$

where F is a view factor which is approximately taken as 1/3, σ is the Stefan-Boltzmann constant, T is the temperature of the powder particles, and x_r is the average diameter of the powder particles.

The effective thermal conductivity is affected by the gas fraction (φ), the morphology of the powder (B, ϕ), and the thermal conductivity of the solid (k_s). Nanoparticles increase the gap between the metallic powders by adhering to them and roughening their surfaces [148]. The morphology of powder in ball milling method changes from spherical to near spherical or irregular shape. The foregoing discussion implies an increase in both φ and ϕ. Ceramic phases would cause properties change in the bulk composites, which in return affect the effective thermal conductivity. Ma *et al.* investigated the correlation between thermal conductivity and nanoparticle fraction and a descending trend of thermal conductivity with

increasing nanoparticle fraction was observed [141]. Nanoparticles decrease the thermal conductivity no matter whether they have a higher or lower thermal conductivity than the matrices because they introduce interfacial thermal resistance and scatter the energy carriers (electrons and phonons) [149-155]. The change induced by nanoparticles leads to the reduction of the effective thermal conductivity. Both reductions in thermal conductivity of powder and bulk system lead to a slower heat conduction among powders and in the previous bulk layer during SLM.

Considering the above changes, it is established by many researchers that introduction of the nanoparticles affects the size of melted zone (MZ) and heat affected zone (HAZ) compared to the matrix alloys. Ma *et al.* compared the size of MZ and HAZ of Ni, Al_2O_3/Ni and SiC/Ni nanocomposites with same laser energy input. MMNCs process an increasing MZ depth and shrinking HAZ size [124]. In fact, laser absorption significantly affects the heat absorption and results in an enlarged melt pool and high temperature. One of the possible reasons for shrinking HAZ is that the nanoparticles reduce the thermal conductivity of the bulk composites underneath and thus decrease the conductive heat transfer to the base materials. Gu *et al.* revealed similar phenomena and demonstrated that the effect increases with the volume of particles [140]. As plotted in Fig. 14, the surface temperature contour of the melt pool increase with TiC contents increasing from 2.5 wt.% to 7.5 wt.%. The highest temperature in the melt pool reaches 1460 K, 1580 K and 1670 K with 2.5 wt.%, 5 wt.% and 7.5 wt.% reinforcement, respectively.

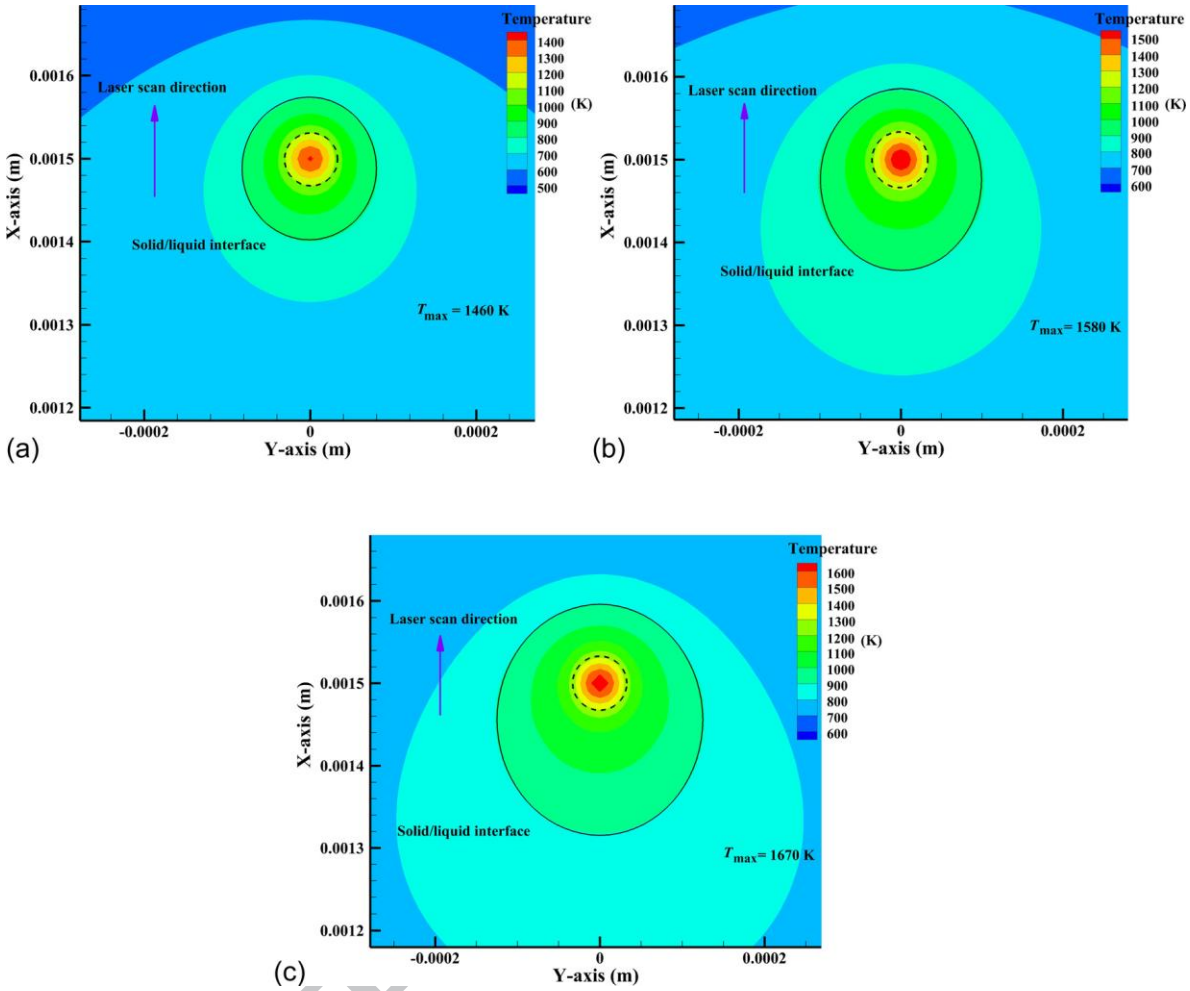

Fig. 14. Temperature contour of top surface of melt pools with different TiC contents of: (a) 2.5 wt.%, (b) 5.0 wt.%, and (c) 7.5 wt.%. The positions of laser beam were circled by dashed line (Reproduced from [140], Copyright (2015), with permission from AIP Publishing).

Fluid flow in the melt pool is mainly dominated by thermo-capillary force and viscous drag force [70], highlighting the importance of surface tension and viscosity. Ma *et al.* measured the surface tension of Al_2O_3/Ni nanocomposites at 1500 ^oC and demonstrated the decreasing trends of surface tension versus nanoparticle fraction although the plot slope varies among different nanocomposites due to the nature of various metals and ceramics

[156]. The same trend can be observed in Gu *et al.* research which shows that surface tension of TiC/AlSi10Mg nanocomposite decreases with the volume fraction of TiC particles when viewed at the same temperature [140]. However, it is the surface tension gradient which is inversely proportional to the temperature gradient of the melt pool that matters most. Higher laser absorption and slower heat dissipation enlarge the melt pool size and temperature gradient. Bigger difference of temperature gradient and surface tension gradient can be observed with the increase of TiC particles, evidenced by increasing Ma number.

Ceramics possess high melting point and thus remain solid in the melt pools, resulting in significant increase in viscosity, especially with high volume of nanoparticles [156]. The distribution state of nanoparticles reinforcement mainly depends on the interaction between the reinforcing particles and the thermo-capillary flow which is determined by the above competitive factors, increasing temperature gradient and viscosity. In addition to the effects on fluid flow caused by the nanoparticles, there is a counterforce to the particles. Fig. 15 shows the influence of TiC volume fraction on the particle velocity distribution in melt pools. Low reinforcement content (2.5 wt.% in Fig. 15a) corresponds to low heat absorption and low Marangoni flow, and thus the fluid velocity direction remains almost the same when passing through the particles. At higher reinforcement content (5 wt.% in Fig. 15b), the Marangoni flow is intensified and a circular flow appears when the convective flow passes through the TiC particles. A ring-like structure in the final MMNCs is thus formed with TiC particles trapped into the circular flow. Further increasing of volume fraction (7.5 wt.% in Fig. 15c) causes a larger circular flow and coarsening of the structures. Fig. 16 shows the distribution of TiC in AlSi10Mg matrix with different volume

fraction, revealing no-ring structure and ring-like structures of different sizes [140]. AlMangour *et al.* investigated both TiC/316L stainless steel and TiB_2/316L stainless steel nanocomposites and demonstrated similar microstructural evolution of ring-like structure. There is also a threshold for the ring-like structure, exceeding which the ring-structure starts coarsening, i.e., 5 vol.% for TiC and 10 vol.% for TiB_2 [108, 131]. Hao *et al.* revealed similar distribution of hydroxyapatite in 316L stainless steel matrix [157].

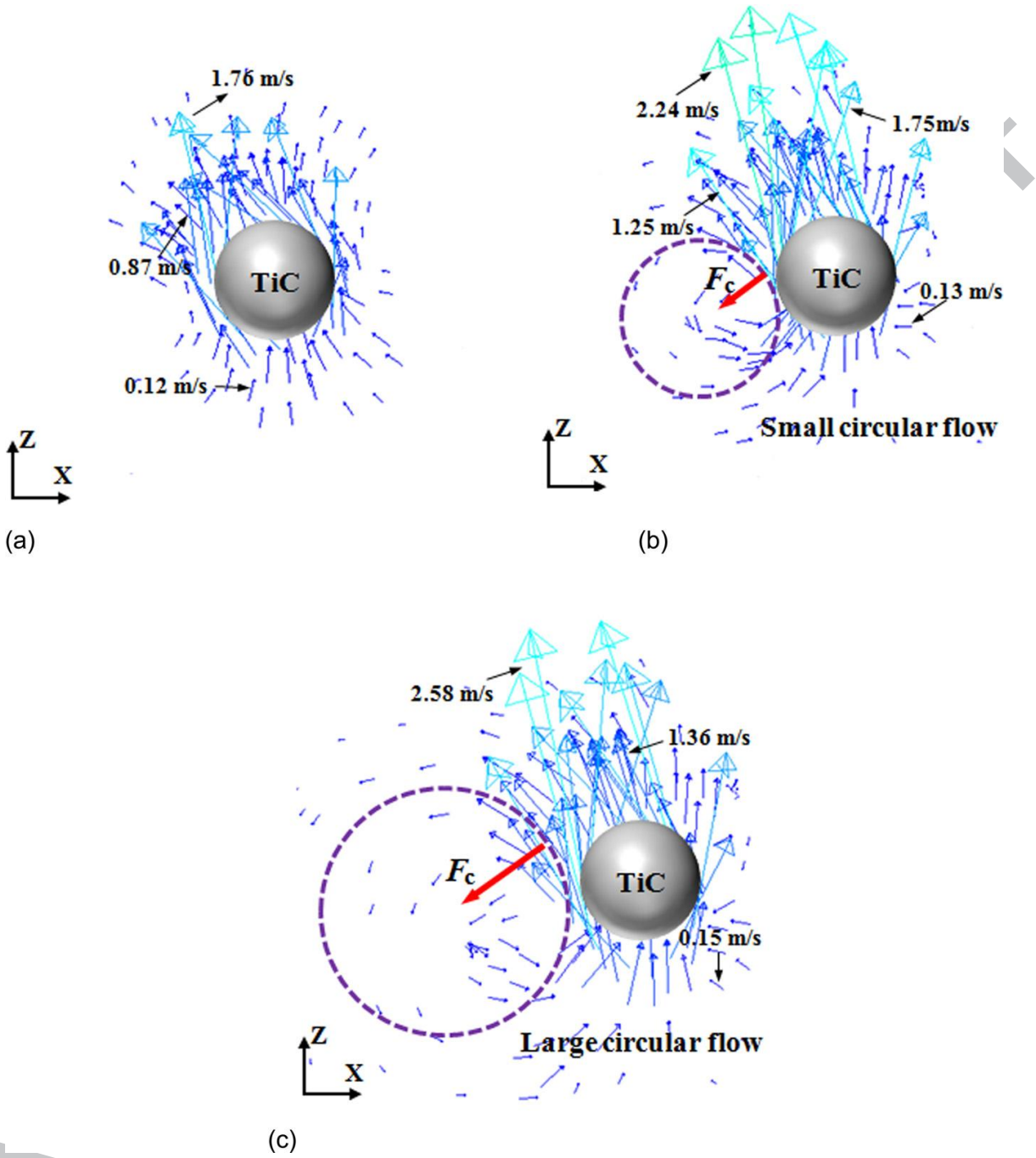

Fig. 15. Plots of velocity vector around a TiC particle within the melt pool at different TiC contents: (a) 2.5 wt.%, (b) 5.0 wt.%, and (c) 7.5 wt.% (Reproduced from [140], Copyright (2015), with permission from AIP Publishing).

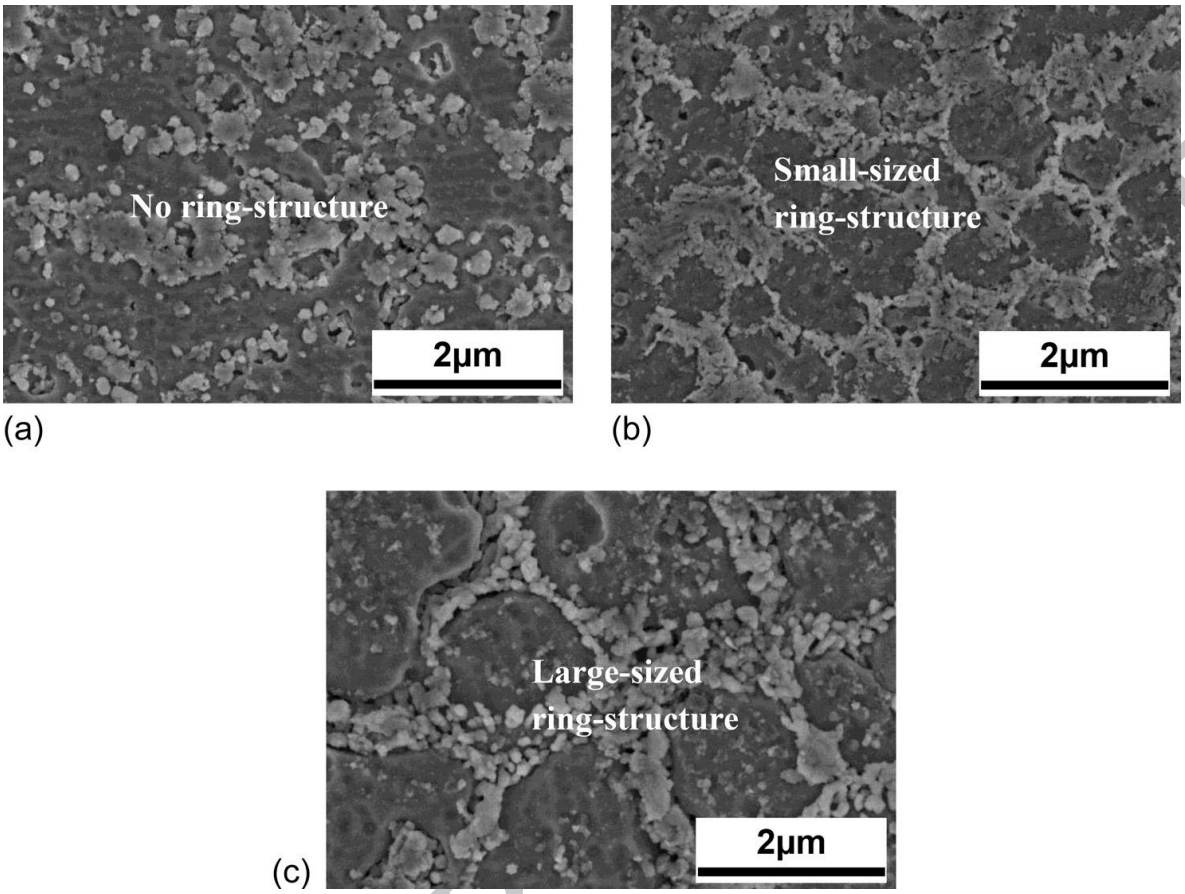

Fig. 16. SEM images of typical microstructures of TiC/AlSi10Mg nanocomposites fabricated by SLM with different TiC contents of: (a) 2.5 wt.%, (b) 5.0 wt.%, and (c) 7.5 wt.% (Reproduced from [140], Copyright (2015), with permission from AIP Publishing).

2.1.3 Interface

Interface between matrix and reinforcement is a special region which affects most mechanical and physical properties, such as strength, fatigue, creep, coefficient of thermal expansion (CTE) and thermal conductivity [5]. The influence of interface in MMCs is highlighted in fibre-reinforced composites. In particle reinforced MMNCs, it also receives considerable interest. The interface type can be categorized based on the compatibility between the matrix and reinforcement, i.e. (1) not reactive and insoluble, (2) not reactive

but soluble (e.g. W/Cb), and (3) reactive (e.g. Ti-B, Ti-SiC). Reactive refers to chemical reaction between matrix and reinforcement and a new chemical compound (or compounds) to connect them. Reactive type bonding is supposed to be a weak interface bonding, as it contains typical growth defects which degrade the bonding [158]. However, Rong *et al.* investigated the graded interface and the diffusion layer in WC/Inconel 718 composite and found that the gradient interface shows an important role in improving the wear performance [159]. In fact, coherent or semi-coherent bonding shows positive effects in MMNCs. High resolution transmission electron microscopy (HRTEM) is usually employed to study the characteristics of the interface. Better bond integrity at the Al/TiC interface was found compared to Al/SiC, Al/B_4C and Al/TiB_2 interfaces [160]. Semi-coherent bonding with orientation relationships $(0001)_{Al_3BC}//(1\bar{1}1)_{Al}$ between Al_3BC/Al was observed and highly valued to the strength increase [161].

In MMNCs synthesis, desirable interface is favored by good wetting ability. In conventional method, wetting can be promoted by (a) alloying the metallic matrix with reactive materials, (b) applying metallic coatings to the ceramic particulates and (c) heat treating the ceramic particulates [162, 163]. It is demonstrated by Zheng *et al.* that Ni-coated TiC microscale particles could offer superior flowability of the mixed powders, improving the integrity of the interface between the matrix and the reinforcement [164, 165]. Yuan *et al.* also produced AZ91 alloys reinforced with carbon nanotubes coated with MgO, taking advantages of the semi-coherent bonding between Mg and MgO [166]. This provides insights into developing new methods to distribute the nanoparticles and increase their wettability with the matrix. However, it is challenging to coat the nanometer scale powder.

2.2 SLM processing parameters

The significant processing parameters involved in SLM include laser power (*P*), scanning speed (*v*), hatch spacing (*h*), layer thickness (*d*), and scanning strategy. Extensive research has been carried out on various alloys [167-169]. In fabrication of the nanocomposites, the relationship between densification and processing parameters resembles the one in production of metal and alloy parts, except there is a processing window shift in nanocomposites. Microstructures corresponding to the distribution of nanoparticles also depend on the processing parameters and would be detailed in this section. Scanning strategy should always be emphasized because isotropy can be well controlled.

2.2.1 Influence of laser power, scanning speed, hatch spacing and layer thickness

The individual parameters *P*, *v*, *h* and *d* can be intergrated into one equation:

$$\varepsilon = \frac{P}{v \cdot h \cdot d} \tag{7}$$

where ε represents laser energy density [170]. The discussion of densification behavior depending on parameters can be attributed to the variation of laser energy density, which corresponds to a processing window for different parameters combination. Since each metal has a characteristic laser absorbance and thermal properties, extensive experimental work has been typically carried out to obtain a processing window that can lead to a production of fully dense parts, beyond or below which degradation of the performance occurs [171, 172].

Energy input determines the heat transition modes, i.e. keyhole mode and conduction mode (Fig. 17), distinguished by whether boiling point is exceeded in the melt pool. As

shown in Fig. 17, size distribution of three zones including deposition zone (DZ) on the top, re-melting zone (RZ) of previous part and HAZ in the peripheral area of melt pool also distinguishes the two modes. The length of RZ in keyhole mode is larger compared with conduction ones, penetrating deep in previous layers. These two modes are related to densification behavior. Yang *et al.* plotted a parameter map of high relative density and revealed a limited region in keyhole mode whilst a wide region in conduction mode [173], indicating an easy access to fully dense parts in conduction mode with less energy input. In keyhole mode, significant vaporization of materials and resultant keyhole pores lead to relatively high porosity. On the other hand, stable melting track and less defects are more attainable in conduction mode.

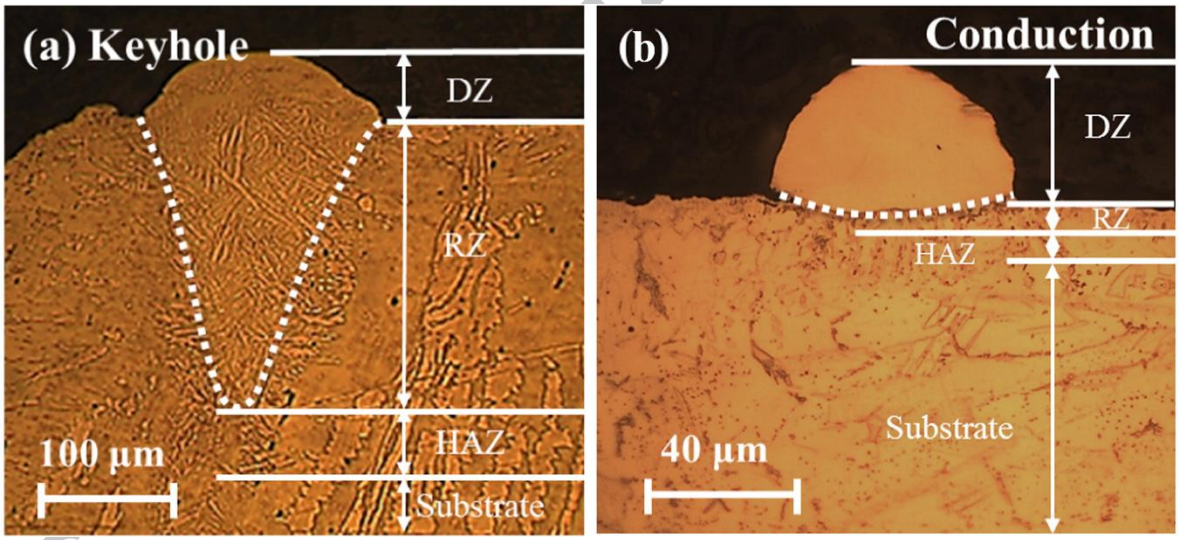

Fig. 17. Macro-morphology of keyhole (a) and conduction (b) melt pools (Reproduced from [173], Copyright (2016), with permission from Elsevier).

Yadroitsev *et al.* asserted that maximum temperature of melt pool significantly increases with increase in laser power and slightly decreases with increase in scanning speed [174]. In contrast, Yang *et al.* investigated the threshold for keyhole mode and highlighted the

importance of laser energy density associated with scanning speed, laser power and layer thickness, among which scanning speed is the main factor, followed by laser power and layer thickness [173]. Lower scanning speed indicates longer duration between laser and materials with more energy input and may facilitate keyhole mode. Higher laser power and thinner layer thickness show the same trends. Extreme low scanning speed, high laser power and thin layer thickness result in an increase in melt temperature and RZ depth. In keyhole mode, vaporization occurs and vapor would be entrapped into the tracks, known as keyhole pores. The vapor recoil pressure also causes distortion and instability of the scanning tracks. In such a case, SLM process is accompanied by keyhole pores and irregularity of the tracks, leading to low relative density of the produced parts. Attar *et al.* revealed keyhole pores in TiB/Ti composite and a decreasing relative density when laser energy density increasing from 120 J/mm^3 to 135 J/mm^3 [134].

High densification is more attainable in conduction mode as a wider region for parameters selection is available in Yang *et al.* research [173]. Nevertheless, careful optimization is necessary to avoid defects and imperfection. Many scholars demonstrated that continuously increase of scanning speed in conduction mode witnesses a transition of melting track from continuous to discontinuous and finally balling effects (Fig. 18) [55, 175]. When the laser energy is not enough to ensure the wetting ability, the melt pool with small dimension tends to become unstable with small circumference-to-length ratio [55, 176]. The unstable longer melt pool tends to become discontinuous with necking and break up into balling finally. This transition is associated with laser power and layer thickness as they also affect the energy density. Lower laser power leads to lower energy input and resembles higher scanning speed. Although a larger layer thickness enables a bigger melt

pool [177-179], a relatively smaller contact area between melt pool and substrate or previously solidified layer appears when the melt pool is far away from the substrate or previously solidified layer, which results in balling effect and poor densification. Hatch spacing would not affect this phenomenon because its effect is normal to the scanning direction with no relation to the depth of the melt pool.

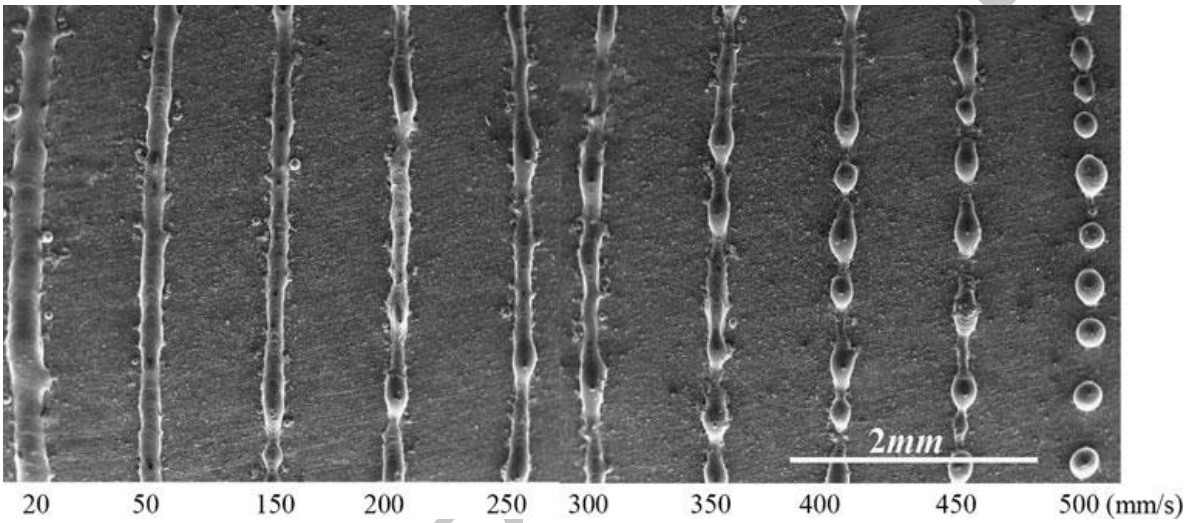

Fig. 18. SEM images of single scan tracks showing change from continuous to discontinuous and balling (from left to right) under different scanning speeds (Reproduced from [178], Copyright (2011), with permission from Springer Nature).

Based on the above discussion, the relative density versus the energy density follows a trend of increasing to a critical value followed by decreasing afterwards. The same is true for the individual parameters that critical values exist. Most scholars focus on the laser power and scanning speed as they are the most variable parameters. The orange area in Fig. 19 illustrates the processing window of laser power *P* and scanning speed *v* for most alloys reproduced on the basis of the iron-based powder (50 wt.% Fe, 20 wt.% Ni, 15 wt.% Cu and 15 wt.% Fe_3P) with layer thickness 250 μm, hatch spacing 100 μm and laser spot

diameter 80 μm. No connection, bonding with smooth and regular surface, and balling effects cover the overall domains. This map shape applies for almost all powders unless the boundaries vary with materials [180]. Olakanmi and Song *et al.* also showed this processing window distribution in pure aluminum, Al-Mg, Al-Si and Ti-6Al-4V alloys [86, 181]. Detailed discussions about the formation of different regions have been addressed elsewhere [53]. The determination of processing parameters for different alloys requires vast investigation. Although not enough data have been collected to map this processing window for MMNCs, it is reasonable to predict that the smooth and regular domains are narrower than those of the matrix alloy counterparts. The processing window will also undergo an offset to higher laser power and slower scanning speed areas for *ex situ* MMNCs fabrication, because the effect of significant increase in viscosity of the melts usually overweighs the influence of increase in temperature and hampers the accessibility to AM. The blue area in Fig. 19 illustrates the offset trends of the smooth and regular domains of *ex situ* MMNCs compared with the corresponding matrix alloys, which was evidenced in literatures [87, 136]. Higher content of nanoparticles leads to higher viscosity and larger offset towards the upper left corner of the panel [182, 183]. Further investigation is necessary to ascertain the processing windows for different MMNCs. However, for MMNCs fabricated with *in situ* reactions it is difficult to predict the change of processing windows as the influence is complex. According to the literatures [116, 139], plenty of *in situ* MMNCs fabrication undergoes exothermic reactions with extra heat assisting the SLM process to achieve better melting. In this case, the processing windows for *in situ* MMNCs can be determined by manipulating the contradictory factors: inclusions and released heat. Expanding processing windows towards higher scanning speed and lower laser power are

expected with the nanoparticles content at low level. For example, Fe_2O_3/Al [184] MMNCs witnessed this phenomenon. When the content of nanoparticles increases, an offset of the processing window towards high energy is predicted as the effect of inclusions dominates the melts. Coarsening of "*in situ*" reinforcements at high laser energy is also a consideration when optimizing the processing parameters. Therefore, the determination of the *in situ* processing parameters is more elaborate.

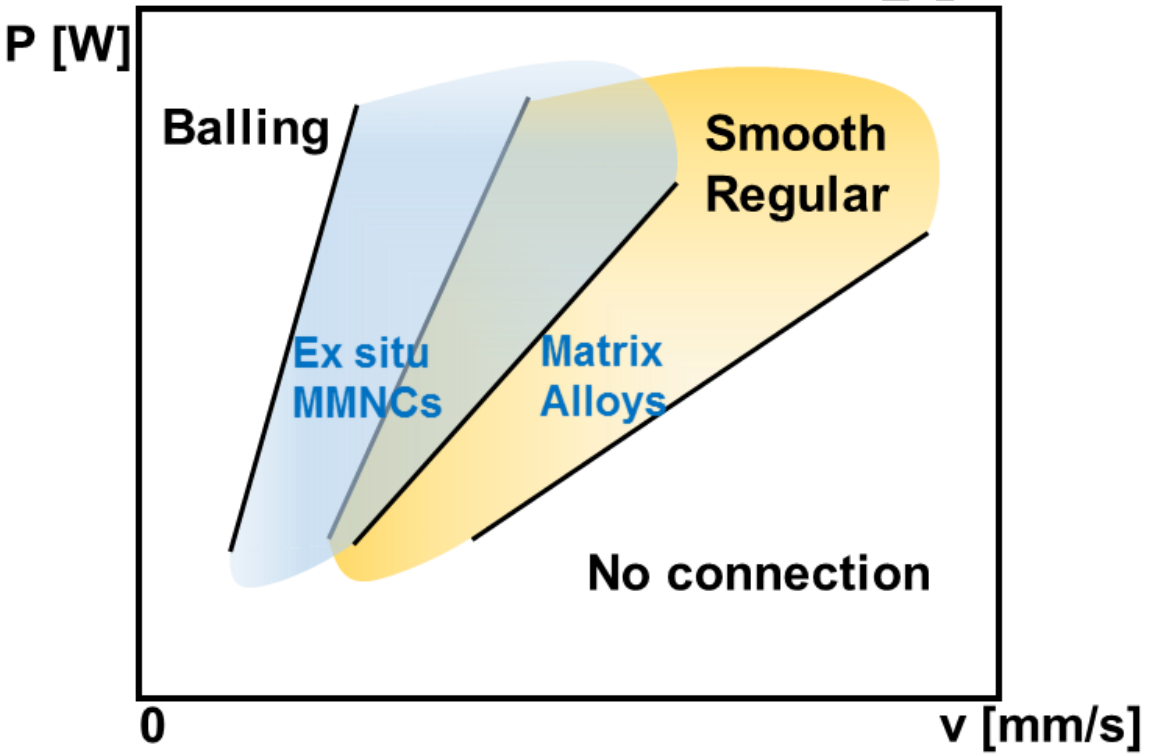

Fig. 19. Schematic of processing windows for MMNCs and corresponding matrix alloys. (Reproduced from [180], Copyright (2004), with permission from Elsevier).

Overlapping hatches are expected to eliminate defects upon repeated re-melting of the tracks during continuous laser passes. Hatch space is a significant variable to determine the energy density and thus the porosity, pore size and shape, according to different overlapping conditions of single laser scanning tracks. Like hatch spacing, layer thickness

is essential to layer bonding and relative density. When a thicker layer thickness is chosen, poor interlayer bonding and residual pores are expected because more input energy would be consumed in melting the powder particles with less heat left for re-melting of the previous layer. Qiu *et al.* simulated melt pool behavior and asserted that thick powder layers tend to intensify the interaction between the laser beam and the melt pool with significant melt splashing and increasing velocity of melt flow within the melt pool. They also validated that increasing powder layer thickness resulted in rapid increase in porosity level and surface roughness with experimental evidence [179].

Mishra *et al.* asserted that there exists a simple linear relation of hatch spacing or layer thickness to the overlapping cross sections and thus to the relative density [185]. Many researchers reported a monotonous increasing relative density with the hatch spacing or layer thickness [186-188]. However, in other research, there exists a threshold for hatch spacing [189, 190] and layer thickness [177, 191] below which decreasing them would deteriorate the relative density. Tang *et al.* established an inequation in which sufficient overlap of melt pools could be obtained [192-194]:

$$\left(\frac{H}{W}\right)^2 + \left(\frac{L}{D}\right)^2 \leq 1 \tag{8}$$

where H is the hatch spacing, L is the layer thickness, W is the melt pool width, and D is the melt pool depth.

2.2.2 Influence of laser energy input on microstructure

The influence of processing parameters on microstructure or on the distribution of nanoparticles which is material system-specific, is essential in MMNCs. Three main types of particle distribution would be addressed in this section.

Firstly, when the melting temperature of the reinforcement is much higher than the matrix and dissolution is negligible, the structure depends on the laser energy density input. No ring structure with severe agglomeration is observed at low energy input. With the increase in energy density, ring-structure forms gradually and tends to coarsen when the energy density exceeds a threshold. Fig. 20 shows the structural evolution in TiC/AlSi10Mg nanocomposites. A continuous and refined ring-structure is formed with laser energy density 160 J/mm^3 [138]. Beyond the threshold is a coarsened ring-structure while below the threshold the ring-structure disappears gradually. This features are also observed in various nanocomposite systems, e.g. AlN/AlSi10Mg [101], TiC/316L [97] and TiB_2/316L [108].

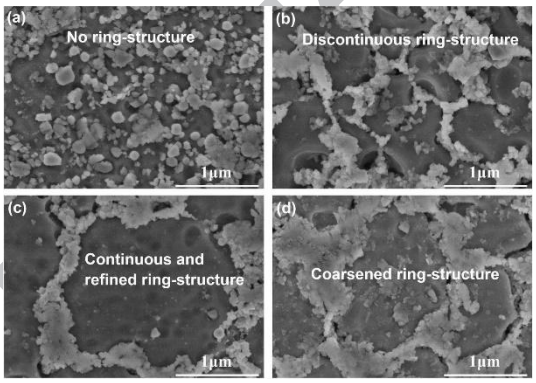

Fig. 20. SEM images of typical microstructure of TiC/AlSi10Mg nanocomposites fabricated by SLM at different laser energy densities: (a) 160 J/mm^3; (b) 200 J/mm^3; (c) 240 J/mm^3; (d) 280 J/mm^3 (Reproduced from [138], Copyright (2015), with permission from Elsevier).

This kind of structures mainly depends on migration of particles which in turn relies on the intensity of the Marangoni flow. For instance, Fig. 21 reveals the melt flow velocity vector near the reinforcement particle AlN in the melted AlSi10Mg matrix depending on

the laser energy input and offers a possible explanation of the formation of random and ring-like structures. At low energy density, the flow direction is almost kept unchanged when passing through the particles, forming the random distribution of nanoparticles. As the velocity of the melt convection tends to be significantly enhanced when the melt flows through the reinforcement particles, a concave pattern of the melt convection forms in the neighboring region of the particles. The velocity increases with the increasing energy input until a symmetrical convection pattern and a circular flow form near the reinforcing particles. The AlN particles tend to be trapped into the circular flow, forming a unique ring structure in the finally solidified materials.

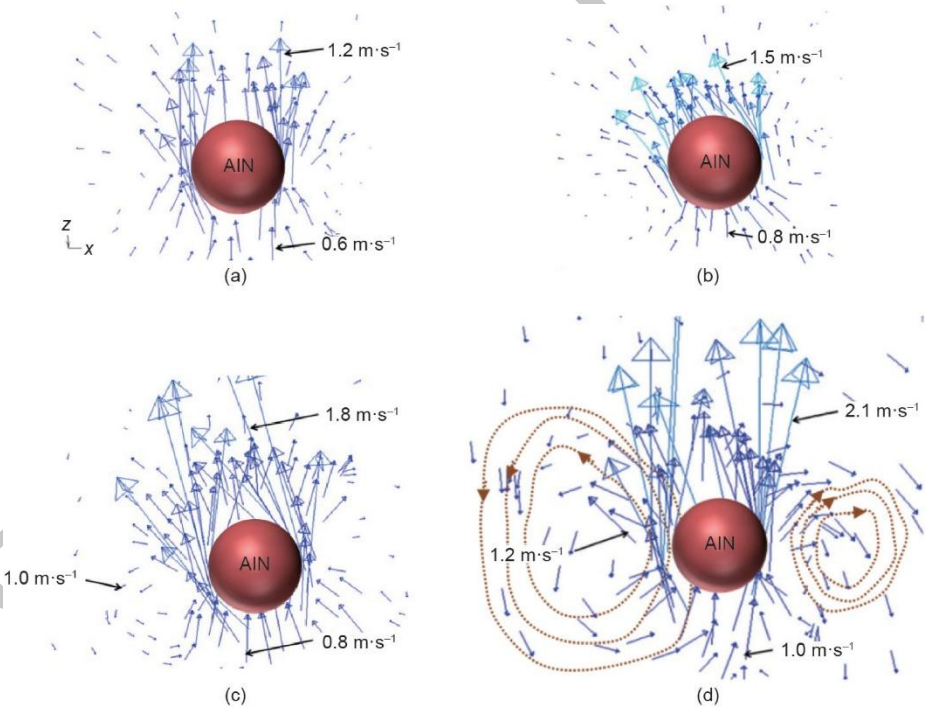

Fig. 21. Plots of velocity vector around AlN particles in AlN/AlSi10Mg composite melts with various SLM processing parameters. (a) P = 100 W, ε = 550 J/mm^3; (b) P = 130 W, ε = 660 J/mm^3; (c) P = 150 W, ε = 830 J/mm^3; (d) P = 180 W, ε = 1000 J/mm^3 (Reproduced

from [113] with no changes. DOI: https://doi.org/10.1016/J.ENG.2017.05.011. Creative Commons user license: https://creativecommons.org/licenses/by/4.0/).

Secondly, when the particles inside the matrix tend to dissolve and solidify during the cooling process, e.g. TiC/Ti composite (Fig. 22), the structure also depends on the energy density input. In such a case, large energy density (360 J/mm^3 and 180 J/mm^3 in Fig. 22a and b, respectively) allows collaboration and coarsening of TiC dendrite grains, while the lower energy density (120 J/mm^3 and 90 J/mm^3 in Fig. 22c and d, respectively) favors the optimum microstructure of nanometer sized lamellar structure. Coarse grains in microscale would not offer the advantages of the MMNCs. Unfortunately, in this research, the parts with nanostructures exhibited inferior densification to those with microscale reinforcement under high energy density. These contradictory features found a compromise at ε = 120 J/mm^3 when 97 % relative density was achieved with nanoscale reinforcement, favoring the optimal mechanical properties. He *et al.* reported similar nanoscale lamellar structures in TiC/Ti nanocomposites at ε = 143 J/mm^3 [137], and the TiC lamellar layer was thicker than that in Fig. 22c and d as expected.

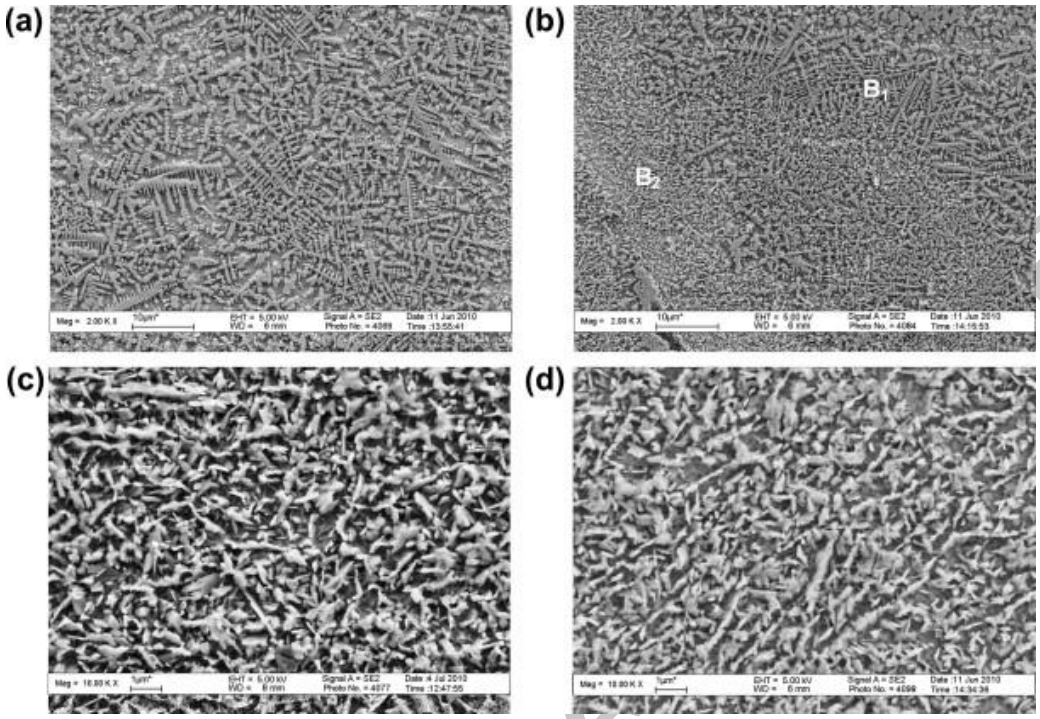

Fig. 22. SEM images of typical microstructure of TiC/Ti nanocomposite parts fabricated by SLM with various energy densities of: (a) 360 J/mm^3; (b) 180 J/mm^3; (c) 120 J/mm^3; (d) 90 J/mm^3 (Reproduced from [136], Copyright (2011), with permission from Elsevier).

The third structure type which is more material system-specific is reported in *in situ* synthesis method. *In situ* synthesis mechanism includes dissolution-precipitation and chemical reaction. An example of dissolution-precipitation mechanism is TiC extracted in Ti-Al matrix (Fig. 23). With the increasing laser power from 700 W to 725 W, 800 W, 875 W and 900 W (other parameters were fixed at v = 100 mm/s, h = 150 μm, t = 150 μm), the morphology of TiC grains changes from a laminar structure to thickened laminar, octahedral, truncated near-octahedral and near-spherical shape. The growth mechanism of the *in situ* formed reinforcements depends strongly on the energy input [103]. For *in situ* chemical reaction system, the dependence principle resembles that in the dissolution-

precipitation although it is system-specific regarding to different crystals. It is found that the grain size and thickness of *in situ* chemical interface is directly proportional to the applied laser energy input, with more energy and time causing more growth of the grains [113].

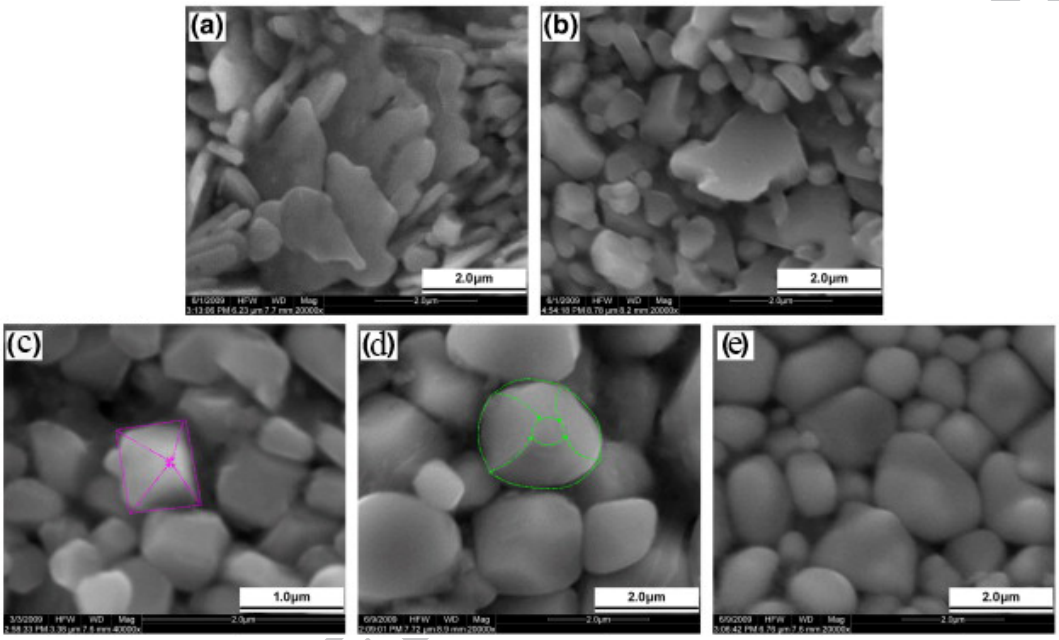

Fig. 23. SEM images of typical morphologies of TiC grains extracted from TiC/TiAl nanocomposite parts fabricated by SLM with various laser power of: (a) 700 W; (b) 725 W; (c) 800 W; (d) 875 W; (e) 900 W (Reproduced from [103], Copyright (2009), with permission from Elsevier).

2.2.3 Influence of scanning strategy

Apart from the inherent porosity in SLM, a strong-textured microstructure tends to develop due to the directional heat flux and large thermal gradient [195]. Although energy input parameters are proven to affect the textures [196], scanning strategies are supposed to offer easier manipulation to eliminate strong textures. Various scanning strategies have

been developed in pursuit of components with full density and controllable texture. Three main basic strategies, i.e. unidirectional, bidirectional, chessboard or island strategies, are well employed in SLM (Fig. 24a, b and d). There are some variants derived from these three basic strategies with rotation for a certain angle (e.g. 60° [197] or 90° [114]) or shift for a certain distance between the layers [198]. Unidirectional scanning is the simplest strategy and generally leads to least densification and strongest texture while other variants show superior densification behavior [183]. The improvement on densification of other strategies depends on materials and other processing parameters. For instance, insignificant change was reported in the research of Thijs *et al.* [198].

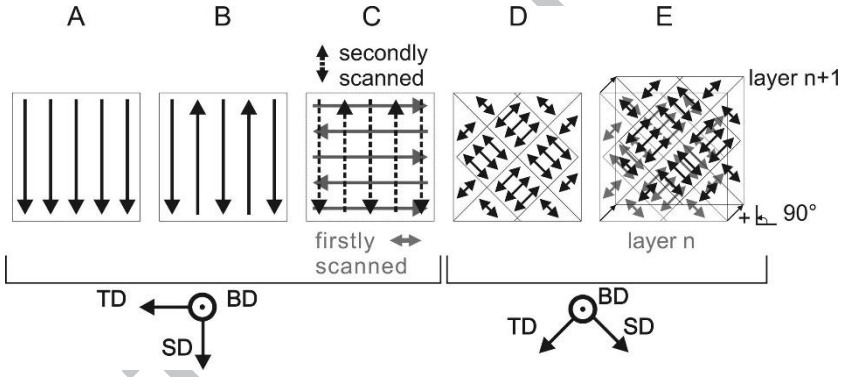

Fig. 24. Overview of various scanning strategies. The building (BD), scanning (SD) and transverse direction (TD) are indicated. A, unidirectional strategy, B, bidirectional strategy, C, bidirectional strategy with 90° rotation between layers, D, island strategy with 90° rotation but without shift between layers, E, island strategy with 90° rotation and 1 mm shift between the layers (Reproduced from [198], Copyright (2013), with permission from Elsevier).

In Fig. 24, five strategies (A - unidirectional scanning, B - bidirectional scanning, C - re-scanning based on bidirectional scanning with 90° rotation of the scanning direction, D -

island scanning, E - shifting the position of the scan vectors between the layers based on island strategy) are employed in AlSi10Mg alloy, with a relative density of 99.0 %, 98.9 %, 99.4 %, 98.2 % and 98.7 % obtained, respectively. As full density has been achieved in unidirectional scanning strategy, insignificant improvement was witnessed. However, the effect on texture is obvious. The texture index (TI, defined by $\mathrm{TI} = \int_{eulerspace} (f(g))^2 dg$, where *f* is the orientation distribution function as a function of the Euler space coordinates *g*. For isotropic materials, TI is equal to unity) for these strategies was revealed to be 1.974, 1.982, 1.266, 1.127 and 1.079, respectively, in consistent with the fact that rotation of scanning direction always eases texture by changing the heat flow.

Re-melting strategies, which refer to double or multiple layer scanning before depositing a new powder layer, show their potential to reduce porosity and surface roughness since it eliminates surface contaminants, removes oxide films, and produces a clean solid-liquid interface at the atomic level, especially when other optimal parameters are unattainable for full density. Although re-melting process tends to be more time- and energy-consuming, it offers an option to cater to the high density requirement. Li *et al.* proposed that re-melting should be carried out at a low laser energy density to reduce the residual stress and tendency to crack [199]. Smaller melt pools are formed because less laser energy is absorbed by the as-solidified bulk compared with powder materials even with the same scanning parameters, producing finer dendrites due to a higher cooling rate. Nevertheless, investigation of re-melting on the un-melted previous layer and layers below is rare due to the complex thermal history. Yasa *et al.* studied multiple re-melting parameters and concluded that their effects on densification depended on careful parameter optimization.

They reported that re-melting could remedy the porosity defects during SLM process [200]. It can also be applied to only the last layer or the outer skin of the part if the aim is to reduce the roughness or to enhance the surface properties. The research on scanning strategies in SLM nanocomposites is limited. AlMangour *et al.* compared four scanning strategies with TiC/316L stainless steel nanocomposite, as illustrated in Fig. 25. The relative density of samples with these four strategies is 92.48 %, 96.04 %, 86.91 % and 96.40 %, respectively [114]. They showed that higher density is attainable after re-melting comparing strategy I and II, while first scanning strategy needs careful selection as strategy III with re-melting processing show lower relative density than strategy I. The re-melting strategy also shows their effects on texture determination. Same directional re-melting aggravates texture while rotation of scanning direction reduces it. Strategy II and III in Fig. 25 incresase magnitudes of texture and resultant anisotropy of properties due to repeated heat flow direction while strategy I and IV ensures texture coefficient approaching unity and isotropic properties. Therefore, to achieve full density components with isotropy, re-melting with rotation of scanning direction is recommended. Re-melting in MMNCs comes with the concern of distribution of nanoparticles. The mass transfer due to the intense vortex flow causes chemical inhomogeneity and different volume contents at different sides of parts [114]. However, few literatures are available due to the complexity of the fluid flow and solidification characteristics.

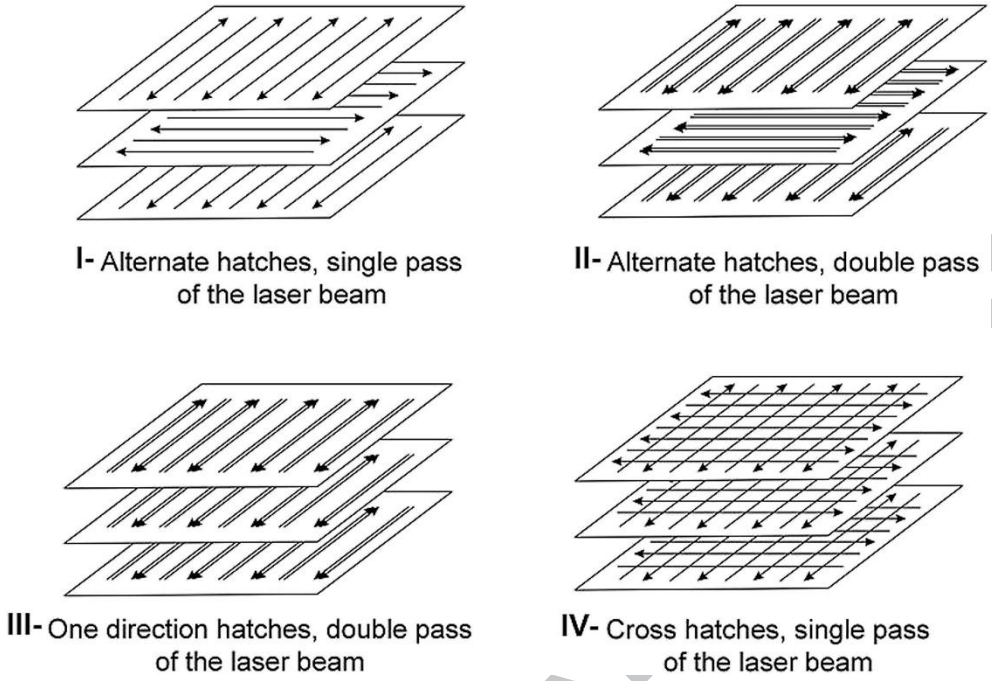

Fig. 25. An overview of the four scanning methodologies: (I) Alternate hatches, single pass of the laser beam, (II) Alternate hatches, double pass of the laser beam, (III) One direction hatches, double pass of the laser beam, (IV) Cross hatches, single pass of the laser beam. (Reproduced from [114], Copyright (2017), with permission from Elsevier).

As to building orientations, vertical, inclined and horizontal building directions (Fig. 26) are popular options for parts with high length-to-height ratio. Rashid *et al.* coined a novel term energy per layer (E_l) to predict the relative density, trying to quantify the relationship between relative density and building orientation [201]. E_l is given by the following equation:

$$E_l = E \times t \times A_p \tag{9}$$

where E is laser energy density, t is powder layer thickness and A_p is printing area per layer. It was found that E_l in the range of 504-895 J yielded AlSi12 SLM-printed samples with over 99.8 % relatively density. The anisotropy caused by building orientation is also

investigated. For example, the fatigue resistance is higher in horizontal direction than in inclined and vertical direction [202]. Tolosa *et al.* compared mechanical tests of 316L stainless steel parts with SLM in all the possible build orientations, not only in the three main directions [203]. For different materials, detailed comparison needs investigation. However, the effects of building orientations have not been addressed yet in MMNCs for SLM.

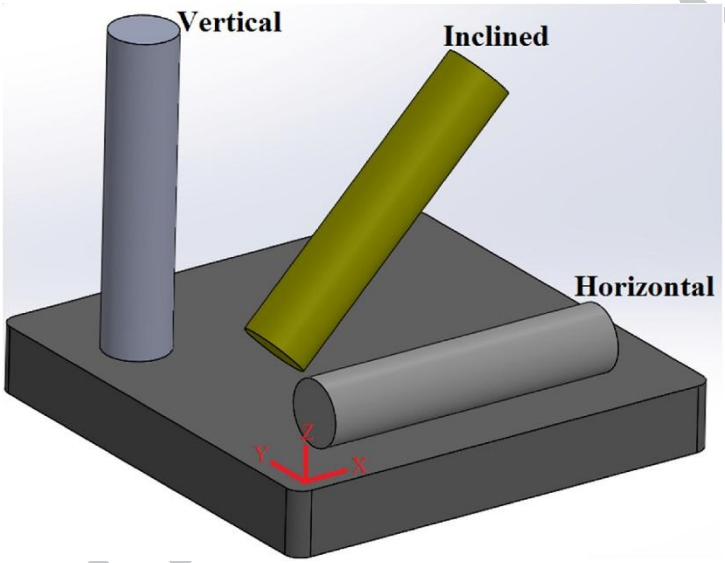

Fig. 26. Schematic representation of three different building orientations: vertical, inclined and horizontal (Reproduced from [201], Copyright (2018), with permission from Elsevier).

3. Influence of nanoparticles on mechanical properties of MMNCs

3.1 Strength

Strength of MMNCs shows significant increase compared with matrix alloys counterparts fabricated with SLM, as shown in Table 4. It is known that strength depends on the relative density of parts [204].The same is true for MMNCs with same reinforced particles. Wen *et al.* produced TiB_2/S136 steel nanocomposites of different reinforcement

contents ranging from 0.5 wt.% to 2.5 wt.% and revealed that even at higher reinforcement content (2.5 wt.%), insufficient relative density leads to inferior strength [205]. However, it is not the case between metallic alloys and nanocomposites because nanoparticles result in lower density but reinforcement in strength. Therefore, a thorough understanding of the reinforcing mechanisms highlighting nanoparticles is necessary.

Table 4 Comparison of ultimate tensile strength (UTS) between MMNCs and matrix alloys fabricated with SLM.

Matrix	Reinforcement	Average particles size (nm)	Contents	UTS (MPa)	Ref.
AlSi10Mg	-	-	-	400	[138]
AlSi10Mg	TiC	50	3 wt.%	486	[138]
AlSi10Mg	TiB_2	~ 100	11.6 wt.%	~ 530 ± 16	[78]
Fe	-	-	-	357 ± 22	[110]
Fe	SiC	700	2.2 wt.%	764 ± 15	[110]
Fe	SiC	78	2.2 wt.%	753 ± 49	[206]
CP-Ti	-	-	-	757 ± 12.5 555 ± 3 (yield strength)	[92]
CP-Ti	TiB		8.35 vol.%	1103 ± 20 (yield strength)	[134]

3.1.1 Strengthening mechanism

An extensive research through available literatures has revealed the possible mechanisms of the increment in strength related to the introduction of the nanoparticles, i.e. Orowan strengthening, grain size strengthening, load-bearing strengthening and enhanced dislocation density strengthening mechanism [207-210].

3.1.1.1 Orowan strengthening

The dislocations suffer bowing, reconnecting and leaving a dislocation loop around the nanoparticles when they move through the small hard particles. This resistance against the motion of dislocations results in considerate strength increments and accounts for a primary mechanism in particle-reinforced MMNCs, known as Orowan strengthening mechanism. The general form to describe Orowan strengthening takes the following Eq. (10-13) [211, 212]:

$$\sigma_{Orowan} = M \frac{0.4 G_m b}{\pi(1-\nu)^{1/2}} \frac{\ln(\bar{d}/b)}{\lambda} \quad (10)$$

$$\bar{d} = \sqrt{\frac{2}{3}} d \quad (11)$$

$$\lambda = \bar{d}\left(\sqrt{\frac{\pi}{4f}} - 1\right) \quad (12)$$

$$G_m = \frac{E}{2(1+\nu)} \quad (13)$$

where M is mean orientation factor, G_m is the shear modulus of matrix, b is the magnitude of Burger's vector, ν is Poisson's ratio, E is the elastic modulus of the matrix, λ is the interparticle spacing, d is the reinforcement particle diameter and f is the volume fraction of reinforcement particles.

This mechanism is negligible in the MMCs reinforced with microscale particles and is activated only when particle size is below 1 μm as both the size of particles and the spacing between them should be comparable to the dimension of dislocation [213]. For example, the calculated Orowan strength increment of 1 vol.% Si_3N_4 (15 nm)/Al composites and 15 vol.% SiC (3.5 μm)/Al is 148.31MPa and 3.36 MPa, respectively [214]. The latter increment is too insignificant to count. Although the contribution of Orowan strengthening

mechanism can be estimated with Eq. (10-13), the models assume that particles distribute randomly and separately in the matrix while micrometric agglomerated particulates is normal in reality. This mechanism only acts on "effective" particulates (below 1 μm in size), and the micrometric agglomeration in between the grain boundary should be excluded in the calculation. In the meanwhile, the diameter of nanoparticles is larger than the original particle size in nanoparticle rich area. However, these are impossible to quantify in experiments. It is certain that the simplification in numerical estimation makes the results higher than experimental data. It should be noted that the improvement in strength caused by Orowan mechanism diminishes as nanoparticles saturate between grain boundaries as the volume fraction of the nanoparticle increases.

3.1.1.2 Grain size strengthening

The introduction of nanoparticles results in a grain refinement of the metal matrix due to constrain of the grain growth by pinning at the grain boundary or introducing nucleation sites [107, 108, 118, 205]. Hall-Petch effect is thus taken into consideration as the strength of materials (σ_{GR}) depends on the grain size of matrix, following the empirical relationship [210, 211],

$$\sigma_{GR} = \sigma_0 + \frac{k_y}{\sqrt{d}} \quad (14)$$

where σ_0 is the yield strength of a single crystal irrespective of any strengthening mechanisms except the solid solution effect, d the average matrix grain size and k_y is a constant depending on the materials.

This contribution in MMNCs depends on the grain size of the matrix which is affected by the size and volume fraction of nanoparticles. Since there is a limit in refinement, there

is a resultant strengthening limit due to Hall-Petch effect. Moreover, higher volume fraction leads to aggregation of nanoparticles and degradation of refinement. AlMangour *et al.* demonstrated that grain size decreases with the decrease in particle size in TiB_2/316L stainless steel system [108] and the increase in the volume fraction in TiC/316L stainless system [131]. In their research, the refinement threshold of volume of nanoparticles is 10 vol.% for both reinforced particles. Wen *et al.* confirmed the refinement effect of nanoparticles while they reported that 0.5 wt.% TiB_2 offers the finest structure in S136 steel matrix [205].

3.1.1.3 Load-bearing strengthening

There emerges a strong bonding at atomic level between dispersed nanoparticles and the matrix due to the nanoscale connection and sound synthesizing methods. Strong coherent bonding facilitates the load transfer at the interface and increases the strength of the materials. The load-bearing contribution of the reinforcement can be estimated with [211]:

$$\Delta\sigma_{Load} = v_p\sigma_m\left[\frac{(l+t)A}{4l}\right] \quad (15)$$

where v_p is the volume fraction of the particles, σ_m is the yield strength of the matrix, l is the size of the particulate parallel to the load direction, t is the thickness of the particulate, and $A=l/t$ is the particulate aspect ratio. Therefore, the strength increment can be expressed as follows:

$$\Delta\sigma_{Load} = \frac{A+1}{4}v_p\sigma_m \quad (16)$$

From Eq. (16), conclusion can be drawn that load-bearing strengthening mechanism in MMNCs is more pronounced in whisker reinforced MMCs when $A > 1$. For the equiaxed particles (A=1), the strength improvement by the load-bearing mechanism is given as [176]:

$$\Delta\sigma_{Load} = \frac{1}{2} v_p \sigma_m \quad (17)$$

The load transfer between the matrix and particles depends on the interface. As introduced in Section 2.1.3, there are usually three types of interface. The assumption in Eq. (15-17) that the interface is well bonded is too vague, without considering the agglomeration of nanoparticles and the type of the interface. Particles with size over 200 nm will initiate the formation of cavities or pits and result in loss of interphase cohesion [11, 215]. Oxidation films on the surface of particles also degrade the interfacial bonding of reinforcement and matrix phases. As the interfacial types and problems are material-specific, it is a difficult exercise to design an optimized interface that is common and suitable for all systems. However, it is generally acknowledged that *in situ* processing facilitate finer and more thermodynamically stable particles with more uniform size distribution in the metal matrix, in contrast to *ex situ* processing. Many researchers evaluate load-bearing strength due to good interface in *in situ* processing, such as TiB_2/AlSi10Mg [78], Al_3BC/Al [161], TiC/316L [97], Cr_3C_2/Fe [120].

3.1.1.4 Enhanced dislocation density strengthening

This mechanism is based on Taylor relationship that relates the contribution of dislocation to the strength of the materials. The increase in the dislocation density is due to mismatch of CTE and the elastic modulus between the matrix and nanoparticles. The CTE mismatch strengthening ($\Delta\sigma_{CTE}$) can be estimated by [211]:

$$\Delta\sigma_{CTE} = M\beta G_m b\sqrt{\rho_{CTE}} \quad (18)$$

where M is the Taylor factor (in unity order), β is the dislocation strengthening coefficient (a constant in the order of 1.25), G_m is the shear modulus of the matrix, b is the magnitude

of Burger's vector, and ρ_{CTE} is the density of dislocations generated from the CTE difference, which can be expressed by [211]:

$$\rho_{CTE} = \frac{Av_p \Delta\alpha \Delta T}{bd_p(1-v_p)} \quad (19)$$

where $\Delta\alpha$ is the CTE difference between the matrix and the reinforcement particles, ΔT is the difference between the processing and test temperature, and A is a geometric constant which varies between 10 and 12 depending on the geometry of the particles. For equiaxed particles, the A constant is assumed to be 12.

In SLM, the contribution of CTE mismatch is pronounced because CTE difference between the matrix and particles increases with the temperature, which results in an increase in dislocation density near the interface. This is consistent with Eq. (19) that ρ_{CTE} value increases with the process temperature. However, for those processes in lower temperature, this mechanism could be less important and is even negligible in room temperature.

Elastic modulus mismatch strengthening mechanism describes similar mechanism and makes contributions only when suitable post processing is applied to the MMNCs, creating dislocations around the particles to accommodate the modulus difference between the matrix and reinforcement. The governing equations are similar as follows [211]:

$$\Delta\sigma_{Modulus} = \sqrt{3}\alpha G_m b\sqrt{\rho_{Modulus}} \quad (20)$$

$$\rho_{Modulus} = \frac{6v_p}{bd_p}\varepsilon \quad (21)$$

where α is the material dependent coefficient, $\rho_{Modulus}$ is the density of dislocations generated from the modulus difference and ε is the uniform deformation.

3.1.2 Prediction models of strength increment

Prediction models of strength improvement include three superposition approaches: arithmetic summation, quadratic summation and compounding models [210].

The arithmetic summation method simply adds the contribution of individual strengthening mechanism in the linear fashion.

$$\Delta\sigma = \Delta\sigma_{Orowan} + \Delta\sigma_{GR} + \Delta\sigma_{Load} + \Delta\sigma_{CTE} + \Delta\sigma_{Modulus} \quad (22)$$

Li *et al.* adopted the method when trying to explain the strength increment caused by the TiB_2 and silicon nanoparticles in AlSi10Mg alloys with SLM [78]. However, this method is generally not applicable in most cases since it neglects the effects of different mechanisms on each other and assumes that they can independently contribute to the final strength of the composites.

Quadratic summation method by Clyne *et al.* acknowledged the interaction between the individual strengthening mechanisms and employed the sum of the squares of the individual strengthening contributions [216].

$$\Delta\sigma = \sqrt{(\Delta\sigma_{Orowan})^2 + (\Delta\sigma_{GR})^2 + (\Delta\sigma_{Load})^2 + (\Delta\sigma_{CTE})^2 + (\Delta\sigma_{Modulus})^2} \quad (23)$$

This method was initially proposed to predict the strength increment of micro-reinforced MMCs, and was later modified to apply to MMNCs by Sanaty *et al.* [211]. The combination of arithmetic summation and quadratic summation is also applied in predicting the strength increment of Al_2O_3/Mg nanocomposites [208].

A third popular model is the compounding method which assumes all the strengthening mechanisms as load-bearing strengthening mechanism and estimates them by using a series of improvement factors. The influences can be manipulated as follows [210]:

$$\sigma = \sigma_m \times \sigma_f \tag{24}$$

$$\Delta\sigma = \sigma_m \times (\sigma_f - 1) \tag{25}$$

$$\Delta\sigma_f = \left(1 + \frac{\Delta\sigma_{Orowan}}{\sigma_m}\right)\left(1 + \frac{\Delta\sigma_{GR}}{\sigma_m}\right)\left(1 + \frac{\Delta\sigma_{Load}}{\sigma_m}\right)\left(1 + \frac{\Delta\sigma_{CTE}}{\sigma_m}\right)\left(1 + \frac{\Delta\sigma_{Modulus}}{\sigma_m}\right) \tag{26}$$

Zhang and Chen employed this concept to establish their prediction model although they only take into consideration of three mechanisms, the load-bearing mechanism, the CTE mismatch, and the Orowan strengthening mechanism [217, 218]. The model can be expressed as follows [211, 217]:

$$\Delta\sigma_{yc} = \Delta\sigma_{ym}(1 + f_{Load})(1 + f_{dislocation})(1 + f_{Orowan}) \tag{27}$$

$$f_l = 0.5v_p \tag{28}$$

$$f_{dislocation} = kG_m b\sqrt{\rho}/\sigma_{ym} \tag{29}$$

$$f_{Orowan} = \frac{0.13G_m b}{d_p\sigma_{ym}\left[\left(\frac{1}{2v_p}\right)^{\frac{1}{3}} - 1\right]}\ln\frac{d_p}{2b} \tag{30}$$

or

$$\Delta\sigma_{yc} = \left(1 + 0.5v_p\right)\left(\sigma_{ym} + A + B + \frac{AB}{\sigma_{ym}}\right) \tag{31}$$

$$A = 1.25G_m b\sqrt{\frac{12(T_{process} - T_{test})(\sigma_m - \sigma_p)v_p}{bd_p(1 - v_p)}} \tag{32}$$

$$\mathrm{B} = \frac{0.13G_m b}{d_p\left[\left(\frac{1}{2v_p}\right)^{\frac{1}{3}} - 1\right]}\ln\frac{d_p}{2b} \tag{33}$$

where σ_{yc} is the yield strength of the composite, and σ_{ym} is the yield strength of the matrix.

Although the model shows better agreement with the experimental data than Ramakrishnan's model which was only applicable for MMCs containing microsized particles [209], refinement of grains was neglected which was proved to play a vital role in the strengthening of nanocomposites.

No consensus has been established as to which model represents reality up to now, although in some cases, the calculated data show similar trends or estimated values with the experimental data. It should be noted that calculated values of strength are always higher than experimental values (Fig. 27) [11]. As mentioned in each individual mechanism description, all equations are based on perfect distribution of particles and well bonded interface. However, there are many practical factors that are different from the assumptions of the models. Agglomeration of particles (especially in nanometer sizes), contaminations and grain growth because of high temperature may influence the experimental procedure and lead to a discrepancy between the theoretical and experimental results.

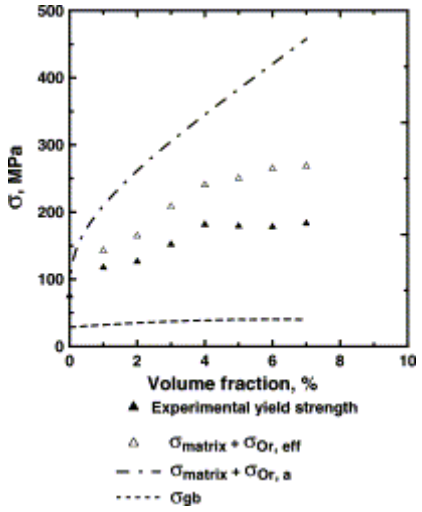

Fig. 27. Comparison of yield strength for Al_2O_3/Al nanocomposites between calculated and experimental results (Reproduced from [11], Copyright (2004), with permission from Elsevier).

3.1.3 Strength dependence on the parameters

Imperfections and complex influences make it difficult to estimate and distinguish the contribution of each mechanism. Thus, some influencing factors are discussed with the prediction models. Fig. 28 plots the dependence of strengthening mechanism contribution over volume fraction for reinforcement particles with two different sizes, the nanometer (30 nm) and micrometer scale (1 μm), with modified Clyne *et al.* model [211]. MMNCs witness an increase in strength increment with the increase of volume fraction of particles. For MMNCs with nanometer reinforcement, all the strengthening contributions expect load-bearing strengthening are more pronounced than those with the micrometer particle reinforcement. Loading bearing effect is negligible for both particle size. This is contradictory to the argument that the interfacial bonding effects between matrix and particles enhance strength of the composites [78, 161]. Although the effect of interface is

highly valued, their effect in numerical estimation shows insignificance compared with other mechanisms while taking no consideration of defects. Further experiment and calculation are thus necessary to validate the principle.

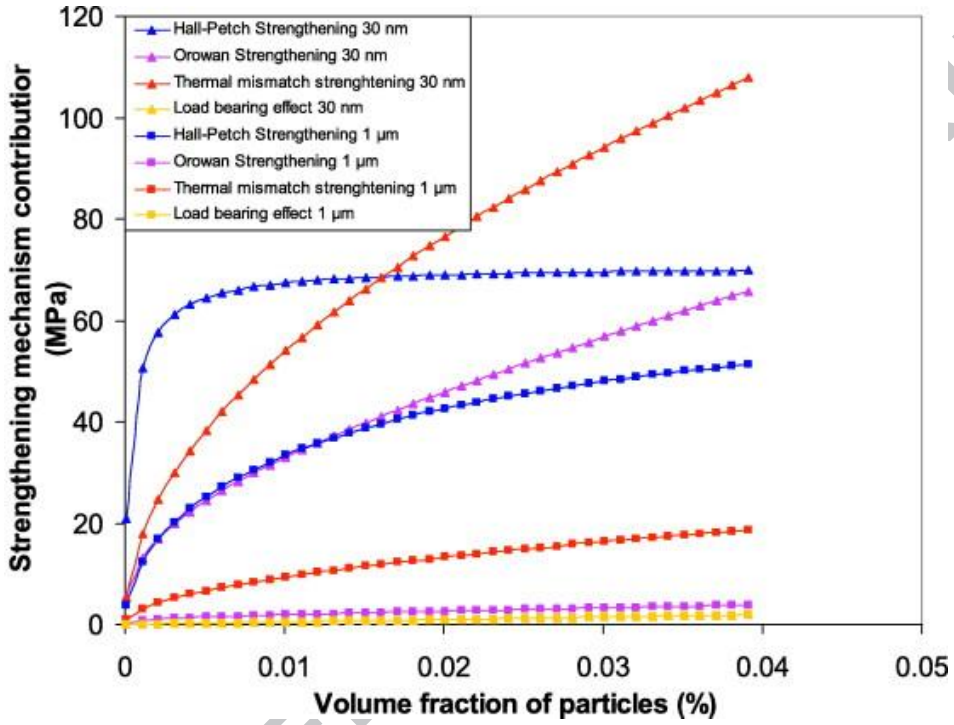

Fig. 28 Strengthening mechanism contributions versus volume fraction with the particle sizes of 10 nm and 1 μm in Y_2O_3/Mg composite (Reproduced from [211], Copyright (2012), with permission from Elsevier).

Fig. 29 shows the strength prediction of nanocomposites according to Zhang and Chen's model, from which the conclusion could be drawn that the strength of the nanocomposites relies strongly on the nanoparticle size and volume fraction [217]. Both decrease of particle size and increase of the volume fraction result in significant strength improvement of the composites. However, decreasing the particle size leads to difficulty in dispersing them

uniformly. Little experimental data is available for nanoparticles less than 50 nm in size. The ease of processing is a key bottleneck for MMNCs with further smaller reinforcement.

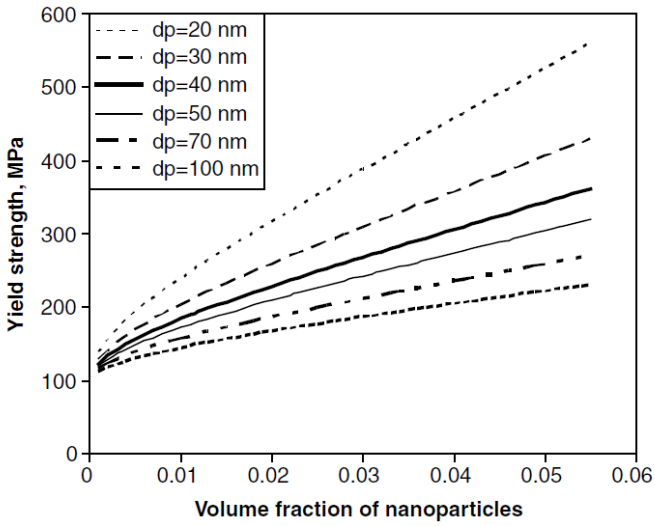

Fig. 29. Yield strength versus volume faction of Al_2O_3/Mg nanocomposites with different particle sizes (Reproduced from [217], Copyright (2006), with permission from Elsevier).

3.2 Ductility

Strengthening is usually achieved at the expense of ductility. MMCs with micrometer reinforcement encounter a tradeoff between tensile strength and ductility as the large size of the particles and aggregations of them cause severe stress concentration. The stress concentration intensifies with the particles contents [219]. Nanocomposites with smaller reinforcement and better interfacial bonding may overcome this issue.

Some research revealed a possible simultaneous enhancement in strength and ductility. CNT/Mg [220, 221] and Y_2O_3/Mg [76] nanocomposites find their peak in ductility with the increase of the reinforcement contents. Any higher contents of nano-reinforcement impair the ductility of the MMNCs. The content for peak ductility is relative low, i.e. 1.3 wt.% for CNT and 0.22 vol.% for Y_2O_3, respectively. The ductility improvement in the above

research is also related to the hot extrusion processing. In other cases, the ductility of Al_2O_3/Mg nanocomposites shows a continuous decrease with the addition of the ceramics [208]. The effects of nanoparticles on ductility property of MMNCs seem to vary with the fabrication methods. The key factors lie in the grain boundaries and the distribution of nanoparticles [222]. The nanoparticles promote refinement of the matrix in many liquid state methods. Despite this positive effect in microstructure, decreasing ductility is still common in MMNCs, emphasizing the importance of the distribution of nanoparticles.

The mechanisms for ductility improvement in simple metals or alloys are well summarized in literature [223]. However, the mechanisms for the ductility improvement caused by nanoparticles have not been well established. Possible explanations are related to the conditions of grain boundaries and particle dispersion. Imperfections in grain boundary bonding and decohesion result in the fracture. The interface between matrix and nanoparticles replaces the grain boundaries between the matrix grains and leaves the MMNCs less ductile. The increasing content of the nanoparticles increases the interface fraction. Particle dispersion is related to the ease of dislocation motion. Dislocation density is high due to the CTE mismatch and elastic modulus mismatch during deformation. Liu *et al.* compared the ductility of Mo alloys with intragranular and intergranular La_2O_3 particles [224]. The former distribution pattern of nanoparticles diminishes the grain boundary cracking caused by larger intergranular particles which helps to nucleate and pins down the dislocations. The effect of interior nanoparticles resembles that in heat-treated alloys with precipitates in nanometer scale. However, this particle distribution is difficult to achieve, especially with exogenous reinforcement particles. As to the intergranular particles, they

tend to fracture and decohere from the matrix except some particles in smaller size with no agglomeration. The negative effects decrease with the size of nanoparticle.

The research of ductility in MMNCs by SLM is limited to a few literatures. A comparable or higher ductility is expectable with this method. The SLM fabricated TiB_2/AlSi10Mg MMNCs exhibited a high ductility of ~ 15.5% with TiB_2 nanoparticles distributing along the grain boundaries and nano-silicon precipitates inside Al grains. The excellent ductility can be attributed to both the sound bonding between TiB_2 and Al grains and the interior silicon nanoparticles [78]. Almangour *et al.* reported that in compressive mode, the ductility of TiB_2/316L stainless steel MMNCs remain almost the same with 316L steel even when TiB_2 reaches up to 15 vol.% [108]. Although the compressive mode facilitates the closure of pores and thus good ductility, the tangle and accumulate of slip dislocation cannot be ignored.

The sensitive optimization of ductility depends on SLM parameters [138]. In fact, both relative density of the parts and the distribution of the particles are responsible for the ductility. Processing parameters that result in poor relative density or insufficient distribution correspond to degradation of ductility.

3.3 Hardness

In SLM, the highly localized heat input leads to fast melting and solidification, resulting in unique microstructures. Moreover, nanoparticles constrain the grain growth and thus facilitate the refinement of the structure, which is evidenced by Li *et al.* [78] and AlMangour *et al.* [108]. The concurrence of grain refinement and the existence of hard ceramic phases facilitate high microhardness of MMNCs. Table 5 lists the microhardness

of various nanocomposites produced using SLM compared with matrix alloys without reinforcement materials.

Table 5 Comparison of microhardness between MMNCs and matrix alloys fabricated with SLM.

Matrix	Reinforcement	Contents	Microhardness	Ref.
AlSi10Mg	-	-	145 $HV_{0.1}$	[138]
AlSi10Mg	TiC	3 wt.%	188.3 $HV_{0.1}$	[138]
AlSi10Mg	TiB_2	11.6 wt.%	191 ± 4 $HV_{0.3}$	[78]
AlSi10Mg	Fe_2O_3	15 wt.%	165 $HV_{0.1}$	[117]
AlMg1SiCu	Fe_2O_3	15 wt.%	110 $HV_{0.1}$	[225]
Al	Fe_2O_3	15 wt.%	85 $HV_{0.1}$	[117]
CP-Ti	-	-	261 $HV_{0.05}$	[92]
CP-Ti	TiB	8.35 vol.%	402 ± 7 $HV_{0.05}$	[134]
CP-Ti	TiC	12.5 wt.%	577 $HV_{0.2}$	[102]
316L	-	-	215 $HV_{0.1}$	[131]
316L	TiC	15 vol.%	~ 403 $HV_{0.2}$	[131]
316L	TiB_2	15 vol.%	~ 611 HV0.1	[108]
316L	TiC	4 wt.%	285.2 $HV_{0.3}$	[226]
H13	-	-	748 $HV_{0.2}$ (top view) 810 $HV_{0.2}$ (side view)	[98]
H13	TiC	15 vol.%	811 $HV_{0.2}$ (top view) 858 $HV_{0.2}$ (side view)	[98]

Microhardness depends on the microstructure of matrix and reinforcement distribution. Alloying elements of aluminum alloys harden the MMNCs matrix with the same reinforcement (Fig. 30). The *in situ* Fe_2O_3/AlSi10Mg MMNCs exhibit higher (micro-) hardness (165 $HV_{0.1}$) than that of both Fe_2O_3/AlMg1SiCu (110 $HV_{0.1}$) and Fe_2O_3/Al composites (85 $HV_{0.1}$). This can be attributed to grain refinement due to the alloying elements which are evident by 300-400 nm in Al/15 wt.% Fe_2O_3, 40-300 nm in AlMg1SiCu/15 wt.%Fe_2O_3, and 40-200 nm in AlSi10Mg/15 wt.%Fe_2O_3 [117]. However,

reinforcement efficiency in pure Al overwhelms that in the alloying matrices. The hardest matrix sees the least increase in hardness.

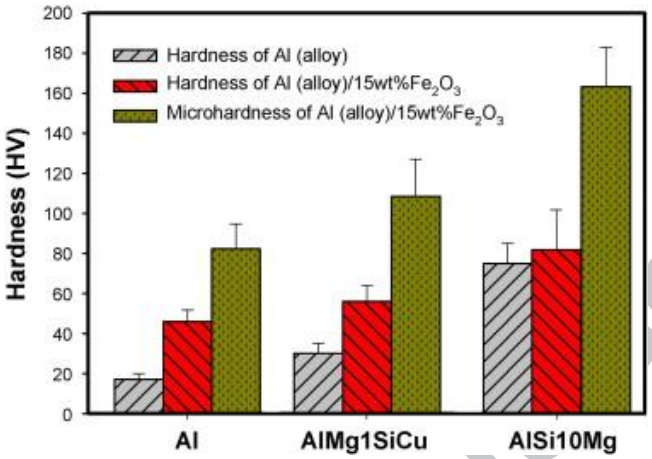

Fig. 30. (Micro)hardness of *in situ* Fe_2O_3/Al-based alloys nanocomposites (Reproduced from [117], Copyright (2012), with permission from Elsevier).

Reinforcement distribution plays a vital role as they refine the matrix and act as a hard second phase. In the foregoing discussion, the microstructure and particle distribution depends on the volume fraction and processing parameters. Generally, microhardness increases with the increasing contents of the hard ceramic reinforcement [108, 227]. It is true in AlMangour *et al.* [108, 131] and Dadbakhsh *et al.* [227] research as microhardness increases significantly and monotonously with TiC or TiB_2 reinforcement in 316L stainless steel matrix and Fe_2O_3 in aluminum matrix. However, in other case, there is a critical fraction beyond which the microhardness degrades. For example, Gu *et al.* reported the increasing trend below 12.5 wt.% and the decreasing trend thereafter in TiC/Ti nanocomposites (Fig. 31). In TiC/Ti system, the structure and distribution of TiC particles are sensitive to the volume fraction because higher contents deprive the nanostructure [102].

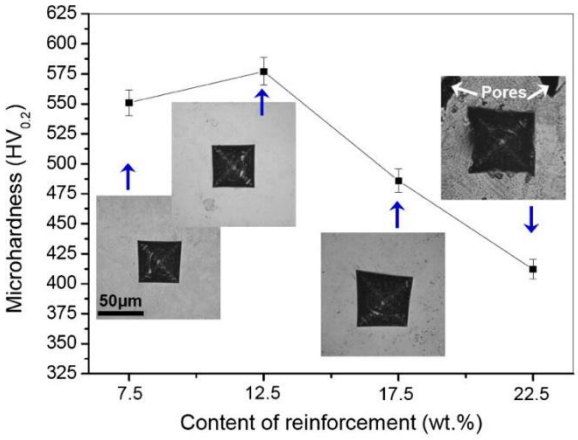

Fig. 31. Microhardness of SLM processed TiC/Ti nanocomposite parts at different reinforcement content and corresponding indentation morphology (Reproduced from [102], Copyright (2016), with permission from Elsevier).

MMNCs hardness is sensitive to the SLM parameters because nanoparticle dispersion depends on them. Fig. 32 illustrates the microhardness of SLM-processed TiC/AlSi10Mg nanocomposite parts varying with laser energy density. Microhardness shows a trend of increasing first and decreasing thereafter with optimal processing parameters, inconsistent with the randomly distribution of reinforcement and ring-like structures [138]. Smaller starting particle size also shows superior performance (Fig. 33), inconsistent with the micro-reinforced MMCs [131]. Zhao *et al.* compared the microhardness of 316L stainless steel based MMNCs reinforced with TiC of 40 nm and 800 nm and higher hardness is found in the former one [226].

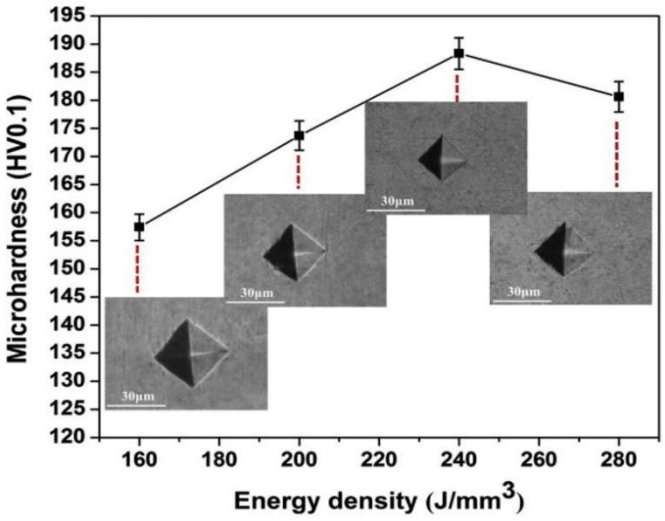

Fig. 32. The dependence of microhardness of SLM-processed TiC/AlSi10Mg nanocomposite parts on laser energy density (Reproduced from [138], Copyright (2015), with permission from Elsevier).

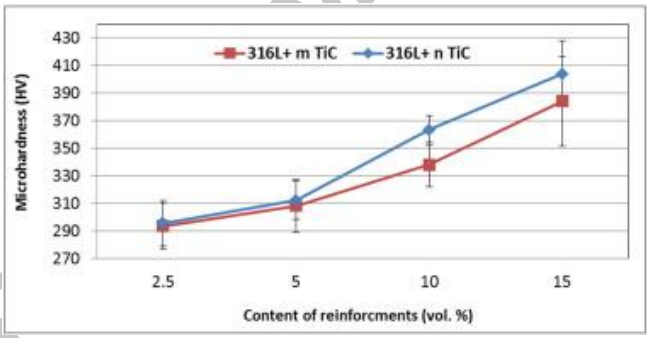

Fig. 33. The influence of particle sizes and volume fraction of nanoparticles on the microhardness of SLM-processed TiC/316L nanocomposites (Reproduced from [131], Copyright (2016), with permission from Elsevier).

Scanning strategies not only lead to anisotropy of matrix microstructure, but also generating inhomogeneity in particle distribution. AlMangour *et al.* reported the hardness measured from the top and side surfaces of the samples with different scanning strategies shown in Fig. 25. Re-melting strategy leads to grain refinement and higher microhardness

(strategy II, III, IV). However, careful design to achieve isotropy is of concern. Significant differences in the microhardness of the top and side were observed in samples produced with scanning method II and III, which resulted in anisotropic property (Fig. 34) [114]. The single-pass alternate hatch scanning strategies (I and IV) yield a lower degree of anisotropy.

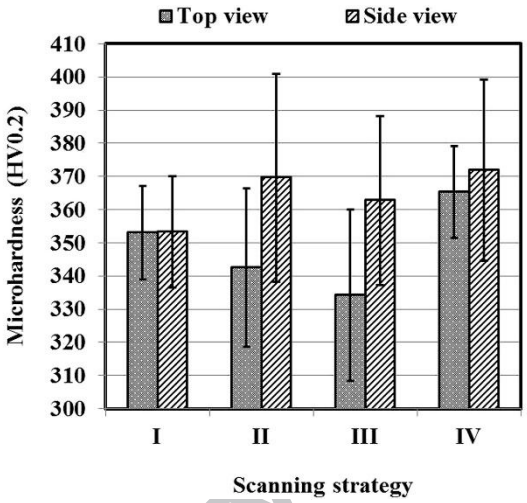

Fig. 34. The microhardness of SLM fabricated nanocomposites with scanning strategies shown in Fig. 25 (Reproduced from [114], Copyright (2017), with permission from Elsevier).

3.4 Fatigue

Fatigue is a catastrophic failure in structural materials, making the materials' resistance to fracture and fatigue crack propagation of paramount importance. To gain a better understanding of fatigue life, this section will focus on SLM targeted features and the influence of nano or sub-micro particles in MMNCs and discuss the mechanisms.

The fatigue damage process of composite materials during high-cyclic fatigue (HCF) is similar to that in the alloys and consists of three consecutive stages (Fig. 35): (1) Stage I, fatigue crack initiation; (2) Stage II, crack propagation; (3) Stage III, ultimate fracture [228,

229]. The discussion of the fatigue characteristics of MMNCs will be derived according to the stages.

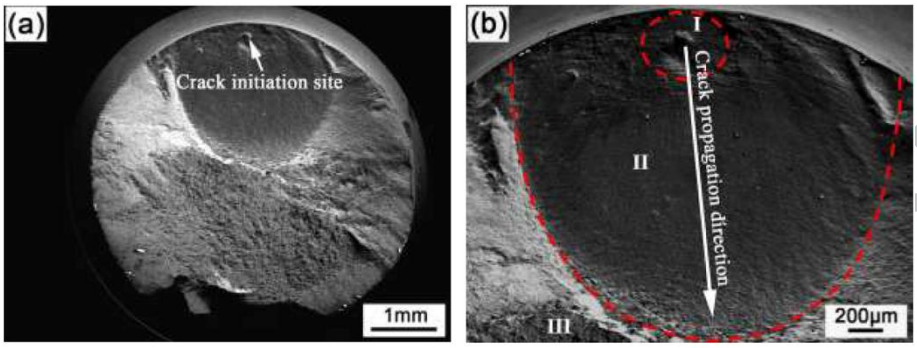

Fig. 35. SEM images showing (a) an overview of fracture surface and (b) three fracture stages (Reproduced from [228], Copyright (2017), with permission from Elsevier).

Generally, pores, inclusions [193], large particles (e.g. intermetallics [230]), grain boundary, slip bands [231] and weak particle/matrix bonding [230] can act as initiation sites in Stage I. Rough surface is also expected to result in degradation in fatigue behavior. These imperfections are strongly dependent on the fabrication methods. For SLM, the inherent drawbacks i.e. process-induced pores, inclusions and insufficient surface quality must be minimized for better fatigue performance. The size, fraction and location of pores have proven to be significantly important to fatigue life. Large size, high porosity and defects adjacent to the surface incur extreme low fatigue life [232-234]. Other causes include oxide films and unmelted powder particles [193, 235]. It is noted that machining improves the fatigue performance, although the effect of surface roughness is difficult to quantify because of concurrence of the residual stresses and porosity [236]. The MMNCs possess narrow processing window and are more prone to imperfections. From this prospective view, the as-built MMNCs by SLM are easier to initiate cracks.

On the other hand, as grain boundaries lead to dislocations piling-up which may cause strain localization and accelerate premature failure, nano or sub-micro particles within grain boundaries would show their effect. The relation of dislocations' distribution and nanoparticles depends on their size and interface with the matrix. For very small particles (less than 500 nm), pronounced dislocation loops generated by Orowan process lead to a homogeneous dislocation distribution and impede crack initiation. Nevertheless, for large particles, they may emit dislocations from edges, resulting in stress concentration during cyclic loading. If by-products such as secondary phases emerge in MMNCs, their aggregations would be an alternative initiation sites. Geng *et al.* revealed that clusters (S (Al_2CuMg) /θ ($CuAl_2$) phases + TiB_2 particles) can act as initiation sites in *in situ* TiB_2/Al-Cu-Mg composites [228]. Tjong *et al.* found Al_3Ti blocks of micrometer scale act as initiation sites during HCF [237]. This is also true in some micrometer scale reinforced MMCs [238]. The ceramic particle fracture and interface de-bonding are dominant to the damage mechanisms. *In situ* MMNCs generally do not undergo gas adsorption or oxidation and thus promote stronger interfacial bonding and improved mechanical properties in the final products [5, 97, 239].While *ex situ* incorporated particles which generally exhibit sharp edges may act as stress concentration risers to cause brittle fracture and become initiation sites during fatigue life [240, 241]. MMNCs are reported to show higher fatigue performance even though SLM fabricated MMNCs are rarely investigated for their fatigue performance.

For Stage II, residual stress and microstructure associated with the SLM process are the main influencing factors. However, the relationship between the nanoparticles and residual stress has not been established [242]. Post-process stress relief and hot isostatic pressing

(HIP) must be employed when fatigue performance is of primary concern as the as-built components show low fatigue life. The crack propagation depends on the microstructure features, i.e. grain boundaries, grain orientations and reinforced particles. Grain boundaries retard crack propagation and the retardation efficiency depends on the inclination angle of the grain boundary to the crack propagation direction. The resistance to crack growth reaches its maximum when the grain boundaries are normal to the crack direction and decreases to almost none until the grain boundaries are parallel to the crack direction. The enriched grain boundaries in MMNCs exert positive effect during HCF. Moreover, nanoparticles around grain boundaries enhance the retarding efficiency on crack propagation in most cases. Well dispersed nanoparticles reduce crack propagation rate (CPR) during HCF. Geng *et al.* revealed particle both at the grain boundaries and within the grain interior, which include almost all particle types [228].

Two types of particles at grain boundaries, i.e. the TiB_2 particle rich region and aggregated TiB_2 nanoparticles, are shown in Fig. 36 [228]. The former type in Fig. 36a results in striations in divergent directions (indicated by arrows) and much more tearing step lines. Around aggregated TiB_2 particles at grain boundaries (Fig. 36b) are located some shear steps and decreasing striation distance (SD, upon which CPR can be approximately evaluated, as it is directly proportional to SD [243, 244]) from 102 nm to 82 nm. Both types of particles retard the CPR.

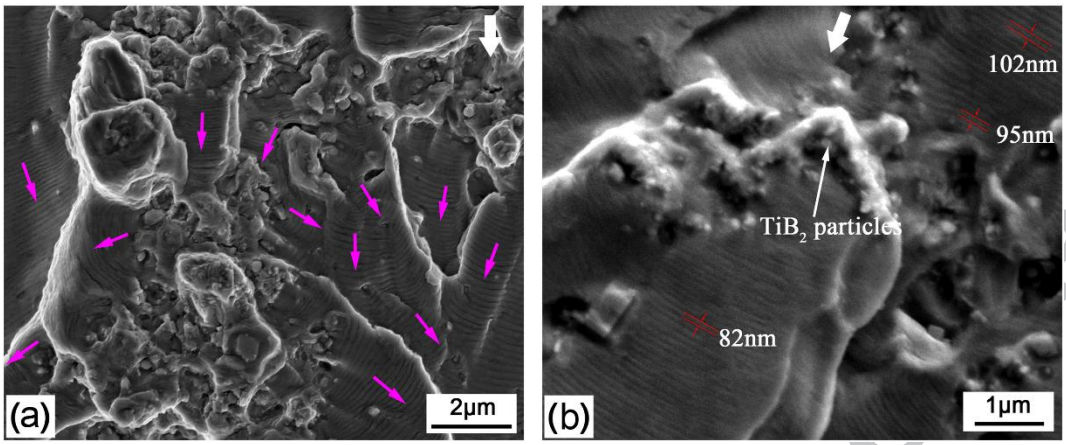

Fig. 36. The typical crack propagation characteristics depending on the particles at grain boundaries: (a) TiB_2 nanoparticle rich region, (b) aggregated TiB_2 nanoparticles. The white arrow indicates the overall crack propagation direction (Reproduced from [228], Copyright (2017), with permission from Elsevier).

Geng *et al.* also revealed the role of dispersed TiB_2 particles within the grain interiors [228]. They can reduce CPR with local curvature deviating from the overall crack front, while the efficiency is dependent on their size. Particles larger than 500 nm initiate microvoid around it (Fig. 37a) whilst those of comparable size with SD (marked by A in Fig. 37b) curve the striation with no microvoid around it. Particles far smaller than SD (indicated by B, C, D in Fig. 37b) slightly decrease SD with few curvature alternations. Several clustered particles shown in Fig. 37c and d (< 500 nm) within grains hinder the crack growth by decreasing SD and producing new crack planes on the shear steps. The foregoing description of particle types and their effects on the HCF can be applied to those with coherent interface with the matrix. However, those particles without coherent or semi-coherent interface bonding would only distribute at the grain boundaries. Their effect still

depends on their distribution and cluster size. Further investigation is in need to reveal the interface effect of different ceramics and matrices.

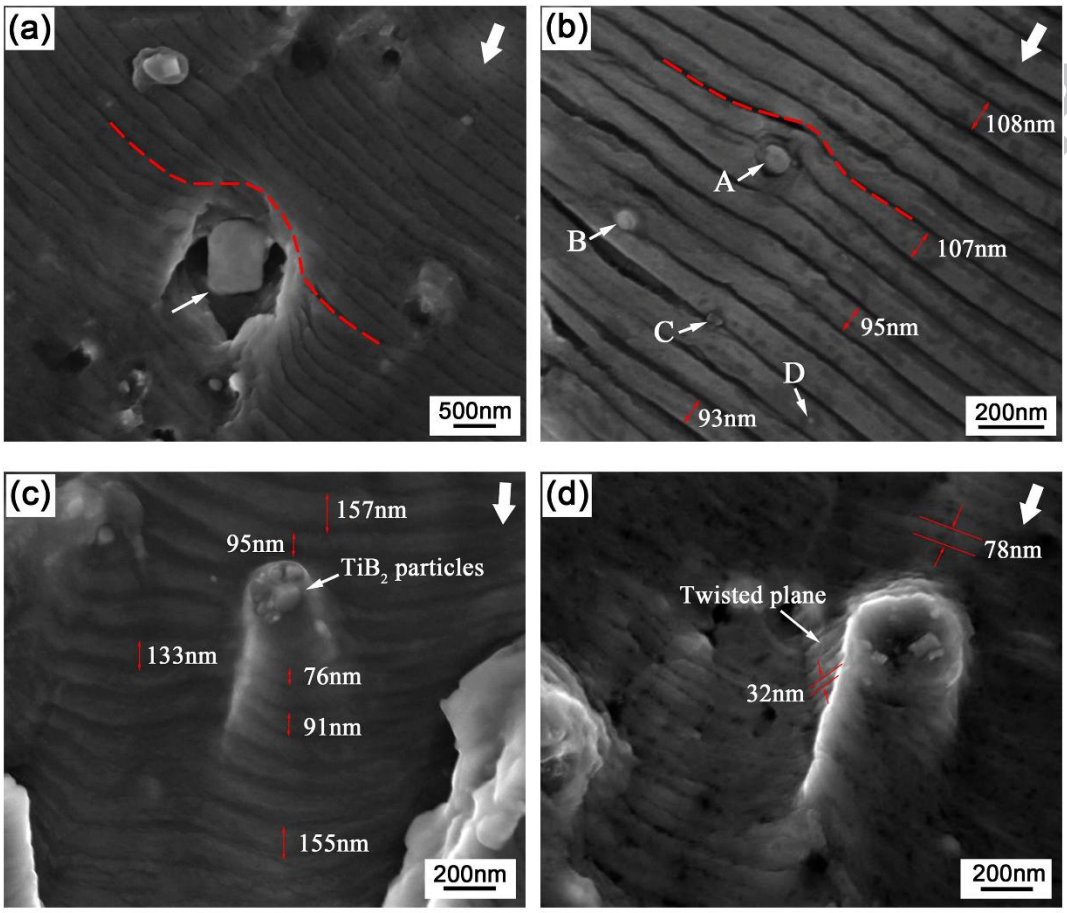

Fig. 37. The interaction between SD and TiB_2 particles within grains: (a) large particles (>500 nm), (b) nanoparticles (comparable or smaller than SD), (c) shear step produced by TiB_2 nanoparticles, (d) twisted plane formed by TiB_2 nanoparticles. The white arrow indicates the overall crack propagation direction (Reproduced from [228], Copyright (2017), with permission from Elsevier).

For Stage III, an acceleration in growth rate of the fatigue crack growth in MMNCs is expected compared with homogeneous alloys [245]. This is true both in MMCs with micro- and nanoscale particles reinforcement.

Overall, the MMNCs with SLM show higher tendency to crack initiation and ultimate fracture while the crack propagation in Stage II is retarded. Further investigation is in demand as more and more MMNCs with SLM are applied as structural components.

4. Defects

A promising future and wide application of the SLM technology hinges on the fabrication of defect free parts. However, many metallurgical defects in SLM processed metallic parts, e.g. balling, porosity, cracking, oxide inclusions and loss of alloying elements, remain unsolved though extensive efforts have been devoted to the solutions. In this section, these defects would be elucidated by highlighting their classification, mechanisms of formation and tendency in MMNCs.

4.1 Balling effect

Balling phenomenon which decreases the surface quality, is a typical defect in SLM. Two types of balling were reported: the ellipsoidal balls with dimension of about 500 μm and the spherical balls with dimension of about 10 μm. The former is attributed to the broken melt tracks, resulting from the worsened wetting ability to the substrate or previous layer. Both severe oxidation of the melt pool or low energy input could result in the worsen wetting characteristics [178]. The oxygen contents of atmosphere below 0.1 % for 316L stainless steel and proper laser power, scanning speed and layer thickness should be controlled, as stated in Section 2.2.1. Stacking of these large balls scratches the blade, hinders the movement of the recoating roller and finally blocks the production process. The second type is formed due to reduction of the liquid surface energy at short length scales by splashing of the molten metal [246]. Both balling effects impede the uniform deposition of

fresh powder on the previous layer and tend to incur further defects, e.g. porosity and crack, which will be addressed in Section 4.2 and 4.3, respectively.

The nanocomposites powders possess different processing windows from the matrix metals due to the change of the physical properties. Gu *et al.* carried out investigation in both CP-Ti and TiC/Ti nanocomposites with the same SLM parameters, i.e. laser power 90 W, hatch spacing and layer thickness 50 μm, scanning speed varying at 100 to 400 mm/s with an interval of 100. Balling effects of TiC/Ti nanocomposites are as severe when the scanning speed is 200 mm/s (Fig. 38b) [136] as those of the matrix alloy counterpart with scanning speed at 400 mm/s (Fig. 39d) [87]. When scanning speed reaches 400 mm/s in MMNCs, severe balling effects with low relative density (91.6 %) degrade the performance of the parts. Balling effects start to occur in SLM fabricated AlSi10Mg components when scanning speed exceeds 500 mm/s or 750 mm/s [183] while in 5 wt.%TiC/AlSi10Mg composite, the threshold drops down to 350 mm/s with other parameters fixed [182]. Similar phenomena are also found between TiC/316L nanocomposites [58] and 316L stainless steel [178, 247].

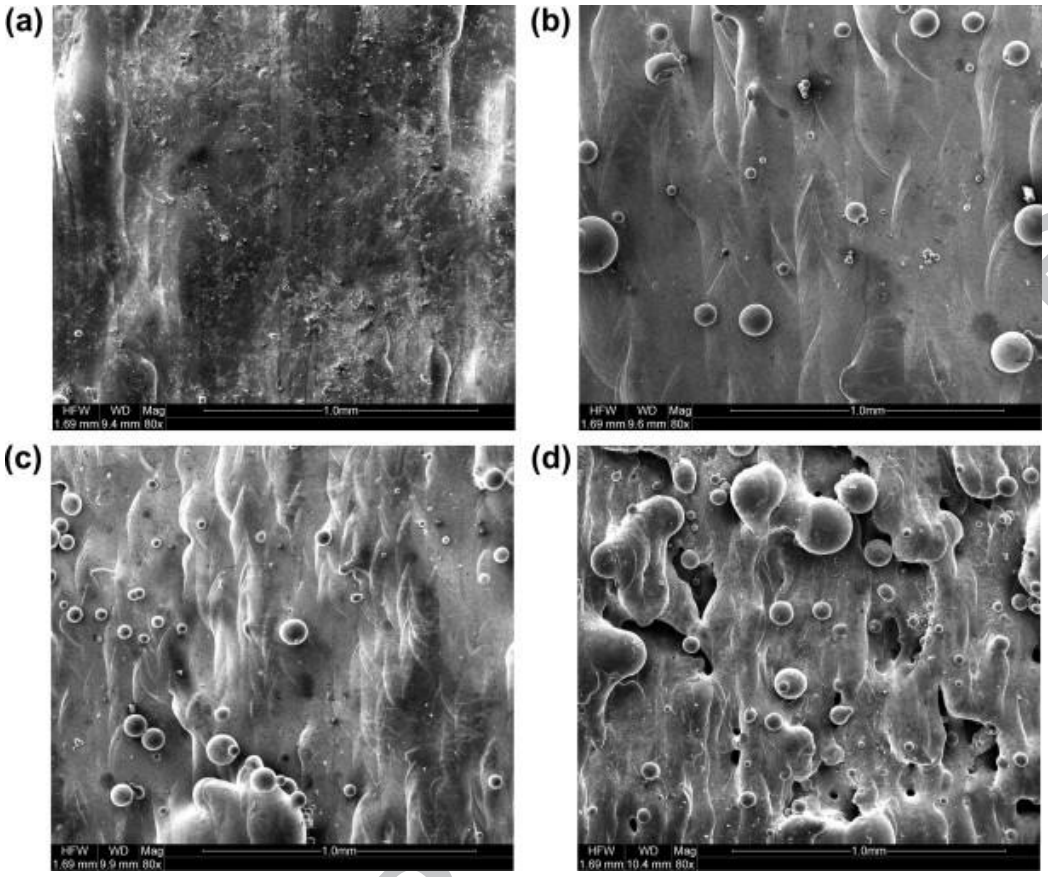

Fig. 38. SEM images of typical microstructure of TiC/Ti nanocomposite parts fabricated by SLM with various scanning speed of: (a) 100 mm/s, (b) 200 mm/s, (c) 300 mm/s, (d) 400 mm/s (Reproduced from [136], Copyright (2011), with permission from Elsevier).

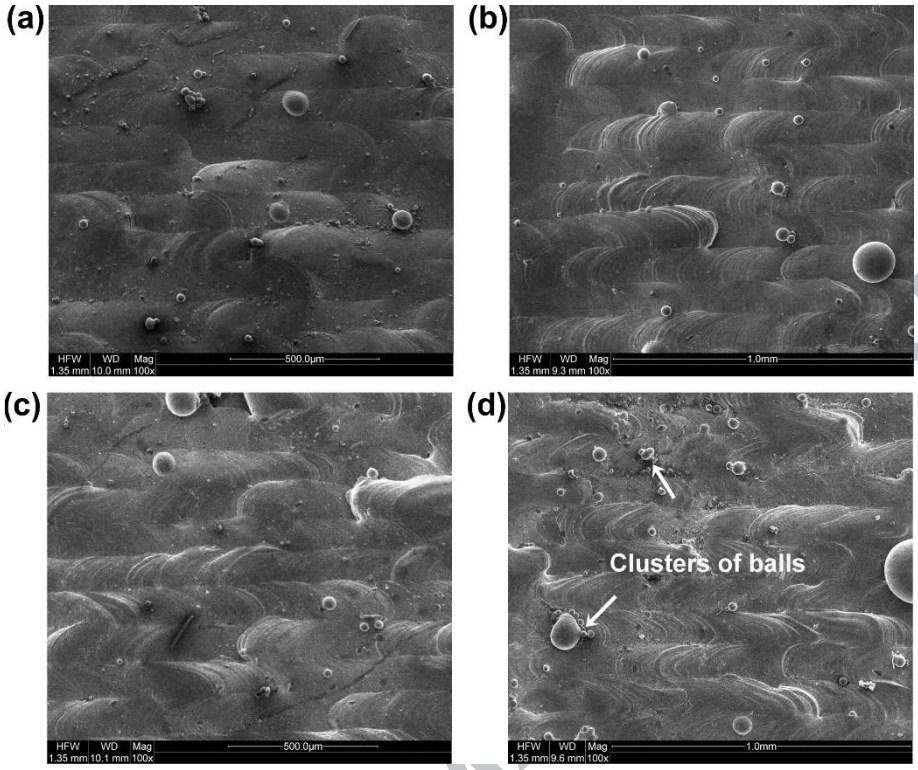

Fig. 39. SEM images of typical microstructure of CP-Ti parts fabricated by SLM with various scanning speed of: (a) 100 mm/s, (b) 200 mm/s, (c) 300 mm/s, (d) 400 mm/s (Reproduced from [87], Copyright (2012), with permission from Elsevier).

As balling effect is dominated by wetting characteristics, processing parameters selection must take physical properties of the materials into consideration. The volume of nanoparticles has a significant effect on the threshold. Gu *et al.* found that in 7.5 wt.%TiC/AlSi10Mg nanocomposites, balling effect occurs with scanning speed reaching 150 mm/s compared with 350 mm/s in 5 wt.%TiC/AlSi10Mg [140]. The balling effect partially depends on the powder preparation methods which determine the quality of the starting powder. Gu *et al.* compared the TiC/Ti nanocomposite powders prepared with ball milling and direct mixing methods and revealed more severe balling phenomenon in the

parts produced with the latter ones [109]. Poor wettability of the direct mixing powder is responsible for the instability of the melt pool.

4.2 Porosity

Porosity is a common feature and demerit of SLM parts. Main formation mechanisms acknowledged include insufficient melting (lack of fusion porosity) and gases entrapped by turbulent flow of liquid metal in the melt pools. The first type forms due to the inadequate overlapping of tracks or shallow penetration of the laser energy into the deposited powders, originating from low laser power, high scanning speed, large hatch spacing and layer thickness. The entrapped gases include shielding gas, vapor, hydrogen and gases entrapped during powder atomization process [248]. The two main mechanisms can be divided by the porosity location, with the former type outside the melt pool while the latter type inside the melt pool. The common feature of the formation of both types of pores can be derived from the instability of fluid flow in the melt pool which is dictated by various forces exerted on the metallic/gaseous interface [249].

Large hatch spacing leads to insufficient overlapping of the tracks and lack of fusion. Low laser power, high scanning speed and large layer thickness result in balling effects which deteriorate the recoating of new layer and may result in unmelting of the powders entrapped in the imperfect positions such as the neighbouring tracks. Imperfect positions also include open pores and cave-like pores formed on the top surface of each scanning track as illustrated in Fig. 40 [179]. The presence of open pores on the surface of the track could be attributed to either a lack of material filling or material splashing out of the melt pool. The cave-like pores are formed when the unstable melt flow moves away from laser scanning direction and then solidifes up in the air before bonding with the solid underneath.

Open pores or cave-like pores are different from the ones in bulk materials, but it is possible that they remain in the building process. The cave-like pores mainly remain as final pores in the parts because of the coverage, while the open pores gain more chance to be filled with melt materials in the subsequent scanning. Qiu *et al.* [249] and Khairallah *et al.* [72] both proved the existence of these pores with their models.

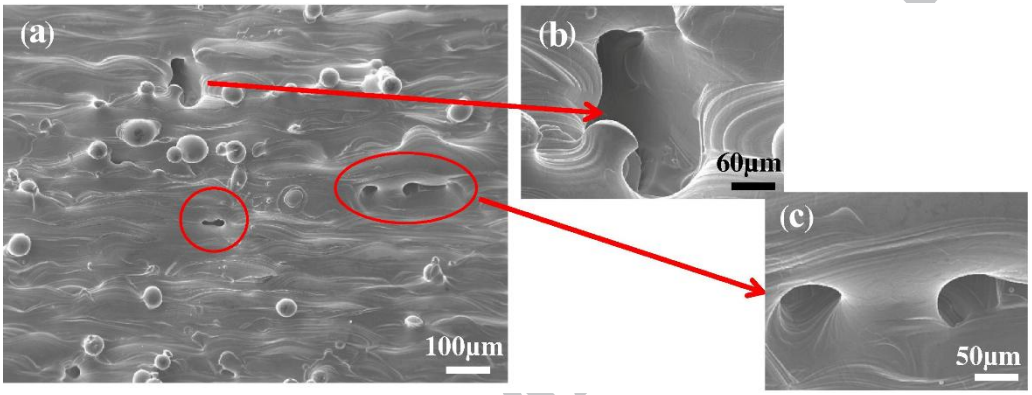

Fig. 40. SEM micrographs showing (a) the top surface characteristics of as-fabricated Ti-6Al-4V samples by SLM with powder layer thickness 60 μm, (b) magnified image of open pores, (c) magnified image of cave-like pores (Reproduced from [179], Copyright (2015), with permission from Elsevier).

As discussed in Setion 4.1, the tendency of balling effect is more severe in nanocomposites. Although a slower scanning speed is employed, balling effects tend to occur at a lower threshold, which means that porosity is more inevitable in nanocomposites. For example, porosity is more severe in AlSi10Mg alloys blended with Fe_2O_3 powder, especially at higher volume content [227].

Khairallah *et al.* simulated the formation of entrapped shielding gas by fluid flow behavior, as shown in Fig. 41 [72]. The authors asserted that a depression region is formed ahead of the melt pool as the Gaussian laser center causes the highest temperature. When

the surface temperature approaches the boiling point, the recoil pressure normal to the surface increases exponentially and drives the liquid away from the center. It digs a hole and forms the depression region (45-76 μs in Fig. 41). After the laser spot moves forward, the temperature begins to decrease exponentially in the absence of recoil force (at 82-92 μs). Consequently, the melt flow velocity vector reverses their direction towards the center of the melt pool starting at 82 μs. The reversal is abrupt and causes the sidewall to collapse within 5 μs. Sheilding gas is thus easy to be trapped due to the fast flow. Escaping failure of these bubbles during the subquent solidification (100-400 μs) results in porosity in the bulks.

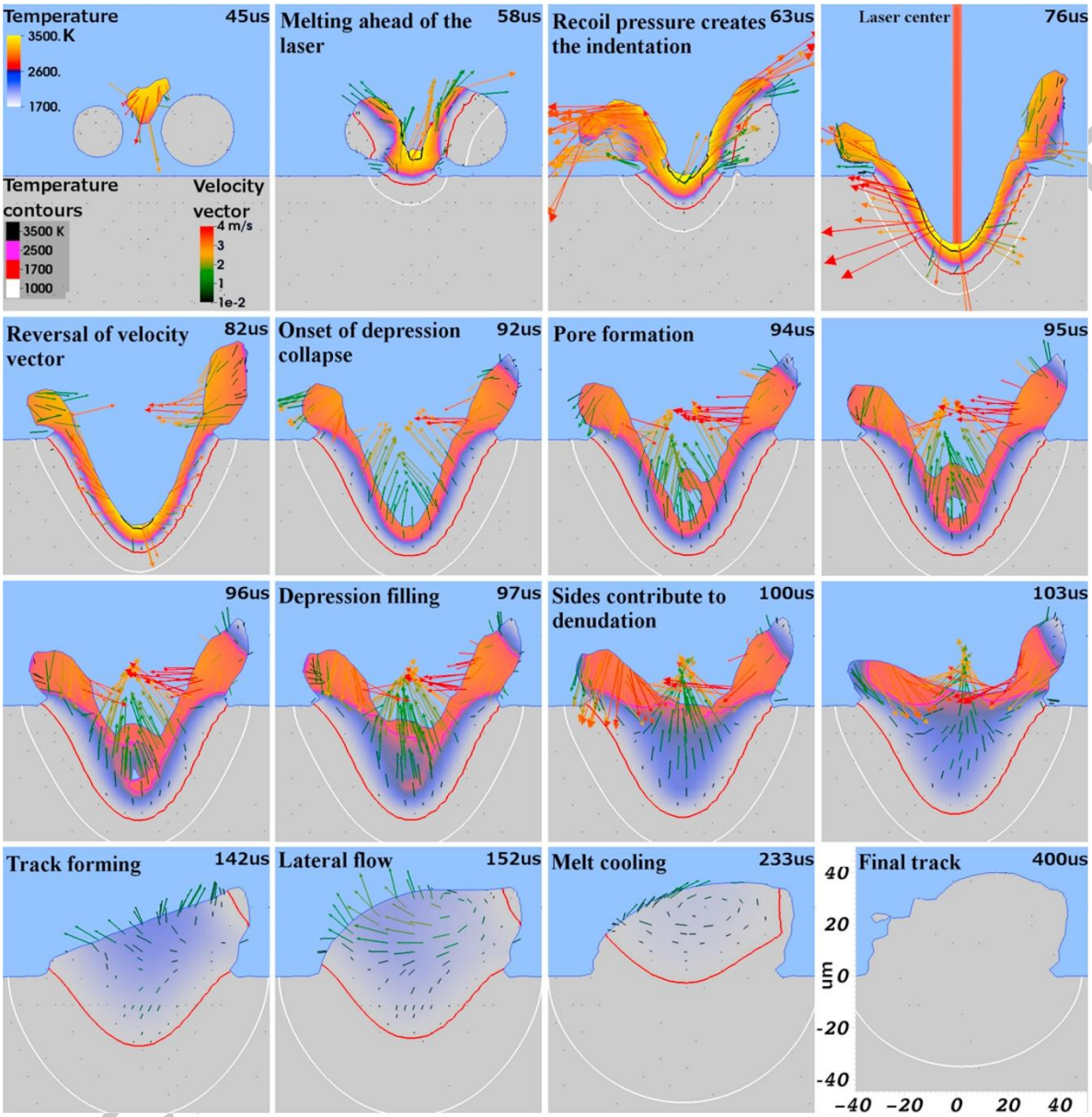

Fig. 41. Lateral 2D slices of the melt track showing the change of temperature and velocity field within the melt pool (Reproduced from [72], Copyright (2016), with permission from Elsevier).

Keyhole pores are formed due to the vaporization of the melting metals. They are reported to be spherical and trapped in the deep tail of the melt pool if they fail to escape [250]. Fig. 42 illustrates the entrapping process of keyhole pores and their positions in laser

welding [251]. The depth and shape of the keyhole fluctuate violently with large bubbles intermittently formed mainly at the bottom of the keyhole. The vapor bubbles float up to the rear of the melt pool and remain as porosity if they fail to escape before solidifying. Thijs *et al.* reported that keyhole pores tend to be formed at the end of the scan track as the fluctuation of the melt pool is more severe at the ending point [72, 198]. Keyhole pores were reported in TiB/Ti composites [134]. They were expected to form because of a larger melt pool and higher peak temperature of metals [124, 140].

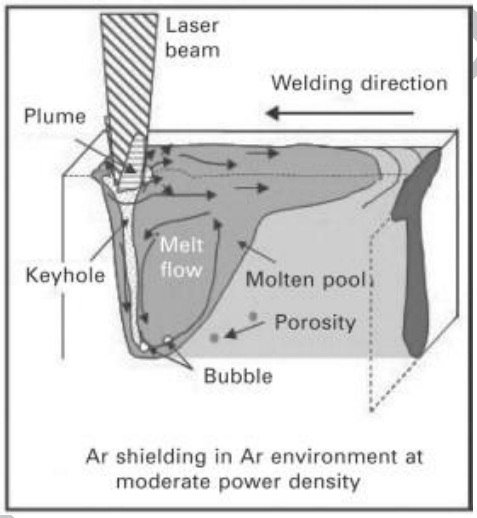

Fig. 42. Schematic of melt flows, keyhole pore formation and distribution in melt pool of welding (Reproduced from [251], Copyright (2013), with permission from Elsevier).

Hydrogen originates from powder surface moisture during SLM process. The dissolution of hydrogen in the melt pool decreases with the decreasing temperature so that hydrogen gas is mainly formed near the solidification front (Fig. 43) [252]. Powder drying process reduces the hydrogen porosity especially when an internal drying process is employed [252, 253]. Substrate pre-heating is widely used in SLM although only the several layers close to the substrate can be influenced. Internal drying process is actually the re-melting process

except that in the first scanning a lower laser power (e.g. 50W) is employed. In such a case, a higher reduction of moisture and pore density is obtained as every layer can be pre-heated to a higher drying temperature.

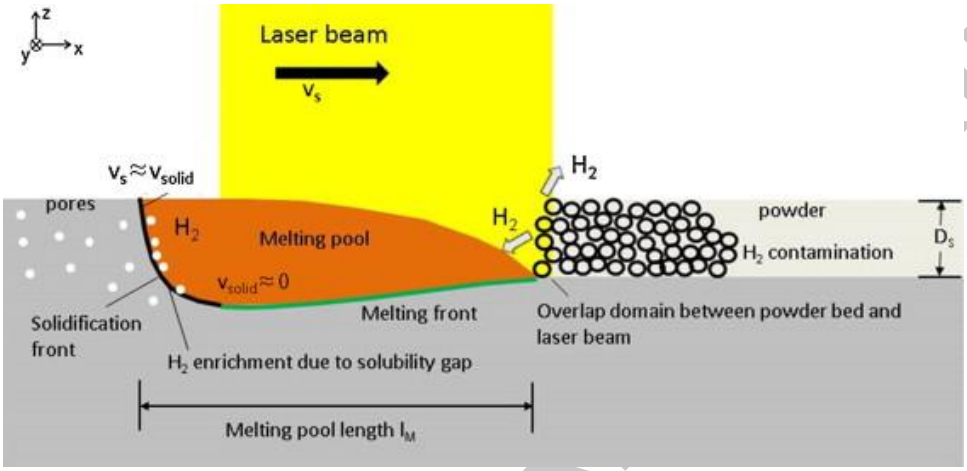

Fig. 43. Schematic of hydrogen entrapment at the solidification front in the melt pool (Reproduced from [252], Copyright (2015), with permission from Elsevier).

Gases entrapped inside the powder particles themselves due to powder atomization process can lead to pores as the gas is easily entrapped in the melts and can be eliminated by refining the powders [248]. Ball milling tends to help close the pores inside the powder particles while other methods do hot have such advantage.

Detailed porosity morphology investigation in MMNCs is in demand to understand the formation and control process. The above porosity formation discussion is all based on melt stability of the melt pool and/or the fluid flow forces. Gu *et al.* also demonstrated the importance of melt flow on gas formation with different shielding gases (Ar, He, N_2) [254]. Hence, the stability of the melt pool determines the porosity formation. The unstable fluid flow in the melt pool can be indentified by the parameter range. Kasperovich *et al.* demonstrated that scanning speed exerts the most dominant influence on the porosity

fractions (Fig. 44a) [250]. The laser power shows a distribution of an optimal parameter range allowing minimal defects (Fig. 44b). High scanning speed and low laser power are related to the lack of fusion pores while low scanning speed and high laser power correspond to the keyhole pores. Finally the hatch distance was found to be least sensitive (Fig. 44c).

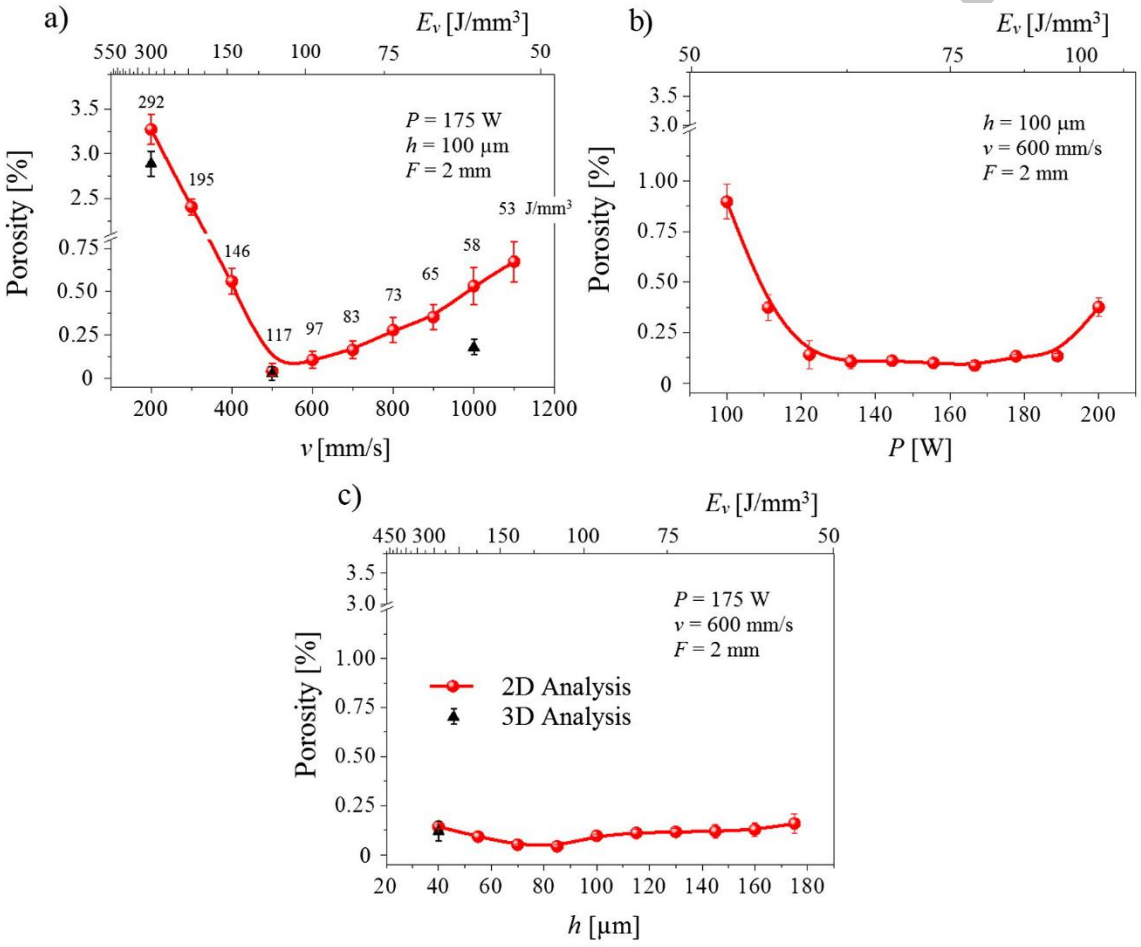

Fig. 44. The relience of porosity on the SLM process parameters (a) scan speed *v*, (b) hatch spacing *h*, and (c) laser power *P*. The volume energy density E_v, is included in the upper abscissae (Reproduced from [250], Copyright (2016), with permission from Elsevier).

4.3 Surface roughness

The concern of surface roughness has been an issue for the application of SLM parts. The condition of surface roughness is related to the foregoing discussion about balling and porosity. To be more specific, the essence can also originate from the surface motion of the melt pool. Both heat absorption and resultant fluid flow are responsible for the stability of the melt pool. High heat absorption is enhanced by nanoparticles and the stability of the melt pool is more difficult to control. For MMNCs fabricated with *in situ* chemical reaction, extra heat released also exerts an influence on the parameter optimization [184]. Surface roughness of MMNCs deserves more attention.

The possible formation of poor surface finish when the following imperfections, i.e. the un-molten powder, lack of fusion, open pores and cave-like pores, materials stacking, balling effects, are exposed at the surface of the parts [70]. These phenomena depend on laser energy input and properties of nanoparticle and have been addressed in the foregoing discussion.

It is established that powders with large size are difficult to melt and would cause higher surface roughness. Size of matrix powder would be enlarged by powder preparation methods, e.g. ball milling, detrimental to the surface finish of MMNCs parts. Therefore, poor surface roughness is a more severe issue and post processing is required.

4.4 Crack

The crack types in SLM can be categorized into hot crack and cold crack. Hot crack, also known as solidification crack, is formed at the late stage of solidification when grains form continuous skeletons. Two phenomena account for the hot crack initiation, deformation in the solid and insufficient convection in the liquid region induced by the temperature

differences during solidification with a large temperature range. It is addressed that fine equiaxed semi-solid structures reduce the entrapped liquid and allow easier grain rotation and deformation than dendrites. It provides a means to accommodate strain in the semi-solid state and thus prevents crack initiation and growth. Introduction of nanoparticles acting as nucleation sites favors dendritic-to-equiaxed transition. Martin *et al.* 3D printed crack-free Al7075 alloys with addition of zirconium particulates to form Al_3Zr in the melt pools [107]. The temperature range was not changed to a narrower one, validating influence of the grain refinement. AlSi10Mg and A6061 alloys with nanoparticles also achieve higher strength due to the elimination of solidification cracks. The grain refinement effect in nanocomposite achieved by constraining grain growth has been well addressed in literatures [78, 108, 126]. However, the presence of nanoparticles tends to increase the viscosity of the melt significantly, thus handicapping the liquid flow and decreasing the rheological performance of the melt pools. The higher volume content of nanoparticles, the higher viscosity of the melt pools. A tradeoff between the grain refinement and viscosity emerges and more detailed research is necessary to explore how the types and volume of nanoparticles influence the solidification crack.

The second type of crack caused by residual stress is more prominent in SLM process. Residual stresses in SLM are caused by two possible mechanisms, i.e. temperature gradient mechanism (TGM) and cool-down phase of the molten top layers. The first mechanism is illustrated in Fig. 45. When a laser beam is stroked onto the surface layer, a steep temperature gradient develops just underneath the laser spot due to the rapid heating and slow heat conduction. Expansion of the upper layer is restricted by the cooler underlying solidified layer, resulting in compressive stresses σ_{comp} in the upper layers. When the yield

strength is reached, the compressive stresses in the material cause plastic deformation ε_{pl}, which remain in the absence of mechanical constrain. During cooling stage, their compressive state is converted into residual tensile stresses σ_{tens} and a bending angle towards the laser beam develops. Those residual stresses may initiate cracking of the parts. The cool-down phase of the molten top layers refers to the shrinkage of the melted top due to the thermal contraction. Prohibition to the deformation by the underlying layers introduces tensile stresses in the top layer and compressive stresses below [255].

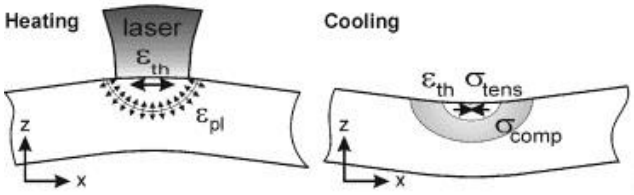

Fig. 45. Temperature gradient mechanism in SLM (Reproduced from [180], Copyright (2004), with permission from Elsevier).

Residual stress may result in cracking and interlayer de-bonding as residual stress is larger in the direction perpendicular to the scan direction than along scan direction [69]. The level of residual stress depends on material properties especially the elastic modulus CTE. Thermal stresses in multiphase materials depend on internal constraints caused by different CTE between the phases. If the thermal expansion is hindered by external constraints or uneven temperature distributions, bending stresses (σ_b) proportional to the average composite CTE are generated [256]:

$$\sigma_b = -\frac{6}{L^2}\int_{-L/2}^{L/2} E\,\alpha_t\,\Delta T X' dx \qquad (34)$$

where L is the layer thickness, E is the elastic modulus, α_t is the average CTE of the composite, ΔT is the temperature difference and X' is equal to $x - L/2$, x is the distance measured from the layer surface. The average CTE of a multiphase material (α_t) is derived as follows based on Turner Equation:

$$\alpha_t = \frac{\alpha_1 V_1 K_1 + \alpha_2 V_2 K_2 + \alpha_3 V_3 K_3 + \cdots}{V_1 K_1 + V_2 K_2 + V_3 K_3 + \cdots} \quad (35)$$

where V is the volume fraction, K is the bulk modulus and α_i is the CTE of i phase. According to Eq. (35), a lower elastic modulus and average CTE which depends on the particular CTE and volume fraction of the material constituents, favor less stress. Taking into consideration of the compatibility between matrix and reinforcement, close CTE between them is preferred. Table 6 lists the CTE of some common materials used in SLM for selection reference.

Table 6 The CTE of some common materials used in SLM.

Material	CTE (ppm/K)	Ref.
TiC	0.77	[257]
Ti_5Si_3	0.97	[257]
SiO_2	0.5	[258]
Al_2O_3	6.6	[258]
Al_2O_3	9.6	[259]
ZrO_2	15.3	[259]
hydroxyapatite	16.9	[260]
TiO_2	9.4	[259]
SiC	4.02	[261]
TiB_2	4.6	[261]
TiB_2	6.4-8.9 (50-1200 ^oC) 9.2-11.6 (50-1200 ^oC) 7.4-9.8 (50-1200 ^oC)	[262]
SiC	2.5-4	[263]
IN737 superalloy	16	[259]

AlSi7Mg	22.6-31.7 (50-500 ^{o}C)	[263]
316L steel	19.6	[264]
Ti-6Al-4V	8.92 (930 ^{o}C)	[265]
CP-Ti	9.2	[266]
NiCr alloy	13.8	[266]

Mercelis *et al.* established a relationship between the distribution of residual stress and processing parameters such as the height of sample and substrate, the scanning strategies and heating conditions in 316L stainless steel [267]. Although the quantitative results cannot be simply extrapolated to other materials [268], most qualitative results can be generalized. For instance, length and direction of scanning vectors can redistribute the stress profiles. Residual stress can also be controlled by pre-heating of the build substrate due to the decrease in temperature gradient.

Nanoparticles lead to high viscosity of the melt pools and deteriorate the rheological performance of the melt pools. To well disperse them and avoid agglomeration, a higher energy density is required. High temperature helps to compromise the effect of low viscosity on wettability and facilitates densification. However, cracks caused by residual stress are thus induced due to the high energy input and temperature gradient. Zhu *et al.* demonstrated that the thermal shrinkage during laser melting was increased with increasing laser energy input under cool-down phase mechanism [269].

Laser processing parameters should be manipulated with care to reduce the residual stress level. Good interlayer bonding is achieved when linear energy density (LED) is 375 J/m while interlayer cracks have been observed in TiC/AlSi10Mg nanocomposites with LED = 500 J/m [100]. In AlSi10Mg alloys, the processing LED below 150 J/m can be

referenced as a benchmark [270]. A higher volume fraction indicates a higher viscosity and requires laser energy input, and the crack tendency is consequently high, evidenced in TiC/316L [58] and TiC/Ti_5Si_3 [139] nanocomposites.

It is noted that the powder preparation also shows its effect. The distribution of the powder would affect the thermal behavior, thus influencing the stability of the melt pool. However, more detailed research is needed as for now only AlMangour *et al.* found that ball milled powders induced larger and more severe cracks than directly mixed powders, although the latter one revealed deep groove and pores [131].

4.5 Loss of alloying elements

High temperature of the melt pool results can result in significant vaporization of volatile elements, e.g. Mg, Zn, Li, Al, etc. with higher equilibrium vapor pressure. Fig. 46 plots the equilibrium vapor pressure of metals at different temperatures. Selective vaporization of elements would result in a change in the composition of the components and degrade mechanical properties, e.g. reducing strength, elongation, hardness [271], corrosion resistance and increasing crack susceptibility [272], which would affect the 3D printability of the matrix. According to Collur *et al.*, the vaporization mechanism can be divided into three stages, of which the first one refers to transport of vaporization elements from the bulk to the surface of the melt pool, followed by the vaporization at the liquid/vapor interface and transport of the vaporized species into the surrounding gas phases [273].

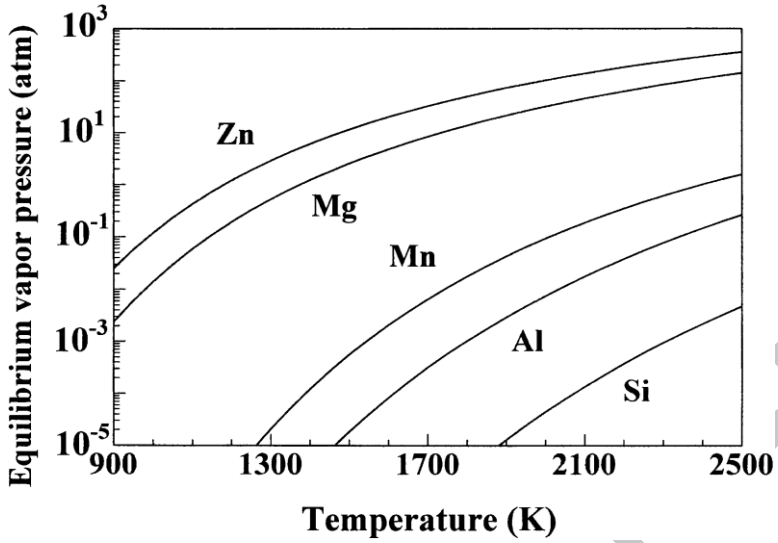

Fig. 46. Equilibrium vapor pressure of metals at different temperature (Reproduced from [272], Copyright (2001), with permission from Springer Nature).

Similar to the welding process, the change in metal composition depends on the vaporization rate and the volume of the melt pool. Although the rate of vaporization increases with laser power, the change in composition is most pronounced at low powers because of the small size and, consequently, the high surface-to-volume ratio of the melt pool. The high scanning speed ensures shorter lifetime of the melt pool and reduces vaporization [274]. As high laser power and relative low speed are usually employed when printing MMNCs, the vaporization should be more severe.

4.6 Oxide inclusions

The oxide inclusions deteriorate the densification and performance of the parts by SLM, and remain unfortunately inevitable. In SLM process, oxidation occurs on the surface of the melt pool or due to the turbulent flow in the depression position of the melt pool by entrapping of and reacting with the oxygen impurity in the shielding gas. Simonelli *et al.* compared the composition of starting particles of 316L stainless steel, AlSi10Mg, and Ti-

6Al-4V alloys directly with the laser spatters and revealed oxide films on the surfaces of 316L stainless steel and AlSi10Mg spatters but no oxidation on that of Ti-6Al-4V powders [171]. The oxides are underpinned by surface enrichment of the most volatile element present in the alloys. If these elements (Mn and Si in 316L stainless steel, and Mg in AlSi10Mg) have a great affinity for oxygen, oxides can be formed. Magnesium oxide films in aluminum alloys contain spinel ($MgO.Al_2O_3$) and MgO depending on the Mg contents. However, it is argued that the protective oxide layers are thinner in typical metals such as 316L stainless steel and titanium alloys than in aluminum alloys and have a negligible effect on the SLM production, because they can be disrupted and stirred in the melt pool or vaporized by the laser beam [90]. Since aluminum has a great affinity to oxygen and can form thicker oxide films even with dissociation pressure of alumina being rather low (10^{-52} pO_2) at the melting point of aluminum, oxide films cannot be avoided with even low oxygen concentration. Therefore, most researchers focus on aluminum components. There are two sides, wetted side and dry side, of oxidation films. The wetted side may nucleate intermetallics while the unwetted dry side is potential nucleation sites for porosity. That is why most oxide films locate at the pore boundary [193]. As aluminum dendrites may not grow through the unwetted dry side of oxide films, oxides may also distribute at the grain boundaries. Oxides films are always folded dry side to dry side as observed in convectional castings and laser welded aluminum alloys [275, 276].

Measures must be taken to eliminate the oxide films because they not only degrade the densification behavior but also can initiate cracks [270]. A high energy density is required to break up the oxide films. However, only the oxide films at the bottom of the melt pool can be interrupted due to stronger Marangoni flow, while those at the sides of the melt pool

remain intact, creating the 'walls' of oxides. Therefore, new methods of controlling the oxidation process and disrupting oxide films formed within the components, for example, optimal scanning strategy, should be further developed. The higher energy density employed in MMNCs seems to be more effective in breaking up the oxide films though it induces higher affinity to oxygen. However, no comparable data has been offered.

5. Applications

While the applications of SLM MMNCs may not have been as established as those fabricated by conventional methods, the potential of the synergy between this manufacturing process and class of materials can be realized. The potential applications of such materials in various industries are summarized in Table 7.

Table 7 Potential applications for SLM MMNCs.

Industry	Examples of applications	Desired properties
Aerospace	Aircraft brakes, landing gears	Good wear resistance, good thermal conductivity, low density, high strength
Space	High gain antenna boom, structural radiators	Low density, high strength, low CTE, good electrical conductivity
Automobile	Break shoes, cylinder liners, piston rings, gears	High strength, wear resistance, good thermal conductivity, low density
Electronics (MEMS, sensors, battery and energy storage)	Micro-beams, micro-gears, anodes and anode coatings	High elastic modulus, high surface area, high current density, reduced response times
Biomedical	Orthopedic implants, surface coating	High strength, low modulus, high corrosion resistance

Sports	Light weight bicycles, tennis and badminton rackets	High strength, high elastic modulus

5.1 Aerospace and space

Due to the extreme environment in space, MMCs provide a unique class of materials for use due to their high specific stiffness and near-zero CTE. In addition, they have high temperature capability, high thermal conductivity and strength [8, 277]. Aluminum based MMNCs are widely used in aerospace industry for structural parts such as rotor vanes, drive shaft and rotor plates [277]. Al6061 reinforced with 50 % B monofilaments is used in 243 MMC tubes for construction of each Space Shuttle Orbiter mid-fuselage main frame and rib truss members, frame stabilizing struts and nose landing gear and drag brace supports [278]. However, the difficulty associated with manufacturing and resultant high cost have limited this MMC system for future use. SLM has the potential to bring down this manufacturing cost.

5.2 Automobile

Aluminum is one of the most commonly used metals in automobile industry. However, it is well established that a soft metal like aluminum slides on hard steel without any external fluid or solid lubrication [279]. Graphite can act as a solid lubricant in aluminum matrices. However, there is a challenge of graphite rejection by the liquid aluminum during the conventional casting method [279]. Aluminum based particulate composites, mainly made up of SiC/Al and Al/Al_2O_3, have been successfully used in pistons, engine blocks, disc rotor brakes, drums, calipers, connecting rods, drive shafts, snow tire studs and other

automobile parts [277-279]. Such combinations of MMNCs have been produced by SLM, which can overcome some of the challenges faced by conventional methods [54, 277, 280, 281].

5.3 Electronics and electronic packaging

Thermal management is important in a wide range of applications, such as substrates for computer processor chips, powder semiconductor devices and packaging for microwave devices in telecommunication. Although the specific thermal conductivity of aluminum is higher than any other metals, the CTE is too high to be useful. Additions of SiC decrease the CTE without significantly degrading the specific thermal conductivity [278].

Heat sinks have been successfully fabricated using SLM [282-284]. While MMCs have not been used in these heat sinks yet, there is potential for such applications as aluminum based and copper based composites have been successfully fabricated using SLM [54, 285].

5.4 Biomedical

While not as actively used as in automobile or aerospace, MMCs have also been researched for use in biomedical applications. The advantages of using MMCs are adjustable mechanical and corrosion properties [286]. With SLM, they have the potential to eliminate the problem of bone remodeling due to mismatch in mechanical properties by varying the compositions of these MMNCs continuously or discretely to match the required properties [287]. A thorough review on MMNCs in biomedical applications, in particular for implants, devices with enhanced wear resistance and hard tissue engineering such as bone and tooth, have been given by Bose *et al.* [288]. Chen *et al.* studied the corrosion behavior of SLM Ti-TiB MMNCs in simulated body fluid and concluded that they have

better corrosion resistance than pure titanium produced by SLM as the TiB particles act as micro-cathode and the titanium matrix acts as anode during corrosion process, which facilitates the formation of a protective film on the surface, in the Hank's solution at body temperature [289].

6. Summary and research trends

An analysis of the available literatures on SLM processing of MMNCs has revealed its importance and explored the possibilities it offers for engineering applications. The SLM technique will be increasingly employed for fabricating high quality, low cost and repeatable MMNCs parts in automotive, aerospace, electronics and biomedical industries. It aids manufacturing in these areas to deliver new customized products quicker into application and has the potential to gain more consumer markets. This review brings deep insight into the fabrication, mechanical properties and defects of MMNCs using SLM.

Fabrication feasibility is considered from the perspectives of materials and processing parameters. The main issues of MMNCs production arise from the limited wettability of the matrix alloys and the tendency to agglomerate for the nanoparticles. Although various methods have been adopted to prepare the feedstock, more efficient and economic processes are in demand, especially in industrial production. Reinforcement introduction modifies the physical properties of powder materials and affects the heat transfer and fluid flow behavior. This review has addressed the influence of heat transfer and fluid flow on the dispersion of nanoparticles and the resultant microstructure. SLM processing windows of MMNCs components witness a shift compared to the matrix metal alloys due to the change of physical properties and thermal history. Mechanical properties (strength, microhardness and fatigue) depend on the size and distribution of nanoparticles as well as

the interface between matrix and reinforcement. Enhancing mechanisms associated with nanoparticles of different properties have been discussed, providing a basis of understanding of MMNCs optimization. Defects associated with SLM need to be carefully controlled as MMNCs especially those fabricated with *ex situ* methods typically have narrow SLM processing windows. Balling effect, porosity, crack, loss of alloying elements and oxide inclusions have all been discussed.

Despite extensive investigations and encouraging prospective, research in this field is relatively new in infancy stage. Numerous issues are still challenging in terms of the future development of MMNCs with SLM. Future research for a better understanding of fundamental and technological issues is therefore recommended hereinafter.

Printability development never loses its attraction. Although much progress has been achieved in modifying 3D printability of alloys, there are still limited options available nowadays. The technique for well dispersing ceramic nanoparticles is another challenging problem. These two aspects determine the accessibility to 3D printing and require further and long-run investigations for MMNCs. In the meanwhile, the processing window for each material vary due to the interaction of the matrix and reinforcement. Extensive experimental research is a necessity for successful production.

In an attempt to clarify new phenomena induced by nanoparticles, numerical and experimental methods should be further developed. Simulation of the behavior in melt pools of MMNCs is required to explicate the change induced by nanoparticles, the report on which is limited at present. With deep insight into the physical modeling, a better understanding and good manipulating of parameters optimization can be achieved. Nowadays various *in situ* techniques such as operando high-speed synchrotron X-ray

imaging were employed to reveal the real-time process of defects formation. This can be also used in studying the behavior of nanoparticles. Accelerated trials and investigations for various applications to come to fruition are the final goals in the subsequent research.

The significant progress in SLM in the last decades promises a prosperous market for metals 3D printing and allows confidence to look forward to the advancement of MMNCs by 3D printing. There is no doubt that in the near future MMNCs of high quality produced by SLM will be fabricated reliably, with a better fundamental understanding expected.

Acknowledgements

We acknowledge the support from the National Research Foundation, Prime Minister's Office, Singapore under its Medium-Sized Centre funding scheme and National Natural Science Foundation of China (Project No. 51371109). Wenhui Yu also appreciates the sponsorship from China Scholarship Council (Sponsorship No. 201706220205).

References

[1] Casati R, Vedani M. Metal Matrix Composites Reinforced by Nano-Particles—A Review. Metals. 2014;4:65-83.

[2] González C, Vilatela JJ, Molina-Aldareguía JM, Lopes CS, Llorca J. Structural composites for multifunctional applications: Current challenges and future trends. Prog Mater Sci. 2017;89:194-251.

[3] Gu D, Chang F, Dai D. Selective laser melting additive manufacturing of novel aluminum based composites with multiple reinforcing phases. J Manuf Sci Eng. 2014;137:021010.

[4] Zhou W, Xu ZM. Casting of SiC reinforced metal matrix composites. J Mater Process Technol. 1997;63:358-63.

[5] Ibrahim IA, Mohamed FA, Lavernia EJ. Particulate reinforced metal matrix composites—a review. J Mater Sci. 1991;26:1137-56.

[6] Doel TJA, Loretto MH, Bowen P. Mechanical properties of aluminium-based particulate metal-matrix composites. Composites. 1993;24:270-5.

[7] Kainer KU. Metal matrix composites: custom-made materials for automotive and aerospace engineering. New York: John Wiley & Sons; 2006.

[8] Rawal SP. Metal-matrix composites for space applications. JOM. 2001;53:14-7.

[9] Moya J, Lopezesteban S, Pecharroman C. The challenge of ceramic/metal microcomposites and nanocomposites. Prog Mater Sci. 2007;52:1017-90.

[10] Mortensen A, Llorca J. Metal Matrix Composites. Annu Rev Mater Res. 2010;40:243-70.

[11] Kang Y-C, Chan SL-I. Tensile properties of nanometric Al_2O_3 particulate-reinforced aluminum matrix composites. Mater Chem Phys. 2004;85:438-43.

[12] Tjong SC. Novel Nanoparticle-Reinforced Metal Matrix Composites with Enhanced Mechanical Properties. Adv Eng Mater. 2007;9:639-52.

[13] Sajjadi SA, Ezatpour HR, Beygi H. Microstructure and mechanical properties of Al–Al_2O_3 micro and nano composites fabricated by stir casting. Mater Sci Eng, A. 2011;528:8765-71.

[14] Knowles AJ, Jiang X, Galano M, Audebert F. Microstructure and mechanical properties of 6061 Al alloy based composites with SiC nanoparticles. J Alloys Compd. 2014;615:S401-S5.

[15] Mohammad Sharifi E, Karimzadeh F, Enayati MH. Fabrication and evaluation of mechanical and tribological properties of boron carbide reinforced aluminum matrix nanocomposites. Mater Des. 2011;32:3263-71.

[16] Sajjadi SA, Ezatpour H, Parizi MT. Comparison of microstructure and mechanical properties of A356 aluminum alloy/Al_2O_3 composites fabricated by stir and compo-casting processes. Mater Des. 2012;34:106-11.

[17] Kandemir S, Yalamanchili A, Atkinson HV. Production of aluminium matrix nanocomposite feedstock for thixoforming by an ultrasonic method. Key Eng Mater: Trans Tech Publ; 2012. p. 339-44.

[18] Turng L-S, DeCicco MP, Li X. Semi-solid forming of metal-matrix nanocomposites. Google Patents; 2009.

[19] Hsu CJ, Chang CY, Kao PW, Ho NJ, Chang CP. Al–Al_3Ti nanocomposites produced in situ by friction stir processing. Acta Mater. 2006;54:5241-9.

[20] Du ZL, Tan MJ, Guo JF, Wei J, Chua CK. Dispersion of CNTs in selective laser melting printed AlSi10Mg composites via friction stir processing. Mater Sci Forum: Trans Tech Publ; 2017. p. 1915-20.

[21] Lan J, Yang Y, Li X. Microstructure and microhardness of SiC nanoparticles reinforced magnesium composites fabricated by ultrasonic method. Mater Sci Eng, A. 2004;386:284-90.

[22] Li X, Yang Y, Cheng X. Ultrasonic-assisted fabrication of metal matrix nanocomposites. J Mater Sci. 2004;39:3211-2.

[23] Huang LJ, Geng L, Li AB, Yang FY, Peng HX. In situ TiBw/Ti–6Al–4V composites with novel reinforcement architecture fabricated by reaction hot pressing. Scripta Mater. 2009;60:996-9.

[24] Huang LJ, Geng L, Peng HX, Zhang J. Room temperature tensile fracture characteristics of in situ TiBw/Ti6Al4V composites with a quasi-continuous network architecture. Scripta Mater. 2011;64:844-7.

[25] Huang LJ, Wang S, Dong YS, Zhang YZ, Pan F, Geng L, et al. Tailoring a novel network reinforcement architecture exploiting superior tensile properties of in situ TiBw/Ti composites. Mater Sci Eng, A. 2012;545:187-93.

[26] Saheb N, Iqbal Z, Khalil A, Hakeem AS, Al Aqeeli N, Laoui T, et al. Spark Plasma Sintering of Metals and Metal Matrix Nanocomposites: A Review. J Nanomater. 2012;2012:1-13.

[27] Azarniya A, Azarniya A, Sovizi S, Hosseini HRM, Varol T, Kawasaki A, et al. Physicomechanical properties of spark plasma sintered carbon nanotube-reinforced metal matrix nanocomposites. Prog Mater Sci. 2017;90:276-324.

[28] Das S. Physical Aspects of Process Control in Selective Laser Sintering of Metals. Adv Eng Mater. 2003;5:701-11.

[29] Suryanarayana C, Al-Aqeeli N. Mechanically alloyed nanocomposites. Prog Mater Sci. 2013;58:383-502.

[30] Sivananth V, Vijayarangan S, Rajamanickam N. Evaluation of fatigue and impact behavior of titanium carbide reinforced metal matrix composites. Mater Sci Eng, A. 2014;597:304-13.

[31] Sing SL, Yeong WY, Wiria FE, Tay BY. Characterization of titanium lattice structures fabricated by selective laser melting using an adapted compressive test method. Exp Mech. 2016;56:735-48.

[32] Liu ZH, Zhang DQ, Chua CK, Leong KF. Crystal structure analysis of M2 high speed steel parts produced by selective laser melting. Mater Charact. 2013;84:72-80.

[33] Sing SL, Lam LP, Zhang DQ, Liu ZH, Chua CK. Interfacial characterization of SLM parts in multi-material processing: Intermetallic phase formation between AlSi10Mg and C18400 copper alloy. Mater Charact. 2015;107:220-7.

[34] Herzog D, Seyda V, Wycisk E, Emmelmann C. Additive manufacturing of metals. Acta Mater. 2016;117:371-92.

[35] Sing SL, Yeong WY, Wiria FE, Tay BY, Zhao Z, Zhao L, et al. Direct selective laser sintering and melting of ceramics: a review. Rapid Prototyping J. 2017;23:611-23.

[36] Yap C, Chua C, Dong Z, Liu Z, Zhang D, Loh L, et al. Review of selective laser melting: Materials and applications. Appl Phys Rev. 2015;2:041101.

[37] Chua CK, Leong KF. 3D Printing and Additive Manufacturing: Principles and Applications Fifth Edition of Rapid Prototyping Fifth Edition: World Scientific Publishing Company; 2016.

[38] Wu W, Tor SB, Chua CK, Leong KF, Merchant A. Investigation on processing of ASTM A131 Eh36 high tensile strength steel using selective laser melting. Virtual Phys Prototyp. 2015;10:187-93.

[39] Liu J, Li J, Xu C. Interaction of the cutting tools and the ceramic-reinforced metal matrix composites during micro-machining: a review. CIRP-JMST. 2014;7:55-70.

[40] Li S, Wei Q, Shi Y, Zhu Z, Zhang D. Microstructure characteristics of Inconel 625 superalloy manufactured by selective laser melting. J Mater Sci Technol. 2015;31:946-52.

[41] Yang J, Yu H, Yin J, Gao M, Wang Z, Zeng X. Formation and control of martensite in Ti-6Al-4V alloy produced by selective laser melting. Mater Des. 2016;108:308-18.

[42] Liu ZH, Zhang DQ, Sing SL, Chua CK, Loh LE. Interfacial characterization of SLM parts in multi-material processing: Metallurgical diffusion between 316L stainless steel and C18400 copper alloy. Mater Charact. 2014;94:116-25.

[43] Yang C, Zhao YJ, Kang LM, Li DD, Zhang WW, Zhang LC. High-strength silicon brass manufactured by selective laser melting. Mater Lett. 2018;210:169-72.

[44] Sun Z, Tan X, Tor SB, Chua CK. Simultaneously enhanced strength and ductility for 3D-printed stainless steel 316L by selective laser melting. NPG Asia Mater. 2018;10:127-36.

[45] Attar H, Bönisch M, Calin M, Zhang L-C, Zhuravleva K, Funk A, et al. Comparative study of microstructures and mechanical properties of in situ Ti–TiB composites produced by selective laser melting, powder metallurgy, and casting technologies. J Mater Res. 2014;29:1941-50.

[46] Zhang LC, Xu J, Eckert J. Thermal stability and crystallization kinetics of mechanically alloyed TiC/Ti-based metallic glass matrix composite. J Appl Phys. 2006;100:033514.

[47] Liu LH, Yang C, Wang F, Qu SG, Li XQ, Zhang WW, et al. Ultrafine grained Ti-based composites with ultrahigh strength and ductility achieved by equiaxing microstructure. Mater Des. 2015;79:1-5.

[48] Kühn U, Mattern N, Gebert A, Kusy M, Boström M, Siegel U, et al. Nanostructured Zr-and Ti-based composite materials with high strength and enhanced plasticity. J Appl Phys. 2005;98:054307.

[49] AlMangour B, Baek M-S, Grzesiak D, Lee K-A. Strengthening of stainless steel by titanium carbide addition and grain refinement during selective laser melting. Mater Sci Eng, A. 2018;712:812-8.

[50] Gu D, Shen Y. Direct laser sintered WC-10Co/Cu nanocomposites. Appl Surf Sci. 2008;254:3971-8.

[51] DebRoy T, Wei HL, Zuback JS, Mukherjee T, Elmer JW, Milewski JO, et al. Additive manufacturing of metallic components – Process, structure and properties. Prog Mater Sci. 2018;92:112-224.

[52] Gu DD, Meiners W, Wissenbach K, Poprawe R. Laser additive manufacturing of metallic components: materials, processes and mechanisms. Int Mater Rev. 2013;57:133-64.

[53] Olakanmi EO, Cochrane RF, Dalgarno KW. A review on selective laser sintering/melting (SLS/SLM) of aluminium alloy powders: Processing, microstructure, and properties. Prog Mater Sci. 2015;74:401-77.

[54] Sercombe TB, Li X. Selective laser melting of aluminium and aluminium metal matrix composites: a review. Mater Technol. 2016;31:77-85.

[55] Yadroitsev I, Gusarov A, Yadroitsava I, Smurov I. Single track formation in selective laser melting of metal powders. J Mater Process Technol. 2010;210:1624-31.

[56] Markl M, Körner C. Multiscale Modeling of Powder Bed–Based Additive Manufacturing. Annu Rev Mater Res. 2016;46:93-123.

[57] Li Y, Zhou K, Tor SB, Chua CK, Leong KF. Heat transfer and phase transition in the selective laser melting process. Int J Heat Mass Transfer. 2017;108:2408-16.

[58] AlMangour B, Grzesiak D, Borkar T, Yang J-M. Densification behavior, microstructural evolution, and mechanical properties of TiC/316L stainless steel nanocomposites fabricated by selective laser melting. Mater Des. 2018;138:119-28.

[59] Wang XC, Laoui T, Bonse J, Kruth J-P, Lauwers B, Froyen L. Direct selective laser sintering of hard metal powders: experimental study and simulation. Int J Adv Manuf Tech. 2002;19:351-7.

[60] Ahn IH, Moon SK, Hwang J, Bi G. Characteristic length of the solidified melt pool in selective laser melting process. Rapid Prototyping J. 2017;23:370-81.

[61] Scharowsky T, Osmanlic F, Singer RF, Körner C. Melt pool dynamics during selective electron beam melting. Appl Phys A. 2013;114:1303-7.

[62] Arafune K, Hirata A. Thermal and solutal Marangoni convection in In–Ga–Sb system. J Cryst Growth. 1999;197:811-7.

[63] Kovalev OB, Gurin AM. Multivortex convection of metal in molten pool with dispersed impurity induced by laser radiation. Int J Heat Mass Transfer. 2014;68:269-77.

[64] Chan CL, Mazumder J, Chen MM. Effect of surface tension gradient driven convection in a laser melt pool: Three-dimensional perturbation model. J Appl Phys. 1988;64:6166-74.

[65] Rongy L, De Wit A. Steady Marangoni flow traveling with chemical fronts. J Chem Phys. 2006;124:164705.

[66] Fabbro R, Hamadou M, Coste F. Metallic vapor ejection effect on melt pool dynamics in deep penetration laser welding. J Laser Appl. 2004;16:16-9.

[67] Fabbro R, Slimani S, Doudet I, Coste F, Briand F. Experimental study of the dynamical coupling between the induced vapour plume and the melt pool for Nd–Yag CW laser welding. J Phys D: Appl Phys. 2006;39:394-400.

[68] Liu Y, Yang Y, Mai S, Wang D, Song C. Investigation into spatter behavior during selective laser melting of AiSi 316L stainless steel powder. Mater Des. 2015;87:797-806.

[69] Loh LE, Chua CK, Yeong WY, Song J, Mapar M, Sing SL, et al. Numerical investigation and an effective modelling on the Selective Laser Melting (SLM) process with aluminium alloy 6061. Int J Heat Mass Transfer. 2015;80:288-300.

[70] Dai D, Gu D. Tailoring surface quality through mass and momentum transfer modeling using a volume of fluid method in selective laser melting of TiC/AlSi10Mg powder. Int J Mach Tool Manu. 2015;88:95-107.

[71] Dai K, Shaw L. Thermal and mechanical finite element modeling of laser forming from metal and ceramic powders. Acta Mater. 2004;52:69-80.

[72] Khairallah SA, Anderson AT, Rubenchik A, King WE. Laser powder-bed fusion additive manufacturing: Physics of complex melt flow and formation mechanisms of pores, spatter, and denudation zones. Acta Mater. 2016;108:36-45.

[73] Spierings AB, Voegtlin M, Bauer T, Wegener K. Powder flowability characterisation methodology for powder-bed-based metal additive manufacturing. Prog Addit Manuf. 2015;1:9-20.

[74] Strondl A, Lyckfeldt O, Brodin H, Ackelid U. Characterization and Control of Powder Properties for Additive Manufacturing. JOM. 2015;67:549-54.

[75] El-Kady O, Fathy A. Effect of SiC particle size on the physical and mechanical properties of extruded Al matrix nanocomposites. Mater Des. 2014;54:348-53.

[76] Hassan SF, Gupta M. Development of nano-Y_2O_3 containing magnesium nanocomposites using solidification processing. J Alloys Compd. 2007;429:176-83.

[77] Ying DY, Zhang DL. Processing of Cu–Al_2O_3 metal matrix nanocomposite materials by using high energy ball milling. Mater Sci Eng, A. 2000;286:152-6.

[78] Li XP, Ji G, Chen Z, Addad A, Wu Y, Wang HW, et al. Selective laser melting of nano-TiB_2 decorated AlSi10Mg alloy with high fracture strength and ductility. Acta Mater. 2017;129:183-93.

[79] Zhang D, Liu Z, Cai Q, Liu J, Chua C. Influence of Ni content on microstructure of W–Ni alloy produced by selective laser melting. Int J Refract Met Hard Mater. 2014;45:15-22.

[80] Sing SL, Yeong WY, Wiria FE. Selective laser melting of titanium alloy with 50 wt% tantalum: Microstructure and mechanical properties. J Alloys Compd. 2016;660:461-70.

[81] Yap CY, Tan HK, Du Z, Chua CK, Dong Z. Selective laser melting of nickel powder. Rapid Prototyping J. 2017;23:750-7.

[82] Khoo ZX, Liu Y, Low ZH, An J, Chua CK, Leong KF. Fabrication of SLM NiTi shape memory alloy via repetitive laser scanning. Shap Mem Superelasticity. 2018;4:112-20.

[83] Khoo ZX, Liu Y, An J, Chua CK, Shen YF, Kuo CN. A Review of Selective Laser Melted NiTi Shape Memory Alloy. Materials. 2018;11:519.

[84] Kimura T, Nakamoto T, Mizuno M, Araki H. Effect of silicon content on densification, mechanical and thermal properties of Al-xSi binary alloys fabricated using selective laser melting. Mater Sci Eng, A. 2017;682:593-602.

[85] Khan M, Dickens P. Selective Laser Melting (SLM) of pure gold. Gold Bull. 2010;43:114-21.

[86] Olakanmi E. Selective laser sintering/melting (SLS/SLM) of pure Al, Al–Mg, and Al–Si powders: Effect of processing conditions and powder properties. J Mater Process Technol. 2013;213:1387-405.

[87] Gu D, Hagedorn Y-C, Meiners W, Meng G, Batista RJS, Wissenbach K, et al. Densification behavior, microstructure evolution, and wear performance of selective laser melting processed commercially pure titanium. Acta Mater. 2012;60:3849-60.

[88] Vrancken B, Thijs L, Kruth JP, Van Humbeeck J. Microstructure and mechanical properties of a novel β titanium metallic composite by selective laser melting. Acta Mater. 2014;68:150-8.

[89] Kaufmann N, Imran M, Wischeropp TM, Emmelmann C, Siddique S, Walther F. Influence of Process Parameters on the Quality of Aluminium Alloy EN AW 7075 Using Selective Laser Melting (SLM). Phys Procedia. 2016;83:918-26.

[90] Louvis E, Fox P, Sutcliffe CJ. Selective laser melting of aluminium components. J Mater Process Technol. 2011;211:275-84.

[91] Zhang L-C, Attar H. Selective Laser Melting of Titanium Alloys and Titanium Matrix Composites for Biomedical Applications: A Review Adv Eng Mater. 2016;18:463-75.

[92] Attar H, Calin M, Zhang LC, Scudino S, Eckert J. Manufacture by selective laser melting and mechanical behavior of commercially pure titanium. Mater Sci Eng, A. 2014;593:170-7.

[93] Vrancken B, Thijs L, Kruth J-P, Van Humbeeck J. Heat treatment of Ti6Al4V produced by Selective Laser Melting: Microstructure and mechanical properties. J Alloys Compd. 2012;541:177-85.

[94] Li W, Li S, Liu J, Zhang A, Zhou Y, Wei Q, et al. Effect of heat treatment on AlSi10Mg alloy fabricated by selective laser melting: Microstructure evolution, mechanical properties and fracture mechanism. Mater Sci Eng, A. 2016;663:116-25.

[95] Kimura T, Nakamoto T. Microstructures and mechanical properties of A356 (AlSi7Mg0.3) aluminum alloy fabricated by selective laser melting. Mater Des. 2016;89:1294-301.

[96] AlMangour B, Grzesiak D, Yang J-M. Selective laser melting of TiB_2/316L stainless steel composites: The roles of powder preparation and hot isostatic pressing post-treatment. Powder Technol. 2017;309:37-48.

[97] AlMangour B, Grzesiak D, Yang J-M. In-situ formation of novel TiC-particle-reinforced 316L stainless steel bulk-form composites by selective laser melting. J Alloys Compd. 2017;706:409-18.

[98] AlMangour B, Grzesiak D, Yang J-M. Nanocrystalline TiC-reinforced H13 steel matrix nanocomposites fabricated by selective laser melting. Mater Des. 2016;96:150-61.

[99] Chang F, Gu D, Dai D, Yuan P. Selective laser melting of in-situ Al4SiC4+ SiC hybrid reinforced Al matrix composites: Influence of starting SiC particle size. Surf Coat Technol. 2015;272:15-24.

[100] Yuan P, Gu D. Molten pool behaviour and its physical mechanism during selective laser melting of TiC/AlSi10Mg nanocomposites: simulation and experiments. J Phys D: Appl Phys. 2015;48:035303.

[101] Dai D, Gu D. Influence of thermodynamics within molten pool on migration and distribution state of reinforcement during selective laser melting of AlN/AlSi10Mg composites. Int J Mach Tool Manu. 2016;100:14-24.

[102] Gu D, Meng G, Li C, Meiners W, Poprawe R. Selective laser melting of TiC/Ti bulk nanocomposites: Influence of nanoscale reinforcement. Scripta Mater. 2012;67:185-8.

[103] Gu D, Shen Y, Meng G. Growth morphologies and mechanisms of TiC grains during Selective Laser Melting of Ti–Al–C composite powder. Mater Lett. 2009;63:2536-8.

[104] Gu D, Wang Z, Shen Y, Li Q, Li Y. In-situ TiC particle reinforced Ti–Al matrix composites: Powder preparation by mechanical alloying and Selective Laser Melting behavior. Appl Surf Sci. 2009;255:9230-40.

[105] Yao X, Moon SK, Lee BY, Bi G. Effects of heat treatment on microstructures and tensile properties of IN718/TiC nanocomposite fabricated by selective laser melting. Int J Precis Eng Man. 2017;18:1693-701.

[106] Hong C, Gu D, Dai D, Gasser A, Weisheit A, Kelbassa I, et al. Laser metal deposition of TiC/Inconel 718 composites with tailored interfacial microstructures. Opt Laser Technol. 2013;54:98-109.

[107] Martin JH, Yahata BD, Hundley JM, Mayer JA, Schaedler TA, Pollock TM. 3D printing of high-strength aluminium alloys. Nature. 2017;549:365-9.

[108] AlMangour B, Grzesiak D, Yang J-M. Rapid fabrication of bulk-form TiB_2/316L stainless steel nanocomposites with novel reinforcement architecture and improved performance by selective laser melting. J Alloys Compd. 2016;680:480-93.

[109] Gu D, Wang H, Zhang G. Selective laser melting additive manufacturing of Ti-based nanocomposites: the role of nanopowder. Metall Mater Trans A. 2014;45:464-76.

[110] Song B, Dong S, Coddet P, Zhou G, Ouyang S, Liao H, et al. Microstructure and tensile behavior of hybrid nano-micro SiC reinforced iron matrix composites produced by selective laser melting. J Alloys Compd. 2013;579:415-21.

[111] Wei Q, Li S, Han C, Li W, Cheng L, Hao L, et al. Selective laser melting of stainless-steel/nano-hydroxyapatite composites for medical applications: Microstructure, element distribution, crack and mechanical properties. J Mater Process Technol. 2015;222:444-53.

[112] Wang H, Gu D. Nanometric TiC reinforced AlSi10Mg nanocomposites: Powder preparation by high-energy ball milling and consolidation by selective laser melting. J Compos Mater. 2014;49:1639-51.

[113] Gu D, Ma C, Xia M, Dai D, Shi Q. A multiscale understanding of the thermodynamic and kinetic mechanisms of laser additive manufacturing. Engineering. 2017;3:675-84.

[114] AlMangour B, Grzesiak D, Yang J-M. Scanning strategies for texture and anisotropy tailoring during selective laser melting of TiC/316L stainless steel nanocomposites. J Alloys Compd. 2017;728:424-35.

[115] Han Q, Setchi R, Evans SL. Synthesis and characterisation of advanced ball-milled Al-Al_2O_3 nanocomposites for selective laser melting. Powder Technol. 2016;297:183-92.

[116] Gu D, Shen Y, Lu Z. Preparation of TiN–Ti_5Si_3 in-situ composites by Selective Laser Melting. Mater Lett. 2009;63:1577-9.

[117] Dadbakhsh S, Hao L. Effect of Al alloys on selective laser melting behaviour and microstructure of in situ formed particle reinforced composites. J Alloys Compd. 2012;541:328-34.

[118] Li W, Yang Y, Liu J, Zhou Y, Li M, Wen S, et al. Enhanced nanohardness and new insights into texture evolution and phase transformation of TiAl/TiB_2 in-situ metal matrix composites prepared via selective laser melting. Acta Mater. 2017;136:90-104.

[119] Attar H, Prashanth KG, Zhang L-C, Calin M, Okulov IV, Scudino S, et al. Effect of Powder Particle Shape on the Properties of In Situ Ti–TiB Composite Materials Produced by Selective Laser Melting. J Mater Sci Technol. 2015;31:1001-5.

[120] Song B, Wang Z, Yan Q, Zhang Y, Zhang J, Cai C, et al. Integral method of preparation and fabrication of metal matrix composite: Selective laser melting of in-situ nano/submicro-sized carbides reinforced iron matrix composites. Mater Sci Eng, A. 2017;707:478-87.

[121] Chen M, Li X, Ji G, Wu Y, Chen Z, Baekelant W, et al. Novel Composite Powders with Uniform TiB_2 Nano-Particle Distribution for 3D Printing. Appl Sci. 2017;7:250.

[122] Zhou W, Sun X, Kikuchi K, Nomura N, Yoshimi K, Kawasaki A. Carbon nanotubes as a unique agent to fabricate nanoceramic/metal composite powders for additive manufacturing. Mater Des. 2018;137:276-85.

[123] Tan H, Hao D, Al-Hamdani K, Zhang F, Xu Z, Clare AT. Direct metal deposition of TiB_2/AlSi10Mg composites using satellited powders. Mater Lett. 2018;214:123-6.

[124] Ma C, Chen L, Cao C, Li X. Nanoparticle-induced unusual melting and solidification behaviours of metals. Nat Commun. 2017;8:14178.

[125] Suryanarayana C. Mechanical alloying and milling. Prog Mater Sci. 2001;46:1-184.

[126] AlMangour B, Grzesiak D, Yang J-M. In situ formation of TiC-particle-reinforced stainless steel matrix nanocomposites during ball milling: Feedstock powder preparation for selective laser melting at various energy densities. Powder Technol. 2018;326:467-78.

[127] Yuying W, Xiangfa L, Binggang J, Chuanzhen H. Modification effect of Ni–38 wt.% Si on Al–12 wt.% Si alloy. J Alloys Compd. 2009;477:118-22.

[128] Yu W, Zhang Y, Jiang A, Yan T, Du H, Tian Y, et al. Multi-step nucleation in Al–Si liquids catalyzed by a Ni–Si master alloy. Mater Des. 2017;132:385-91.

[129] Yu W, Zhang Y, Yan T, Liu Y, Jiang A, Zheng H, et al. Enhanced nucleation of primary silicon in Al-20áwt.% Si alloy withá Ni-Si inoculation. J Alloys Compd. 2017;693:303-7.

[130] Hong C, Gu D, Dai D, Alkhayat M, Urban W, Yuan P, et al. Laser additive manufacturing of ultrafine TiC particle reinforced Inconel 625 based composite parts: tailored microstructures and enhanced performance. Mater Sci Eng, A. 2015;635:118-28.

[131] AlMangour B, Grzesiak D. Selective laser melting of TiC reinforced 316L stainless steel matrix nanocomposites: Influence of starting TiC particle size and volume content. Mater Des. 2016;104:141-51.

[132] Han Q, Setchi R, Evans SL. Characterisation and milling time optimisation of nanocrystalline aluminium powder for selective laser melting. Int J Adv Manuf Tech. 2017;88:1429-38.

[133] AlMangour B, Grzesiak D, Yang J-M. Selective laser melting of TiB_2/H13 steel nanocomposites: Influence of hot isostatic pressing post-treatment. J Mater Process Technol. 2017;244:344-53.

[134] Attar H, Bönisch M, Calin M, Zhang L-C, Scudino S, Eckert J. Selective laser melting of in situ titanium–titanium boride composites: Processing, microstructure and mechanical properties. Acta Mater. 2014;76:13-22.

[135] Lorusso M, Aversa A, Manfredi D, Calignano F, Ambrosio EP, Ugues D, et al. Tribological behavior of aluminum alloy AlSi10Mg-TiB_2 composites produced by direct metal laser sintering (DMLS). J Mater Eng Perform. 2016;25:3152-60.

[136] Gu D, Hagedorn Y-C, Meiners W, Wissenbach K, Poprawe R. Nanocrystalline TiC reinforced Ti matrix bulk-form nanocomposites by Selective Laser Melting (SLM): Densification, growth mechanism and wear behavior. Compos Sci Technol. 2011;71:1612-20.

[137] He B, Chang K, Wu W, Zhang C. The formation mechanism of TiC reinforcement and improved tensile strength in additive manufactured Ti matrix nanocomposite. Vacuum. 2017;143:23-7.

[138] Gu D, Wang H, Dai D, Yuan P, Meiners W, Poprawe R. Rapid fabrication of Al-based bulk-form nanocomposites with novel reinforcement and enhanced performance by selective laser melting. Scripta Mater. 2015;96:25-8.

[139] Gu D, Hagedorn Y-C, Meiners W, Wissenbach K, Poprawe R. Selective Laser Melting of in-situ TiC/Ti_5Si_3 composites with novel reinforcement architecture and elevated performance. Surf Coat Technol. 2011;205:3285-92.

[140] Gu D, Yuan P. Thermal evolution behavior and fluid dynamics during laser additive manufacturing of Al-based nanocomposites: Underlying role of reinforcement weight fraction. J Appl Phys. 2015;118:233109.

[141] Ma C, Zhao J, Cao C, Lin T-C, Li X. Fundamental Study on Laser Interactions With Nanoparticles-Reinforced Metals—Part I: Effect of Nanoparticles on Optical Reflectivity, Specific Heat, and Thermal Conductivity. J Manuf Sci Eng. 2016;138:121001.

[142] Chehrghani A, Torkamany MJ, Hamedi MJ, Sabbaghzadeh J. Numerical modeling and experimental investigation of TiC formation on titanium surface pre-coated by graphite under pulsed laser irradiation. Appl Surf Sci. 2012;258:2068-76.

[143] Vasantgadkar NA, Bhandarkar UV, Joshi SS. A finite element model to predict the ablation depth in pulsed laser ablation. Thin Solid Films. 2010;519:1421-30.

[144] Shi Q, Gu D, Xia M, Cao S, Rong T. Effects of laser processing parameters on thermal behavior and melting/solidification mechanism during selective laser melting of TiC/Inconel 718 composites. Opt Laser Technol. 2016;84:9-22.

[145] Ang L, Lau Y, Gilgenbach R, Spindler H. Analysis of laser absorption on a rough metal surface. Appl Phys Lett. 1997;70:696-8.

[146] Boley CD, Khairallah SA, Rubenchik AM. Calculation of laser absorption by metal powders in additive manufacturing. Appl Opt. 2015;54:2477-82.

[147] Sib SS, Barlow JW. Measurement and Prediction of the thermal Conductivity of Powders at High Temperatures. Solid Freeform Fabrication Symposium1994. p. 321-9.

[148] Gusarov AV, Smurov I. Modeling the interaction of laser radiation with powder bed at selective laser melting. Phys Procedia. 2010;5:381-94.

[149] Ordonez-Miranda J, Yang R, Alvarado-Gil JJ. Thermal Conductivity of Particulate Nanocomposites. Nanoscale Thermoelectrics: Springer; 2014. p. 93-139.

[150] Ordonez-Miranda J, Alvarado-Gil J. Thermal conductivity of nanocomposites with high volume fractions of particles. Compos Sci Technol. 2012;72:853-7.

[151] Chuang P-Y, Huang M-J. Model and simulation predictions of the thermal conductivity of compact random nanoparticle composites. Int J Heat Mass Transfer. 2013;61:490-8.

[152] Huang C-L, Qian X, Yang R-G. Influence of nanoparticle size distribution on the thermal conductivity of particulate nanocomposites. EPL-Europhys Lett. 2017;117:24001.

[153] Nan C-W, Birringer R, Clarke DR, Gleiter H. Effective thermal conductivity of particulate composites with interfacial thermal resistance. J Appl Phys. 1997;81:6692-9.

[154] Hasselman DPH, Donaldson KY, Geiger AL. Effect of reinforcement particle size on the thermal conductivity of a particulate-silicon carbide-reinforced aluminum matrix composite. J Am Ceram Soc. 1992;75:3137-40.

[155] Tian Z, Hu H, Sun Y. A molecular dynamics study of effective thermal conductivity in nanocomposites. Int J Heat Mass Transfer. 2013;61:577-82.

[156] Ma C, Zhao J, Cao C, Lin T-C, Li X. Fundamental Study on Laser Interactions With Nanoparticles-Reinforced Metals—Part II: Effect of Nanoparticles on Surface Tension, Viscosity, and Laser Melting. J Manuf Sci Eng. 2016;138:121002.

[157] Hao L, Dadbakhsh S, Seaman O, Felstead M. Selective laser melting of a stainless steel and hydroxyapatite composite for load-bearing implant development. J Mater Process Technol. 2009;209:5793-801.

[158] Metcalfe AG, Klein MJ. Interfaces in Fabricated Metal Matrix Composites. J Adhes. 1973;5:57-72.

[159] Rong T, Gu D, Shi Q, Cao S, Xia M. Effects of tailored gradient interface on wear properties of WC/Inconel 718 composites using selective laser melting. Surf Coat Technol. 2016;307:418-27.

[160] Kuruvilla AK, Bhanuprasad VV, Prasad KS, Mahajan YR. Effect of different reinforcements on composite-strengthening in aluminium. Bull Mater Sci. 1989;12:495-505.

[161] Zhao Y, Qian Z, Ma X, Chen H, Gao T, Wu Y, et al. Unveiling the semicoherent interface with definite orientation relationships between reinforcements and matrix in novel Al_3BC/Al composites. ACS Appl Mater Interfaces. 2016;8:28194–201.

[162] Rohatgi PK, Asthana R, Das S. Solidification, structures, and properties of cast metal-ceramic particle composites. Int Metals Rev. 2013;31:115-39.

[163] Rajan TPD, Pillai RM, Pai BC. Reinforcement coatings and interfaces in aluminium metal matrix composites. J Mater Sci. 1998;33:3491-503.

[164] Zheng B, Smugeresky J, Zhou Y, Baker D, Lavernia E. Microstructure and properties of laser-deposited Ti6Al4V metal matrix composites using Ni-coated powder. Metall Mater Trans A. 2008;39:1196-205.

[165] Zheng B, Topping T, Smugeresky JE, Zhou Y, Biswas A, Baker D, et al. The influence of Ni-coated TiC on laser-deposited IN625 metal matrix composites. Metall Mater Trans A. 2010;41:568-73.

[166] Yuan Q-h, Zeng X-s, Liu Y, Luo L, Wu J-b, Wang Y-c, et al. Microstructure and mechanical properties of AZ91 alloy reinforced by carbon nanotubes coated with MgO. Carbon. 2016;96:843-55.

[167] Mahamood R, Akinlabi E. Effect of the Scanning Speed of Treatment on the Microstructure, Microhardness, Wear, and Corrosion Behavior of Laser Metal-Deposited Ti–6AL–4V/TiC Composite. Mater Sci. 2017;53:76-85.

[168] Sing SL, Wiria FE, Yeong WY. Selective laser melting of lattice structures: A statistical approach to manufacturability and mechanical behavior. Robot Comput Integr Manuf. 2018;49:170-80.

[169] Thijs L, Verhaeghe F, Craeghs T, Humbeeck JV, Kruth J-P. A study of the microstructural evolution during selective laser melting of Ti–6Al–4V. Acta Mater. 2010;58:3303-12.

[170] Saedi S, Shayesteh Moghaddam N, Amerinatanzi A, Elahinia M, Karaca HE. On the effects of selective laser melting process parameters on microstructure and thermomechanical response of Ni-rich NiTi. Acta Mater. 2018;144:552-60.

[171] Simonelli M, Tuck C, Aboulkhair NT, Maskery I, Ashcroft I, Wildman RD, et al. A study on the laser spatter and the oxidation reactions during selective laser melting of

316L stainless steel, Al-Si10-Mg, and Ti-6Al-4V. Metall Mater Trans A. 2015;46:3842-51.

[172] Yap CY, Chua CK, Dong ZL. An effective analytical model of selective laser melting. Virtual Phys Prototyp. 2016;11:21-6.

[173] Yang J, Han J, Yu H, Yin J, Gao M, Wang Z, et al. Role of molten pool mode on formability, microstructure and mechanical properties of selective laser melted Ti-6Al-4V alloy. Mater Des. 2016;110:558-70.

[174] Yadroitsev I, Krakhmalev P, Yadroitsava I. Selective laser melting of Ti6Al4V alloy for biomedical applications: Temperature monitoring and microstructural evolution. J Alloys Compd. 2014;583:404-9.

[175] Ciurana J, Hernandez L, Delgado J. Energy density analysis on single tracks formed by selective laser melting with CoCrMo powder material. Int J Adv Manuf Tech. 2013;68:1103-10.

[176] Gusarov AV, Yadroitsev I, Bertrand P, Smurov I. Heat transfer modelling and stability analysis of selective laser melting. Appl Surf Sci. 2007;254:975-9.

[177] Ma M, Wang Z, Gao M, Zeng X. Layer thickness dependence of performance in high-power selective laser melting of 1Cr18Ni9Ti stainless steel. J Mater Process Technol. 2015;215:142-50.

[178] Li R, Liu J, Shi Y, Wang L, Jiang W. Balling behavior of stainless steel and nickel powder during selective laser melting process. Int J Adv Manuf Tech. 2011;59:1025-35.

[179] Qiu C, Panwisawas C, Ward M, Basoalto HC, Brooks JW, Attallah MM. On the role of melt flow into the surface structure and porosity development during selective laser melting. Acta Mater. 2015;96:72-9.

[180] Kruth J-P, Froyen L, Van Vaerenbergh J, Mercelis P, Rombouts M, Lauwers B. Selective laser melting of iron-based powder. J Mater Process Technol. 2004;149:616-22.

[181] Song B, Dong S, Zhang B, Liao H, Coddet C. Effects of processing parameters on microstructure and mechanical property of selective laser melted Ti6Al4V. Mater Des. 2012;35:120-5.

[182] Gu D, Wang H, Chang F, Dai D, Yuan P, Hagedorn Y-C, et al. Selective Laser Melting Additive Manufacturing of TiC/AlSi10Mg Bulk-form Nanocomposites with Tailored Microstructures and Properties. Phys Procedia. 2014;56:108-16.

[183] Aboulkhair NT, Everitt NM, Ashcroft I, Tuck C. Reducing porosity in AlSi10Mg parts processed by selective laser melting. Addit Manuf. 2014;1:77-86.

[184] Dadbakhsh S, Hao L, Jerrard P, Zhang D. Experimental investigation on selective laser melting behaviour and processing windows of in situ reacted Al/Fe_2O_3 powder mixture. Powder Technol. 2012;231:112-21.

[185] Mishra P, Ilar T, Brueckner F, Kaplan A. Energy efficiency contributions and losses during selective laser melting. J Laser Appl. 2018;30:032304.

[186] Yang Y, Wen S, Wei Q, Li W, Liu J, Shi Y. Effect of scan line spacing on texture, phase and nanohardness of TiAl/TiB_2 metal matrix composites fabricated by selective laser melting. J Alloys Compd. 2017;728:803-14.

[187] Li R, Shi Y, Wang Z, Wang L, Liu J, Jiang W. Densification behavior of gas and water atomized 316L stainless steel powder during selective laser melting. Appl Surf Sci. 2010;256:4350-6.

[188] Zhang S, Wei Q, Cheng L, Li S, Shi Y. Effects of scan line spacing on pore characteristics and mechanical properties of porous Ti6Al4V implants fabricated by selective laser melting. Mater Des. 2014;63:185-93.

[189] Yadroitsev I, Thivillon L, Bertrand P, Smurov I. Strategy of manufacturing components with designed internal structure by selective laser melting of metallic powder. Appl Surf Sci. 2007;254:980-3.

[190] Di W, Yongqiang Y, Xubin S, Yonghua C. Study on energy input and its influences on single-track, multi-track, and multi-layer in SLM. Int J Adv Manuf Tech. 2012;58:1189-99.

[191] Gu D, Shen Y. Processing and microstructure of submicron WC–Co particulate reinforced Cu matrix composites prepared by direct laser sintering. Mater Sci Eng, A. 2006;435:54-61.

[192] Tang M, Pistorius P, Beuth J. Geometric model to predict porosity of part produced in powder bed system. Mater Sci Technol. 2015:129-35.

[193] Tang M, Pistorius PC. Oxides, porosity and fatigue performance of AlSi10Mg parts produced by selective laser melting. Int J Fatigue. 2017;94:192-201.

[194] Tang M. Inclusions, Porosity, and Fatigue of AlSi10Mg Parts Produced by Selective Laser Melting [D]. Pittsburgh: Carnegie Mellon University; 2017.

[195] Wei HL, Elmer JW, DebRoy T. Origin of grain orientation during solidification of an aluminum alloy. Acta Mater. 2016;115:123-31.

[196] Li XP, Van Humbeeck J, Kruth JP. Selective laser melting of weak-textured commercially pure titanium with high strength and ductility: A study from laser power perspective. Mater Des. 2017;116:352-8.

[197] Thijs L, Montero Sistiaga ML, Wauthle R, Xie Q, Kruth J-P, Van Humbeeck J. Strong morphological and crystallographic texture and resulting yield strength anisotropy in selective laser melted tantalum. Acta Mater. 2013;61:4657-68.

[198] Thijs L, Kempen K, Kruth J-P, Van Humbeeck J. Fine-structured aluminium products with controllable texture by selective laser melting of pre-alloyed AlSi10Mg powder. Acta Mater. 2013;61:1809-19.

[199] Li X, Kang C, Huang H, Sercombe T. The role of a low-energy–density re-scan in fabricating crack-free $Al_{85}Ni_5Y_6Co_2Fe_2$ bulk metallic glass composites via selective laser melting. Mater Des. 2014;63:407-11.

[200] Yasa E, Deckers J, Kruth JP. The investigation of the influence of laser re-melting on density, surface quality and microstructure of selective laser melting parts. Rapid Prototyping J. 2011;17:312-27.

[201] Rashid R, Masood SH, Ruan D, Palanisamy S, Rahman Rashid RA, Elambasseril J, et al. Effect of energy per layer on the anisotropy of selective laser melted AlSi12 aluminium alloy. Addit Manuf. 2018;22:426-39.

[202] Brandl E, Heckenberger U, Holzinger V, Buchbinder D. Additive manufactured AlSi10Mg samples using Selective Laser Melting (SLM): Microstructure, high cycle fatigue, and fracture behavior. Mater Des. 2012;34:159-69.

[203] Tolosa I, Garciandía F, Zubiri F, Zapirain F, Esnaola A. Study of mechanical properties of AISI 316 stainless steel processed by "selective laser melting", following different manufacturing strategies. Int J Adv Manuf Tech. 2010;51:639-47.

[204] Agarwala M, Bourell D, Beaman J, Marcus H, Barlow J. Direct selective laser sintering of metals. Rapid Prototyping J. 1995;1:26-36.

[205] Wen S, Hu H, Zhou Y, Chen Z, Wei Q, Shi Y. Enhanced hardness and wear property of S136 mould steel with nano-TiB_2 composites fabricated by selective laser melting method. Appl Surf Sci. 2018;457:11-20.

[206] Song B, Dong S, Coddet C. Rapid in situ fabrication of Fe/SiC bulk nanocomposites by selective laser melting directly from a mixed powder of microsized Fe and SiC. Scripta Mater. 2014;75:90-3.

[207] Ferguson JB, Sheykh-Jaberi F, Kim C-S, Rohatgi PK, Cho K. On the strength and strain to failure in particle-reinforced magnesium metal-matrix nanocomposites (Mg MMNCs). Mater Sci Eng, A. 2012;558:193-204.

[208] Habibnejad-Korayem M, Mahmudi R, Poole WJ. Enhanced properties of Mg-based nano-composites reinforced with Al_2O_3 nano-particles. Mater Sci Eng, A. 2009;519:198-203.

[209] Ramakrishnan N. An analytical study on strengthening of particulate reinforced metal matrix composites. Acta Mater. 1996;44:69-77.

[210] Kim C-S, Sohn I, Nezafati M, Ferguson JB, Schultz BF, Bajestani-Gohari Z, et al. Prediction models for the yield strength of particle-reinforced unimodal pure magnesium (Mg) metal matrix nanocomposites (MMNCs). J Mater Sci. 2013;48:4191-204.

[211] Sanaty-Zadeh A. Comparison between current models for the strength of particulate-reinforced metal matrix nanocomposites with emphasis on consideration of Hall–Petch effect. Mater Sci Eng, A. 2012;531:112-8.

[212] Ye J, Han BQ, Lee Z, Ahn B, Nutt SR, Schoenung JM. A tri-modal aluminum based composite with super-high strength. Scripta Mater. 2005;53:481-6.

[213] Nguyen Q, Gupta M. Increasing significantly the failure strain and work of fracture of solidification processed AZ31B using nano-Al_2O_3 particulates. J Alloys Compd. 2008;459:244-50.

[214] Ma ZY, Tjong SC, Li YL, Liang Y. High temperature creep behavior of nanometric Si3N4 particulate reinforced aluminium composite. Mater Sci Eng, A. 1997;225:125-34.

[215] Jue J, Gu D, Chang K, Dai D. Microstructure evolution and mechanical properties of Al-Al_2O_3 composites fabricated by selective laser melting. Powder Technol. 2017;310:80-91.

[216] Hull D, Clyne TW. An introduction to composite materials. Cambridge: Cambridge university press; 1996.

[217] Zhang Z, Chen D. Consideration of Orowan strengthening effect in particulate-reinforced metal matrix nanocomposites: A model for predicting their yield strength. Scripta Mater. 2006;54:1321-6.

[218] Zhang Z, Chen DL. Contribution of Orowan strengthening effect in particulate-reinforced metal matrix nanocomposites. Mater Sci Eng, A. 2008;483-484:148-52.

[219] Wang X, Wang N, Wang L, Hu X, Wu K, Wang Y, et al. Processing, microstructure and mechanical properties of micro-SiC particles reinforced magnesium matrix

composites fabricated by stir casting assisted by ultrasonic treatment processing. Mater Des. 2014;57:638-45.

[220] Goh C, Wei J, Lee L, Gupta M. Simultaneous enhancement in strength and ductility by reinforcing magnesium with carbon nanotubes. Mater Sci Eng, A. 2006;423:153-6.

[221] Goh C, Wei J, Lee L, Gupta M. Ductility improvement and fatigue studies in Mg-CNT nanocomposites. Compos Sci Technol. 2008;68:1432-9.

[222] Nie K, Wang X, Wu K, Xu L, Zheng M, Hu X. Processing, microstructure and mechanical properties of magnesium matrix nanocomposites fabricated by semisolid stirring assisted ultrasonic vibration. J Alloys Compd. 2011;509:8664-9.

[223] Ma E. Eight routes to improve the tensile ductility of bulk nanostructured metals and alloys. JOM. 2006;58:49-53.

[224] Liu G, Zhang G, Jiang F, Ding X, Sun Y, Sun J, et al. Nanostructured high-strength molybdenum alloys with unprecedented tensile ductility. Nat Mater. 2013;12:344-50.

[225] Jerrard PGE, Hao L, Dadbakhsh S, Evans KE. Consolidation Behaviour and Microstructural Characteristics of Al and a Mixture of Al-Cu Alloy Powders Following Selective Laser Melting Processing. Laser Eng. 2012;22:371-81.

[226] Zhao S, Shen X, Yang J, Teng W, Wang Y. Densification behavior and mechanical properties of nanocrystalline TiC reinforced 316L stainless steel composite parts fabricated by selective laser melting. Opt Laser Technol. 2018;103:239-50.

[227] Dadbakhsh S, Hao L. Effect of Fe_2O_3 content on microstructure of Al powder consolidated parts via selective laser melting using various laser powers and speeds. Int J Adv Manuf Tech. 2014;73:1453-63.

[228] Geng J, Liu G, Wang F, Hong T, Dai J, Wang M, et al. Microstructural correlated damage mechanisms of the high-cycle fatigued in-situ TiB_2/Al-Cu-Mg composite. Mater Des. 2017;135:423-38.

[229] Rafi HK, Starr TL, Stucker BE. A comparison of the tensile, fatigue, and fracture behavior of Ti–6Al–4V and 15-5 PH stainless steel parts made by selective laser melting. Int J Adv Manuf Tech. 2013;69:1299-309.

[230] Wang F, Xu J, Li J, Li X, Wang H. Fatigue crack initiation and propagation in A356 alloy reinforced with in situ TiB_2 particles. Mater Des. 2012;33:236-41.

[231] Sangid MD, Maier HJ, Sehitoglu H. A physically based fatigue model for prediction of crack initiation from persistent slip bands in polycrystals. Acta Mater. 2011;59:328-41.

[232] Leuders S, Thöne M, Riemer A, Niendorf T, Tröster T, Richard H, et al. On the mechanical behaviour of titanium alloy TiAl6V4 manufactured by selective laser melting: Fatigue resistance and crack growth performance. Int J Fatigue. 2013;48:300-7.

[233] Chawla N, Andres C, Jones JW, Allison JE. The effect of reinforcement volume fraction and particle size on the fatigue behavior of an aluminum alloy/SiC composite. Industrial Heating. 1999;66:61-6.

[234] Yang KV, Rometsch P, Jarvis T, Rao J, Cao S, Davies C, et al. Porosity formation mechanisms and fatigue response in Al-Si-Mg alloys made by selective laser melting. Mater Sci Eng, A. 2018;712:166-74.

[235] Kasperovich G, Hausmann J. Improvement of fatigue resistance and ductility of TiAl6V4 processed by selective laser melting. J Mater Process Technol. 2015;220:202-14.

[236] Edwards P, Ramulu M. Fatigue performance evaluation of selective laser melted Ti–6Al–4V. Mater Sci Eng, A. 2014;598:327-37.

[237] Tjong S, Wang G. High-cycle fatigue properties of Al-based composites reinforced with in situ TiB_2 and Al_2O_3 particulates. Mater Sci Eng, A. 2004;386:48-53.

[238] Bonnen JJ, Allison JE, Jones JW. Fatigue behavior of a 2xxx series aluminum alloy reinforced with 15 vol pct SiCp. Metall Trans A. 1991;22:1007-19.

[239] Tee KL, Lü L, Lai MO. Improvement in mechanical properties of in-situ Al–TiB_2 composite by incorporation of carbon. Mater Sci Eng, A. 2003;339:227-31.

[240] Kumai S, King JE, Knott JF. Short and long fatigue crack growth in a SiC reinforced aluminium alloy. Fatigue Fract Eng Mater Struct. 1990;13:511-24.

[241] Levin M, Karlsson B. Crack initiation and growth during low-cycle fatigue of discontinuously reinforced metal-matrix composites. Int J Fatigue. 1993;15:377-87.

[242] Cain V, Thijs L, Van Humbeeck J, Van Hooreweder B, Knutsen R. Crack propagation and fracture toughness of Ti6Al4V alloy produced by selective laser melting. Addit Manuf. 2015;5:68-76.

[243] Connors WC. Fatigue striation spacing analysis. Mater Charact. 1994;33:245-53.

[244] Suresh S. Fatigue of materials. Cambridge: Cambridge university press; 1998.

[245] Arsenault RJ, Fishman S, Taya M. Deformation and fracture behavior of metal-ceramic matrix composite materials. Prog Mater Sci. 1994;38:1-157.

[246] Gu D, Shen Y. Balling phenomena in direct laser sintering of stainless steel powder: Metallurgical mechanisms and control methods. Mater Des. 2009;30:2903-10.

[247] Cherry JA, Davies HM, Mehmood S, Lavery NP, Brown SGR, Sienz J. Investigation into the effect of process parameters on microstructural and physical properties of 316L stainless steel parts by selective laser melting. Int J Adv Manuf Tech. 2014;76:869-79.

[248] Qi H, Azer M, Ritter A. Studies of standard heat treatment effects on microstructure and mechanical properties of laser net shape manufactured Inconel 718. Metall Mater Trans A. 2009;40:2410-22.

[249] Panwisawas C, Qiu CL, Sovani Y, Brooks JW, Attallah MM, Basoalto HC. On the role of thermal fluid dynamics into the evolution of porosity during selective laser melting. Scripta Mater. 2015;105:14-7.

[250] Kasperovich G, Haubrich J, Gussone J, Requena G. Correlation between porosity and processing parameters in TiAl6V4 produced by selective laser melting. Mater Des. 2016;105:160-70.

[251] Katayama S. Introduction: fundamentals of laser welding. Handbook of laser welding technologies: Elsevier; 2013. p. 3-16.

[252] Weingarten C, Buchbinder D, Pirch N, Meiners W, Wissenbach K, Poprawe R. Formation and reduction of hydrogen porosity during selective laser melting of AlSi10Mg. J Mater Process Technol. 2015;221:112-20.

[253] Kang N, Coddet P, Chen C, Wang Y, Liao H, Coddet C. Microstructure and wear behavior of in-situ hypereutectic Al–high Si alloys produced by selective laser melting. Mater Des. 2016;99:120-6.

[254] Dai D, Gu D. Effect of metal vaporization behavior on keyhole-mode surface morphology of selective laser melted composites using different protective atmospheres. Appl Surf Sci. 2015;355:310-9.

[255] Kempen K, Thijs L, Vrancken B, Buls S, Van Humbeeck J, Kruth J. Producing crack-free, high density M2 Hss parts by selective laser melting: pre-heating the baseplate. Proceedings of the 24th international solid freeform fabrication symposium Laboratory for freeform fabrication, Austin, TX2013. p. 131-9.

[256] Gåård A, Krakhmalev P, Bergström J. Microstructural characterization and wear behavior of (Fe, Ni)–TiC MMC prepared by DMLS. J Alloys Compd. 2006;421:166-71.

[257] Wang L, Jiang W, Qin C, Chen L. In-situ synthesized Ti_5Si_3/TiC composites by spark plasma sintering technology. J Mater Sci. 2006;41:3831-5.

[258] Wong CP, Bollampally RS. Thermal conductivity, elastic modulus, and coefficient of thermal expansion of polymer composites filled with ceramic particles for electronic packaging. J Appl Polym Sci. 1999;74:3396-403.

[259] Cao XQ, Vassen R, Stoever D. Ceramic materials for thermal barrier coatings. J Eur Ceram Soc. 2004;24:1-10.

[260] Guo HB, Miao X, Chen Y, Cheang P, Khor KA. Characterization of hydroxyapatite–and bioglass–316L fibre composites prepared by spark plasma sintering. Mater Lett. 2004;58:304-7.

[261] Taya M, Hayashi S, Kobayashi AS, Yoon H. Toughening of a particulate-reinforced ceramic-matrix composite by thermal residual stress. J Am Ceram Soc. 1990;73:1382-91.

[262] Munro RG. Material properties of titanium diboride. J Res Natl Inst Stand Technol. 2000;105:709.

[263] Huber T, Degischer H-P, Lefranc G, Schmitt T. Thermal expansion studies on aluminium-matrix composites with different reinforcement architecture of SiC particles. Compos Sci Technol. 2006;66:2206-17.

[264] Miao X. Observation of microcracks formed in HA-316L composites. Mater Lett. 2003;57:1848-53.

[265] Jiang SS, Zhang KF. Study on controlling thermal expansion coefficient of ZrO_2–TiO_2 ceramic die for superplastic blow-forming high accuracy Ti–6Al–4V component. Mater Des. 2009;30:3904-7.

[266] Yilmaz H, Dincer C. Comparison of the bond compatibility of titanium and an NiCr alloy to dental porcelain1. J Dent. 1999;27:215-22.

[267] Mercelis P, Kruth J-P. Residual stresses in selective laser sintering and selective laser melting. Rapid Prototyping J. 2006;12:254-65.

[268] Li Y, Zhou K, Tan P, Tor SB, Chua CK, Leong KF. Modeling temperature and residual stress fields in selective laser melting. Int J Mech Sci. 2018;136:24-35.

[269] Zhu HH, Lu L, Fuh JYH. Study on shrinkage behaviour of direct laser sintering metallic powder. Proc Inst Mech Eng Pt B: J Eng Manuf. 2006;220:183-90.

[270] Read N, Wang W, Essa K, Attallah MM. Selective laser melting of AlSi10Mg alloy: Process optimisation and mechanical properties development. Mater Des. 2015;65:417-24.

[271] Ramasamy S, Albright C. CO_2 and Nd: YAG laser beam welding of 6111-T4 aluminum alloy for automotive applications. J Laser Appl. 2000;12:101-15.

[272] Zhao H, DebRoy T. Weld metal composition change during conduction mode laser welding of aluminum alloy 5182. Metall Mater Trans B. 2001;32:163-72.

[273] Collur MM, Paul A, DebRoy T. Mechanism of alloying element vaporization during laser welding. Metall Trans B. 1987;18:733-40.

[274] Pastor M, Zhao H, Martukanitz R, DebRoy T. Porosity, underfill and magnesium lose during continuous wave Nd: YAG laser welding of thin plates of aluminum alloys 5182 and 5754. Weld J. 1999;78:207-s.

[275] Cao X, Wallace W, Immarigeon J-P, Poon C. Research and progress in laser welding of wrought aluminum alloys. II. Metallurgical microstructures, defects, and mechanical properties. Mater Manuf Processes. 2003;18:23-49.

[276] Katayama S, Seto N, Mizutani M, Matsunawa A. Formation mechanism of porosity in high power YAG laser welding. Proceedings of the International Congress on Applications of Lasers and Electro-optics: ICALEO: Springer-Verlag; 2000. p. 200016.

[277] Ghosh SK, Saha P. Crack and wear behavior of SiC particulate reinforced aluminium based metal matrix composite fabricated by direct laser sintering process. Mater Des. 2011;32:139-45.

[278] Miracle DB. Metal matrix composites – From science to technological significance. Compos Sci Technol. 2005;65:2526-40.

[279] Prasad SV, Asthana R. Aluminum metal-matrix composites for automotive applications: tribological considerations. Tribol Lett. 2004;17:445-53.

[280] Hu Z, Chen F, Xu J, Nian Q, Lin D, Chen C, et al. 3D printing graphene-aluminum nanocomposites. J Alloys Compd. 2018;746:269-76.

[281] Han Q, Geng Y, Setchi R, Lacan F, Gu D, Evans SL. Macro and nanoscale wear behaviour of Al-Al_2O_3 nanocomposites fabricated by selective laser melting. Composites Part B: Engineering. 2017;127:26-35.

[282] Wong KK, Ho JY, Leong KC, Wong TN. Fabrication of heat sinks by Selective Laser Melting for convective heat transfer applications. Virtual Phys Prototyp. 2016;11:159-65.

[283] Ho JY, Wong KK, Leong KC, Wong TN. Convective heat transfer performance of airfoil heat sinks fabricated by selective laser melting. Int J Therm Sci. 2017;114:213-28.

[284] Ho JY, Wong KK, Leong KC. Saturated pool boiling of FC-72 from enhanced surfaces produced by Selective Laser Melting. Int J Heat Mass Transfer. 2016;99:107-21.

[285] Dai D, Gu D. Thermal behavior and densification mechanism during selective laser melting of copper matrix composites: Simulation and experiments. Mater Des. 2014;55:482-91.

[286] Witte F, Feyerabend F, Maier P, Fischer J, Stormer M, Blawert C, et al. Biodegradable magnesium–hydroxyapatite metal matrix composites. Biomaterials. 2007;28:2163-74.

[287] Sing SL, An J, Yeong WY, Wiria FE. Laser and electron-beam powder-bed additive manufacturing of metallic implants: A review on processes, materials and designs. J Orth Res. 2016;34:369-85.

[288] Bose S, Ke D, Sahasrabudhe H, Bandyopadhyay A. Additive manufacturing of biomaterials. Prog Mater Sci. 2018;93:45-111.

[289] Chen Y, Zhang J, Dai N, Qin P, Attar H, Zhang L-C. Corrosion Behaviour of Selective Laser Melted Ti-TiB Biocomposite in Simulated Body Fluid. Electrochim Acta. 2017;232:89-97.